UNIVERSITÀ
DEGLI STUDI
FIRENZE

DOTTORATO DI RICERCA IN

AREA DEL FARMACO E TRATTAMENTI INNOVATIVI

CICLO XXIX

COORDINATORE Prof.ssa Teodori Elisabetta

IN VIVO 7T MR IMAGING AND MR SPECTROSCOPY IN PATIENTS WITH BRAIN LESIONS

Settore Scientifico Disciplinare MED/39

Dottorando
Dott. De Ciantis Alessio

Tutore scientifico
Prof. Guerrini Renzo

Tutore teorico
Prof. Mugelli Alessandro

Coordinatore del corso
Prof.ssa Teodori Elisabetta

Anni 2013/2016

ABSTRACT

Magnetic resonance imaging (MRI) is an imaging modality that enables non-invasively the identification of in-vivo anatomical brain structures. Since first clinical applications MRI has been constantly improved increasing the static magnetic field strength, improving the radiofrequency (RF) detection system, developing dedicated acquisition sequences and optimizing the processes for image reconstruction.

Magnetic resonance spectroscopy (MRS) complements MRI as a non-invasive tecnique for the characterization of tissue obtaining spectra of signals from each spatial location of interest. MRS enables the quantification of in vivo brain metabolite concentrations. It has great impact in diagnosing and better understanding of numerous brain pathologies including epilepsy, tumors, metabolic diseases, multiple sclerosis and stroke.

While MRI uses the signal from hydrogen protons to produce anatomical images, proton MRS uses this information to define the concentration of brain metabolites such as N-acetyl-L-aspartate (NAA), choline (Cho), creatine (Cr) and lactate (Lac).

In the past few years, 7T has shown promise in studing in-vivo human brain. Compared to conventional field strenghts (1.5 and 3T), 7T offers higher signal-to-noise ratio (SNR), which enables higher spatial resolution. As a result, 7T can provide better depiction of anatomic structures and enhance both detection and characterization of brain lesions, increasing diagnostic confidence. Moreover, the combination of increased SNR associated with the increased spectral separation of metabolite peaks results in higher resolution spectroscopic images and improved spectral quantification.

However, the transition to UHF 7T also introduces new technical issues, including inhomogeneity of B0 (magnetic field) and B1 (the applied RF), errors in chemical shift localization, increased deposition of RF power within the patient. These concerns cause image artifacts, limit section number/spatial coverage, and limit the use of MR spectroscopy for clinical purposes.

The work for this thesis has been carried out at Imago7 Foundation (Calambrone, Pisa, Italy) where the first and unique Ultra High Field 7T MR scanner in Italy for human study has been installed.

The main objective of this work is to explore the added value of 7T MRI in providing anatomical and structural details of specific brain lesions in both adults and children. Secondly, proton 7T MRS (^{1}H MRS) is used to detect in vivo brain neurotransmitter levels. Thirdly, combining $B1^{+}$ in vivo measurements with electromagnetic simulations, local and global specific absorbation rate (SAR) exposure are predicted to ensure the respect of regulatory limit imposed by the International Electrotechnical Commission (IEC).

This dissertation is dedicated to the one I love most: my Son Emanuele.

I am indebted to him for the absent moments when he needs me.

ACKNOWLEDGMENTS

The work described in the thesis is the product of collaborations with a number of colleagues with different specialization and expertise in UHF 7T MR. I would like to thank everyone at Imago7 Foundation for their support and assistance over the project explaining me how the 7T is made and how it really works. In particular I want to thank, Mauro, Gianni and Mark without whom my understanding of 7T MR would be much less. Further, I acknowledge Carmen for her help, encouragement and critical comments during these years worked together at Children's Hospital A. Meyer in Florence and at Imago7 Foundation. During these years, we have spent a lot of time together discussing patients and writing papers and I have learnt a lot from her. I also wish to thank Alessandra for acquiring, analysing the MRS spectra and for teaching me a lot about MRS.

I would like to thank my supervisor Prof. Renzo Guerrini for his intellectual guidance and scientific support from the start of the project and the opportunities he has provided me in the past years.

I also wish to thank Mirco for teaching me more about MR Imaging and Michela who introduce me into the field of 7T MR Spectroscopy. Thanks you both, for the opportunity you gave me to join the Imago7 team and to use the 7T MR scan.

Finally, I thank the patients and their families for participating in our research.

I acknowledge financial support for my doctoral studies received by the Scholarship from Pisa Foundation - Project 133-11 “Ultra-high field MRI targeted imaging of dysplastic cortical lesions and dysembryoplastic tumours”.

I acknowledge also the financial support of the European Research Project on Rare Diseases (E-Rare-2, TUB-GENCODEV, 11-027), the European Union Seventh Framework Programme FP7/2007–2013 (under the project DESIRE: Development and Epilepsy: Strategies for Innovative Research to improve diagnosis, prevention and treatment in Children with difficult to treat Epilepsy, Grant Agreement: 602531) and the Italian Ministry of Health (RC 5/2015 to IRCCS Fondazione Stella Maris).

THESIS OUTLINE

The presented thesis is subdivided into five chapters.

Chapter 1 provides an overview of the 7T MR imaging and 7T MR spectroscopy with a description of the opportunities and challenges arising from the use of UHF 7T MR scanner.

Chapter 2 describes the added value of 7T MRI in providing details of structural changes and the extent of cortical malformation in 10 adults patients with polymicrogyria with respect 3T imaging. Further, the limitations encountered while exploring the polymicrogyric brain with 7T are presented. This chapter is a reproduction of the original article "Ultra High Field MR imaging in Polymicrogyria and Epilepsy" (De Ciantis A. et al., AJNR, 2015 vol. 36, pp. 309-316).

Chapter 3 describes the evaluation of the diagnostic yield of 7T MRI in detecting and characterizing structural lesions in 21 patients with intractable focal epilepsy and unrevealing conventional MRI. This chapter is a reproduction of the original article "7T MRI in focal epilepsy with unrevealing conventional field strength imaging" (De Ciantis A. et al., Epilepsia, 2016 vol 57, no.3, pp 445-454).

Chapter 4 describes the methods to predict local and global SAR exposure in two 7T sequences (SILENT and FLAIR) in adults and children by combining electromagnetic simulations on two generic anatomic human head models with subject-specific B_1^+ maps measured in-vivo. Phantom experiments, simulations with human head models and in vivo measurements are detailed. This chapter is a reproduction of the original article "SAR Prediction in Adults and Children by Combining Measured B1+ Maps and Simulations at 7.0T" (Tiberi. et al., J. Magn. Reson. Imaing, 2016 vol. 44, pp. 1048-1055).

Chapter 5 provides preliminary data obtained using 7T Single Voxel ^{1}H Spectroscopy in patients with brain lesions. Data concerning the acquisition protocol and the methods for metabolites characterization and quantification are described. The description of three cases is reported.

TABLE OF CONTENTS

Abstract ii

Dedication iv

Acknowledgments v

Thesis outline vi

Chapter 1

7T MR Imaging and MR Spectroscopy 1

1.1. Introduction 1

1.2. 7T MR Imaging 3

1.2.1 Advantages of 7T MRI 3

1.2.2 Challenges of 7T MRI 4

1.2.3 Patients Experience, Risk and Physiological Side Effects 5

1.2.4 Anatomical Brain Imaging 5

1.2.5 Epilepsy 6

1.2.6 Brain Tumors 6

1.3. 7T MR Spectroscopy: ^{1}H MRS 7

1.3.1 Single Voxel MRS 9

1.3.2 7T ^{1}H MRS in Brain Tumors and Epilepsy 9

1.4. The Specific Absorption Rate (SAR) 10

1.5. References 11

Chapter 2

Ultra High Field MR imaging in Polymicrogyria and Epilepsy 25

2.1. Abstract 26

2.1.1 Background and Purpose 26

2.1.2 Materials and Methods 26

2.1.3 Results 26
2.1.4 Conclusion 27
2.2. Introduction 27
2.3. Materials and Methods 29
2.3.1 Ethics Statement 29
2.3.2 Subjects 29
2.3.3 Data Acquisition 29
2.3.4 Data Analysis 30
2.4. Results 31
2.5. Discussion 36
2.6. Conclusion 40
2.7. References 40
2.8. Supplemental On-line Materials 46

Chapter 3

7T MRI in focal epilepsy with unrevealing conventional field strength imaging 50
3.1. Summary 51
3.1.1 Objective 51
3.1.2 Methods 51
3.1.3 Results 51
3.1.4 Significance 51
3.2. Introduction 52
3.3. Methods 53
3.3.1 Patients 53
3.3.2 Scalp and invasive video-EEG recordings 53
3.3.3 MRI Acquisition 54
3.3.4 MRI Evaluation 55

3.3.5 Surgery and Post-operative outcome 55
3.3.6 Histopathology 55
3.4. Results 55
3.4.1 Patients 55
3.4.2 Video-EEG and Stereo-EEG recordings 58
3.4.3 7T MRI 58
3.4.4 Surgery and Post-operative outcome 63
3.4.5 Hystopathology 63
3.5. Discussion 63
3.6. Acknowledgment 65
3.7. References 66

Chapter 4

SAR Prediction in Adults and Children by Combining Measured B1+ Maps and Simulations at 7.0 Tesla 69
4.1. Abstract 70
4.1.1 Purpose 70
4.1.2 Materials and Method 70
4.1.3 Results 70
4.1.4 Conclusions 70
4.2. Introduction 71
4.3. Materials and Methods 72
4.3.1 Electromagnetic simulations 72
4.3.2 Phantom Experiments 74
4.3.3 In-Vivo Measurements 75
4.3.4 SAR Prediction by Combining B_1^+ In-Vivo Measurements with Electromagnetic Simulations 76
4.3.5 Statistical Analysis 77

4.4. Results 77
4.5. Discussion 82
4.6. Acknowledgment 85
4.7. References 85

Chapter 5

In Vivo 7T MR Spectroscopy in patients with brain lesions: Preliminary data 88
5.1. Introduction 88
5.2. Methods 89
5.2.1 Patients 89
5.2.2 MR Imaging and Spectroscopy 90
5.2.3 Post-processing and Metabolite Quantification 92
5.3. Illustrative Cases 93
5.3.1 Focal Cortical Dysplasia (FCD) 93
5.3.2 Case 1 94
5.3.3 Tumors 95
5.3.4 Case 2 96
5.3.5 Case 3 97
5.4. Preliminary Results 98
5.5. Future Perspectives 98
5.6. References 99

Chapter 1.

7T MR Imaging and 7T MR Spectroscopy

1.1 Introduction

Nuclear magnetic resonance (NMR) is a physical phenomenon in which nuclei in a magnetic field absorb and re-emit electromagnetic radiation (Hendee and Morgan 1984). NMR was originally a field of Physics, which overflowed into Chemistry, Biochemistry and Medicine. Interest in the potential of NMR for medical diagnostic purposes began in the early 1970s when Raymond Damadian studied the differences in relaxation times between normal and cancerous tissue (Damadian 1971), motivating scientists to consider magnetic resonance for the detection of diseases. In 1975 Richard Ernest proposed magnetic resonance imaging using phase and frequency encoding and Fourier Trasform (Kumar et al 1975), which represents the basis of current MR Imaging techniques.

In vivo MR Imaging (MRI) and MR Spectroscopy (MRS) became possible in the eraly 1980s with the advent of whole-body magnets (Eldestein et al. 1980). After this date, several companies started to invest in MRI developments and to promote clinical trials.

Although, both tecniques are based on the same physical principles, MRS provides physiological and chemical information (phase and frequency are used to identify spectral patterns of specific metabolites, while the amplitude is used as a scale for the concentration of these metabolites) conversely MRI provides anatomical information (frequency and phase are used to encode the spatial coordinates, while the signal amplitude is translated into grey value of the resulting image) (Tosetti et al. 2006).

MRI is a versatile technique to image changes in brain anatomy and function. Since its introduction this method has become the most important imaging technique for the diagnosis and theraphy monitoring of diseases, particularly in clinical brain studies and also in neuroscientific research (European Federation of Neurological Societies Task Force 2001; Speck 2010; Balchandani and Naidich 2015).

MRS is a non-invasive technique, which can be used to provide cellular biochemistry characterization of brain diseases, and to evaluate the biochemical changes after treatment. Localized proton MRS of the human brain, first reported more than 20 years ago (Bottomley et al. 1985; Hanstock et al. 1988; Frahm et al. 1989). Today MRS is used clinically in many medical centres worldwide for the evaluation of brain lesions, however, it has not been established yet as a routine tool for clinical diagnostics. MRS offers the opportunity for localizing biochemical information relating to specific metabolites in a volume of interest (VOI) to study brain lesional substrates. The main nucleus studied in brain MRS is the hydrogen (^{1}H) mainly because of its high sensitivity providing information on markers of neurons, myelin, energy metabolism and abundance in the brain (van der Graaf 2010; Bluml 2013).

By the end of the 1990s, we have seen a steady increase in the magnetic field strengths used for MRI research, as well as for routine clinical applications. The clinical benefits of increased signal-to-noise ratio (SNR) that at 3T is twice compared to standard 1.5 T MR consist in the possibility to combined morphological and functional high-field MR methods, such as functional MR, metabolic imaging, and diffusion-weighted imaging (Trattnig et al. 2012; Balchandani and Naidich 2015). During the early 2000s another important step was taken with the advent of UHF 7T MR systems for human clinical research. The major advantages of the UHF 7T compared to lower field strength can be summarized as an increased SNR allowing higher spatial resolution and reduced scanning times, an increased sensitivity to differences in tissue magnetic susceptibility at the micro/mesoscopic scale introducing a new contrast mechanism and an increased spectral resolution for localized MR spectroscopy. Therefore, 7T MR systems have the potential to improve lesion detection revealing anatomical abnormalities that would remain unresolved at lower field strenghts, enhance lesion characterization, improve treatment planning, increase depiction of different metabolites and help to discover mechanisms underlying disease (Moser et al. 2012; van der Kolk et al. 2013;; Umutlu et al. 2014; Balchandani and Naidich 2015; Trattnig et al. 2016).

1.2 7T MR Imaging

During recent years, the number of UHF 7T MR scanners in the world has increased to about 60. This rapid increase indicates the growing interest in UHF MRI produced by preliminary (Tkác et al. 2001; Yacoub et al. 2001; Pfeuffer et al. 2002; Terpstra et al. 2002) and more recent (Triantafyllou et al. 2005; Krug et al. 2008; Laule et al. 2008; Nakada et al. 2008; Yao et al. 2009; Kollia et al. 2009; van der Zwaag et al. 2009) results in morphological detail (De Ciantis et al. 2015; De Ciantis et al 2016; Springer et al. 2016; Trattnig et al. 2016), functional imaging capability (Beisteiner et al. 2011; Goncalves et al. 2015) and other biochemical information (Zaiss et al. 2015; Biller et al. 2016). Although not widely used clinically at this time, an increasing number of research sites worldwide have access to 7T MRI scanner. Since the signal of the body tissue is determined by the static magnetic field B_0, UHF 7T MR is expected to yield an improvement in increase SNR that grows linearly with field strength, contrast to noise ratio (CNR) and spatial resolution (Vaughan et al. 2001; Ugurbil et al. 2003; Wargo et al. 2013) compared to 1.5T or 3T (Yacoub et al. 2005). However, several limitations exist due to technical complexity related directly to the UHF strength and the fact that not all previously advanced techniques applied to lower field strengths can be transformed directly to 7T.

1.2.1 Advantages of 7T MRI

In the past few years, 7T MRI has been used for in vivo brain imaging, providing several advantages (van der Kolk et al. 2013; Umutlu et al. 2014; Balchandani and Naidich 2015). Compared to conventional field strengths, the major advantages of the 7T can be summarized as an increased SNR allowing higher spatial resolution and reduced scanning time. The increase in spatial resolution promises to reveal anatomical and pathological details that were not determined by lower-field MRI. High magnetic field strength also affects the relaxation times of tissues, T1 and $T2^*$ in particular (Bottomley et al. 1984; Karamat et al. 2016). The shortened $T2^*$-values are related to the increased magnetic susceptibility effects that scale linearly with magnetic field strength. The shortening of the $T2^*$ time constant at UHF MRI makes it more sensitive to the presence of calcium and iron in microbleeds and hemorrhages. This leads to an improved depiction rate

of microbleeds in patients (Conijn et al. 2011; Brundel et al. 2012) detection of small venules (Tallantyre et al. 2008; Ge et al. 2008) and recognition of deep brain structures (Cho et al. 2010; Lenglet et al. 2012).

1.2.2 Challenges of 7T MRI

The technical issues include inhomogeneity of B_0 and B_1, errors in chemical shift localization, and increased deposition of RF power within the patient (Balchandani and Naidich 2015; Karamat et al. 2016). These cause image artifacts, limit section number/spatial coverage. In MR imaging, this results in distortion of both the geometry and the intensity of images. In MR spectroscopy B_0 changes among voxels manifest as spectral shifts causing broadening of metabolite peaks. It also makes it difficult the use of selective frequency pulses designed for spectral band specific data sampling. The intensity distortions caused by B_0 inhomogeneity also make lipids and water suppression more problematic. To combat this effect, more powerful referencing schemes, advanced B_0 shimming, and decreased voxel size are required. B_1 inhomogeneity is one of the most difficult problems to solve. This is caused by the shortening of the RF wavelength. The RF operating becomes comparable with the diameter of the human head, resulting in severe reduction of B_1 strength in the brain periphery compared with the center (Vaughan et al. 2001). The chemical Shift Localization Error (CSLE) is the measure of spatial offset in precise location with RF frequency and resonance frequency of the metabolite in MR spectroscopy within VOI. Because CSLE is linearly proportional to the frequency shift, the increase of CSLE reduce the performance of conventional 1H MRS sequences reducing the volume in which MR spectroscopy can be done at 7T. Another challenge for UHF imaging is related to the increased RF power deposition and tissue heating measured as Specific Absorption Rate (SAR), which theoretically increases with the square of B_0 (Zwanenburg et al. 2013; Balchandani and Naidich 2015; Karamat et al. 2016; Tiberi et al. 2016).

1.2.3 Patients Experience, Risk and Physiological Side Effects

Risks at 7T scanner are similar to those for lower-field MRI systems (Cosottini et al. 2014; Balchandani and Naidich 2015; Karamat et al. 2016). However, there are some additional patient comforts and safety considerations related to 7T MRI scanner.

Noise levels, SAR exposure, and peripheral nerve stimulation can be minimized by observance of safety guidelines established by health authority and institutional safety committees.

Acoustic noise is produced by bulk vibrations in gradient coils. The UHF MR systems have been verified to work within specified comfort levels in terms of decibel (dB) thanks to the use of noise dampening, noise insulation, and encapsulation and design specific MR sequences bring noise down to comfortable levels. Moreover, the application of earplugs and addictional pads covering the ears, placed within the RF coil cage, can further reduce the acoustic noise.

During the MR examination, RF energy deposition within the patient, quantified as the SAR exposure, is inspected by SAR monitor systems installed on the scanner to ensure that the sequences do not exceed safety limits and to guarantee the thermal safety of the patient (Collins et al. 2004).

To date, metallic implants are a contraindication for volunteer subjects and patients referred for 7T examinations. However, several research are studying the implantable devices to allow a scanning of higher number of subjects at 7T (Shellock FG. www.mrisafety.com; Dula et al. 2014; Feng et al. 2015).

1.2.4 Anatomical Brain Imaging

In the paste, researchers focused their studies on ex vivo imaging to obtain the highest resolutions despite acquisition with long scan durations (Wieshmann et al. 1999; Soria et al. 2011; Geyer et al. 2011).

Over the past several years, ultra-high-field 7T MR imaging has been available for in vivo human brain imaging. In vivo 7T MR imaging can improve the detection and characterization of abnormalities associated with a wide range of neurologic disorders,

including epilepsy, cortical malformation, brain tumors, multiple sclerosis, Alzheimer disease/dementia, and neuropsychiatric disorders (Yuh et al. 2006; Thomas et al. 2008; Kollia et al. 2009; Kerchner GA. 2011; Henry et al. 2011; Grabner et al. 2012; van der Kolk et al. 2013; Umutlu et al. 2014; Balchandani and Naidich 2015; De Ciantis et al. 2015; De Ciantis et al. 2016).

1.2.5 Epilepsy

From 20 to 40% of epileptic patients are drug resistant. The absence of a structural lesion on MRI still represents a challenge for surgical management, as it entails a poorer prognosis in both children and adults (Berkovic et al. 1995; Zentner et al. 1996; Mosewich et al. 2000; Tellez-Zenteno et al. 2010; Zwanenburg et al. 2013). Although epileptogenic lesions, mainly focal cortical dysplasia (FCD), have been demonstrated in 30–50% of histopathology specimens of MRI-negative patients (Chapman et al. 2005; Alarcon et al. 2006; McGonigal et al. 2007; Bien et al. 2009; Seo et al. 2009; Bernasconi et al. 2011; Wang et al. 2013), 16-43% of patients referred for presurgical assessment have negative brain MRI (Berg et al. 2003; McGonigal et al. 2007; Bien et al. 2009; Duncan 2010). With the improved SNR and novel contrast mechanisms available for the UHF MRI, 7T may give additional diagnostic information in patients with cryptogenic epilepsy in which no structural epileptic focus can be found at 3 T and 1.5 T. The added diagnostic value of 7T, compared to lower field strengths, has been demonstrated for FCD (De Ciantis et al. 2016; Colon et al. 2016), polymicrogyria (De Ciantis et al. 2015), vascular malformations (Schlamann et al 2010), hippocampal sclerosis (Henry et al. 2011; Breyer et al. 2012).

1.2.6 Brain Tumors

Ultra-high-field 7T MRI may be applied in different ways to better visualize brain tumor pathology. Clinically, the principal advantages of UHF include improved specificity, better sensitivity for signal-starved compounds, and the ability to detect, quantify and monitoring tumor activity and the effects of treatment (Lupo et al. 2009). Tumour heterogeneity and improvement in spatial localization have been observed with high-resolution T2-weighted and T2*-weighted imaging. The tumor evaluations can benefit from the use of

susceptibility-weighted image (SWI) that allowing the visualization of microvasculature, can detect the microbleeds associated with long-term effects of radiation or disclosure hemosiderin deposits associated with bleeding within tumours or metastases (Bian et al. 2014). Moreover SWI improving the appearance of cerebral veins reveals also the vascular distribution and the possible neovascularisation in primary brain tumours (Moenninghoff et al. 2009). Furthermore, in SWI the spatial resolution and susceptibility sensitivity improve the detection of cavernomas but also of cavernous hemangioma in the presence of a developmental venous anomaly. Additionally, several studies have reported an increase in contrast agent effects at higher field strength in brain tumours, compared to a lower field (Chang KH et al 1994; Akeson et al 1997; Nobauer-Huhmann et al. 2002; Krautmacher et al. 2005) and using even less dose of contrast agent (Noebauer-Huhmann et al. 2015). To date, 7T could help in determine the expansion of tumour in areas surrounding the tumour core, the differentiation between necrotic primary brain tumours, between necrotic metastases and cerebral abscesses and the differentiation between radionecrosis and tumour recurrence (van der Kolk et al. 2013).

1.3 7T MR Spectroscopy: ^{1}H MRS

Higher signal-to-noise ratio and spectral resolution at high magnetic fields have enabled significant gains in the quantification of a wide range of metabolites in the brain using in vivo Hydrogen 1 (^{1}H) MRS (Tkáč et al. 2001; Tkáč and Gruetter 2005; Grams et al. 2011). The chance to perform in vivo ^{1}H MRS in the human brain at 7T and the substantial improvements in sensitivity and spectral resolution were first shown in 2001 (Tkáč et al. 2001). Since then, only few clinical applications were published until 2010, which is mainly related to technical challenges associated with the 7T MRS (Moser et al. 2012; Posse et al. 2013). In particular, the delay in the development of in vivo high field MRS can be attributed to safety considerations, hardware limitations, high performance gradients and procedures to correct magnetic field inhomogeneity (Takahashi et al. 2003; Vaughan et al. 2001). Anyhow, in the past few years several clinical papers has been published describing advantages of 7T MRS in specific brain deseases, e.g., multiple sclerosis (Srinivasan et al. 2010) brain tumors (Li et al. 2015a,b) and epilepsy (Pan et al. 2015)

allowing the quantification of more metabolites than at lower field strengths (Tkáč et al. 2009) unless the use of special editing (Bogner et al. 2012) or 2D-MRS techniques (Thomas et al. 2001). In theory, high magnetic fields are helpful for ^{1}H MRS due to increased SNR, increased spatial and temporal resolution, increased spectral dispersion, simplification of J-coupled spectral patterns and a large chemical shift (Ugurbil et al. 2003). Numerous studies described gains in quantification precision at 3T or 4T compared to 1.5 T (Bartha et al. 2000; Gonen et al. 2001), at 7T compared to 3T (Mekle et al. 2009) and at 7T compared to 4T (Tkáč et al. 2009). Gains in sensitivity have also been reported for ^{1}H spectroscopic imaging at 7T compared to 1.5T (Otazo et al. 2006). However, these benefits are reduced by other factors resulting from high-field MRI, such as increased T2 signal decay, chemical shift dispersion error (CSDE), eddy current artefacts, J-modulation anomalies, increased magnetic susceptibility, limitations in design homogeneous and sensitive radiofrequency coils, B0 and B1 inhomogeneities and also safety issues, may decrease spectral resolution and minimize quantitation accuracy (Tosetti et al. 2006; Bogner et al. 2012). In the last few years, several groups have developed new methods to solve some of these limitations (Bogner et al. 2012; Moser et al. 2012). Some have used short echo time (TE) sequences to prevent excessive signal loss of short T2 components (Henning et al. 2009; Avdievich et al. 2009; Hetherington et al. 2010; Považan et al. 2015). CSDE has been reduced by the application of adiabatic refocusing pulses (Scheenen et al. 2008; Xu et al. 2008; Balchandani et al. 2008) or by the omission of selective refocusing pulses (Henning et al. 2009; Hetherington et al. 2010). Variations in the transmit B1 field have also been reduced by adiabatic pulses (Scheenenet al. 2008; Xu D et al. 2008; Balchandani et al. 2008), the omission of refocusing pulses (Henning et al. 2009; Hetherington et al. 2010) and by the use of multichannel transmit coils (Hetherington et al. 2010). Other groups have enhanced the suppression of subcutaneous lipid signals (Balchandani and Spielman 2008; Henning et al. 2009; Hetherington et al. 2010). Some researchers have optimized the detection of specific brain metabolites [e.g. glutamate, glutamine, glutathione, serine, taurine, scyllo-inositol, and glucose] (Tkáč et al., 2001; Choi et al. 2009; Henning et al. 2009; Snyder and Wilman 2010; Lally et al. 2016). Forthermore, in some cases, some limitations led to increased specific absorption rate (SAR) constraints (Scheenen et al. 2008; Henning et al. 2009). Currently, at 7T, around 18 metabolites can be mesured faithfully (Tkáč et al. 2001; Tkáč et al. 2009).

1.3.1 Single Voxel MRS

Single voxel technique is a type of in vivo spectroscopy. The underlying basic principles is to use mutually orthogonal slice-selective pulses and design the pulse sequences to collect only the echo signal from the voxel in space where all three slices intersect. Therefore, the single voxel techniques generate a cubic-based volume (voxel) for a region to be sampled with MRS (Zhu and Barker 2011). Similar pulse sequences as used at 1.5 or 3T can also be used for 7 T, such as stimulated echo acquisition mode (STEAM) (Frahm et al 1989) or point resolved spectroscopy (PRESS) (Bottomley 1987) sequences. However, results may not always be optimal if directly using a 1.5T or 3T protocol at 7T. Although PRESS has a theoretical factor of two higher S/N than STEAM, PRESS requires a much longer echo time and suffers from a higher chemical shift artifact than STEAM. Furthermore usage of either fully (Localization by Adiabatic SElective Refocusing - LASER) (Slotboom and Bovee 1995; Garwood and DelaBarre 2001) or partially (semi-LASER) (Scheenen et al. 2008a,b) adiabatic pulse sequences have been proposed for in vivo MRS. Over the last few years, the partially adiabatic semi-LASER sequence has become widespread, since it involves fewer RF pulses, and hence lower SAR, than fully adiabatic sequences (Penner and Bartha 2004; Pradha et al. 2015; Oz and Tkáč 2011). A recent study at 7T has shown a more than two-fold increase in SNR when using semi-LASER as opposed to the non-adiabatic STEAM sequence (Boer et al. 2011).

1.3.2 7T ^{1}H MRS in Brain Tumors and Epilepsy

Because 7T MRS has had to overcome several major technical challenges (Moser et al. 2012; Posse et al. 2013), most prior studies are methodological. In the past few years several groups have discussed the quantification of human brain metabolites in healthy volunteers by 1H MRS at ultrahigh magnetic fields emphasizing the precision and accuracy of metabolites quantification. To date there are around 18 metabolites identified using the 7T MRS (Tkáč et al. 2009; Bogner et al. 2012). These data indicate a great potential of in vivo 1H MRS at 7T to reveal new information about the neurochemistry of human brain under normal and pathological conditions. Scientific papers offering the specific advantages of 7T MRS in detecting metabolites in brain deseases such as tumors

(Li et al. 2015a,b; Emir et al. 2016; Trattnig et al. 2016) and epilepsy (Cai et al. 2012; Pan et al. 2013a,b; Pan et al. 2015) have only recently been published. Our knowledge of metabolites quantification in brain deseases are based on previously studies performed at lower fields strengths (Graaf 2010; Zhu and Barker 2011; Lupo et al. 2011; Oz et al. 2014; Verma et al. 2016).

In a study by Emir et al. (2016), single voxel 7T MRS offered increased sensitivity and specificity for onco-marker 2-hydroxyglutarate (HG) quantification and other metabolites associated, with implications for monitoring response treatment. Pan et al. (2013) developed a selective homonuclear polarization transfer sequence to measure thalamic GABA in controls and epilepsy patients at 7T. This study has been motivated by the central role of GABA in the hyperexcitability of epileptic brain and the ongoing clinical evaluation of a thalamic stimulator for the treatment of intractable epilepsy. Further, Cai et al. (Cai et al. 2012) demonstrated the increase of GABA concentration in the visual cortex of rodents and humans with Gabapentin admininistration used for the treatment of neuropathic pain and seizures.

In another study Pan and colleagues (Pan et al. 2013) demonstrated that MR spectroscopy imaging provides information in the identification of seizure onset regions in patients candidate for epilepsy surgery.

1.4 The Specific Absorption Rate (SAR)

The Specific Absorption Rate is defined as the radio-frequency (RF) power absorbed per unit of mass of a tissue, and is measured in watts per kilogram (W/kg). The RF power deposition theoretically increased as the square of B_0. The increase of RF energy deposition and of its spatial variability is due to the higher operating frequency of the UHF MR system. The SAR describes the potential for heating of the patient's tissue due to the application of the RF energy necessary to produce the MR signal (van Osch and Webb 2014). The management of SAR is a critical issue in MR, especially at UHF strengths. At UHF, the energy deposition due to the RF field increases and its distribution inside the subject becomes extremely inhomogeneous (Collins et al. 1998; Vaughan et al. 2001; Collins 2009; Kraff et al. 2015). Therefore, during 7T MR exames, RF energy deposition within the patient is closely monitored by SAR monitors to ensure that the sequences used

do not exceed the conservative safety limits imposed. The International Electrotechnical Commission (IEC) states a 1gram average (SAR 1g) of 8W/kg maximum for the head during 5 minutes, or a 3.2 W/kg whole head average SAR during 10 minutes (International Electrotechnical Commission. International Standard. Medical electrical equipment 2010). However, SAR estimation presents some drawbacks, such as 1) the monitoring of forward and reflected power is performed in real time, but offers no capability for SAR prediction, 2) the global SAR is determined by empirical formulation and thus it is not subject-specific because subject anatomy and subject position with respect to the transmitting coil are not taken into account, 3) local SAR is not evaluated. Moreover, it has been shown that global SAR estimation routines differ from system to system: thus, they should not be taken as the primary and only way to evaluate MR safety (Tiberi et al. 2016). Therefore in order to enhance safety of both adults and children imaged at 7T, Tiberi and colleagues suggested to predict SAR exposure by combining B1+ in vivo measurements with electromagnetic simulations.

1.5 References

1. Akeson P, Vikhoff B, Stahlberg F et al. Brain lesion contrast in MR imaging - dependence on field strength and concentration of gadodiamide injection in patients and phantoms. Acta Radiol 1997;38:14–18.
2. Alarcon G, Valentin A, Watt C, et al. Is it worth pursuing surgery for epilepsy in patients with normal neuroimaging? J Neurol Neurosurg Psychiatry 2006;77:474–480.
3. Avdievich NI, Pan JW, Baehring JM, Spencer DD, Hetherington HP. Short echo spectroscopic imaging of the human brain at 7T using transceiver arrays. Magn. Reson. Med. 2009; 62(1): 17–25.
4. Balchandani P, Naidich TP. Ultra-High-Field MR Neuroimaging. AJNR Am J Neuroradiol. 2015 Jul;36(7):1204-15.
5. Balchandani P, Pauly J, Spielman D. Interleaved narrow-band PRESS sequence with adiabatic spatial-spectral refocusing pulses for H-1 MRSI at 7T. Magn. Reson. Med. 2008; 59(5): 973–979.

6. Balchandani P, Spielman D. Fat suppression for H-1 MRSI at 7T using spectrally selective adiabatic inversion recovery. Magn. Reson. Med. 2008; 59(5): 980–988.

7. Bartha R, Drost DJ, Menon RS, Williamson PC. Comparison of the quantification precision of human short echo time (1)H spectroscopy at 1.5 and 4.0 Tesla. Magn Reson Med 2000;44:185–192.

8. Beisteiner, R., Robinson, S., Wurnig, M., Hilbert, M., Merksa, K., Rath, J., Hollinger, I., Klinger, N., Marosi, C., Trattnig, S., Geissler, A. Clinical fMRI: Evidence for a 7T benefit over 3T. NeuroImage 2011; 57, 1015-1021.

9. Berg AT, Vickrey BG, Langfitt JT, et al. The multicenter study of epilepsy surgery: recruitment and selection for surgery. Epilepsia 2003;44:1425–1433.

10. Berkovic SF, McIntosh AM, Kalnins RM, et al. Preoperative MRI pre- dicts outcome of temporal lobectomy: an actuarial analysis. Neurology 1995;45:1358–1363.

11. Bernasconi A, Bernasconi N, Bernhardt BC, et al. Advances in MRI for 'cryptogenic' epilepsies. Nat Rev Neurol 2011;7:99–108.

12. Bian W, Hess CP, Chang SM, Nelson SJ, Lupo JM. Susceptibility- weighted MR imaging of radiation therapy-induced cerebral mi- crobleeds in patients with glioma: a comparison between 3T and 7T. Neuroradiology. 2014;56(2):91–6.

13. Bien CG, Szinay M, Wagner J, et al. Characteristics and surgical out- comes of patients with refractory magnetic resonance imaging-nega- tive epilepsies. Arch Neurol 2009;66:1491–1499.

14. Biller, A., Badde, S., Nagel, A., Neumann, J.O., Wick, W., Hertenstein, A., Bendszus, M., Sahm, F., Benkhedah, N., Kleesiek, J. Improved Brain Tumor Classification by Sodium MR Imaging: Prediction of IDH Mutation Status and Tumor Progression. AJNR Am J Neuroradiol 2016; 37, 66-73.

15. Bluml S. Magnetic Resonance Spectroscopy: Basics. In: Bluml S, Panigrahy A (eds) MR spectroscopy of pediatric brain disorders. Springer, New York, Heidelberg, Dordrecht, London, 2013 pp 11-23.

16. Boer VO, van Lier AL, Hoogduin JM, Wijnen JP, Luijten PR, Klomp DW. 7-T (1) H MRS with adiabatic refocusing at short TE using radiofrequency focusing with a dual-channel volume transmit coil. NMR Biomed 2011;24:1038–46.

17. Bogner, W., Gruber, S., Trattnig, S., Chmelik, M. High-resolution mapping of human brain metabolites by free induction decay (1)H MRSI at 7 T. NMR Biomed 2012;25, 873-882.

18. Bottomley PA, Edelstein WA, Foster TH, Adams WA. In vivo solvent-suppressed localized hydrogen nuclear magnetic resonance spectroscopy: a window to metabolism? Proc Natl Acad Sci U S A. 1985 Apr;82(7):2148-52.

19. Bottomley PA, Foster TH, Argersinger RE, Pfeifer LM. A review of normal tissue hydrogen NMR relaxation times and relaxation mechanisms from 1–100 MHz: dependence on tissue type, NMR frequency, temperature, species, excision, and age. Med Phys 1984;11(4):425–48.

20. Bottomley PA. Selective volume method for performing localized NMR Spectroscopy, U.S. Patent 4,480,228, October 30, 1984; Bottomley PA. Spatial localization in NMR spectroscopy in vivo. Ann NY Acad Sci. 1987;508:333–348.

21. Breyer T, Wanke I, Maderwald S, et al. Imaging of patients with hippocampal sclerosis at 7 Tesla: initial results. Acad Radiol 2012;17:421–26

22. Brundel M, Heringa SM, de Bresser J, Koek HL, Zwanen- burg JJM, Jaap Kappelle L, Luijten PR, Biessels GJ. High prevalence of cerebral microbleeds at 7T MRI in patients with early Alzheimer's disease. J Alzheimers, 2012 Jan; 31(2):259–263.

23. Cai K, Nanga RP, Lamprou L, Schinstine C, Elliott M, Hariharan H, Reddy R, Epperson CN. The impact of gabapentin administration on brain GABA and glutamate concentrations: a 7T ^{1}H-MRS study. Neuropsychopharmacology. 2012 Dec;37(13):2764-71.

24. Chang KH, Ra DG, Han MH et al. Contrast enhancement of brain-tumors at different MR field strengths - comparison of 0.5-T and 2.0-T. Am J Neuroradiol 1994; 15:1413–1419

25. Chapman K, Wyllie E, Najm I, et al. Seizure outcome after epilepsy surgery in patients with normal preoperative MRI. J Neurol Neurosurg Psychiatry 2005;76:710–713.

26. Cho ZH, Min H, Oh S, Han JY, Park CW, Chi JG, Kim YB, Paek SH, Lozano AM, Lee KH. Direct visualization of deep brain stimulation targets in Parkinson disease with the use of 7T magnetic resonance imaging. J Neurosurg. 2010, 113(3):639–647.

27. Choi CH, Dimitrov I, Douglas D, Zhao CG, Hawesa H, Ghose S, Tamminga CA. Invivo detection of serine in the human brain by proton magnetic resonance spectroscopy (H-1-MRS) at 7 Tesla. Magn. Reson. Med. 2009; 62(4): 1042–1046

28. Collins CM, Li S, Smith MB. SAR and B1 field distributions in heterogeneous human head model within a birdcage coil. Magn Reson Med 1998;40:846–856.

29. Collins CM, Liu W, Wang J, Gruetter R, Vaughan JT, Ugurbil K, Smith MB. Temperature and SAR calculations for a human head within volume and surface coils at 64 and 300 MHz. J Magn Reson Imaging 2004; 19:650–656.

30. Collins CM. Numerical field calculations considering the human subject for engineering and safety assurance in MRI. NMR Biomed 2009; 22:919–926.

31. Colon AJ, van Osch MJ, Buijs M, Grond JV, Boon P, van Buchem MA, Hofman PA.

32. Conijn MMA, Geerlings MI, Biessels GJ, Takahara T, Witkamp TD, Zwanenburg JJM, Luijten PR, Hendrikse J. Cerebral microbleeds on MR imaging: Comparison be- tween 1.5 and 7T. Am J Neuroradiol. 2011, 32(6):1043– 1049

33. Cosottini M, Frosini D, Biagi L, Pesaresi I, Costagli M, Tiberi G, Symms M, Tosetti M. Short-term side-effects of brain MR examination at 7 T: a single-centre experience. Eur Radiol. 2014 Aug;24(8):1923-8.

34. Damadian R. Tumor detection by nuclear magnetic resonance. Science. 1971 Mar 19;171(3976):1151-53.

35. De Ciantis A, Barba C, Tassi L, Cosottini M, Tosetti M, Costagli M, Bramerio M, Bartolini E, Biagi L, Cossu M, Pelliccia V, Symms MR, Guerrini R. 7T MRI in focal epilepsy with unrevealing conventional field strength imaging. Epilepsia. 2016 Mar;57(3):445-54.

36. De Ciantis A, Barkovich AJ, Cosottini M, Barba C, Montanaro D, Costagli M, Tosetti M, Biagi L, Dobyns WB, Guerrini R. Ultra-high-field MR imaging in polymicrogyria and epilepsy. AJNR Am J Neuroradiol. 2015 Feb;36(2):309-16.

37. Detection superiority of 7 T MRI protocol in patients with epilepsy and suspected focal cortical dysplasia. Acta Neurol Belg. 2016 Sep;116(3):259-69.

38. Dula AN, Virostko J, Shellock FG. Assessment of MRI issues at 7 T for 28 implants and other objects. AJR Am J Roentgenol. 2014 Feb;202(2):401-5.

39. Duncan JS. Imaging in the surgical treatment of epilepsy. Nat Rev Neurol 2010;6:537–550.

40. Edelstein WA, Hutchison JM, Johnson G, Redpath T. Spin warp NMR imaging and applications to human whole-body imaging. Phys Med Biol. 1980 Jul;25(4):751-6.

41. Emir UE, Larkin SJ, de Pennington N, Voets N, Plaha P, Stacey R, Al-Qahtani K, Mccullagh J, Schofield CJ, Clare S, Jezzard P, Cadoux-Hudson T, Ansorge O. Noninvasive Quantification of 2-Hydroxyglutarate in Human Gliomas with IDH1 and IDH2 Mutations. Cancer Res. 2016 Jan 1;76(1):43-9.

42. European Federation of Neurological Societies Task Force. The future of magnetic resonance-based techniques in neurology. Eur J Neurol. 2001;8(1):17–25.

43. Feng DX, McCauley JP, Morgan-Curtis FK, Salam RA, Pennell DR, Loveless ME, Dula AN. Evaluation of 39 medical implants at 7.0 T. Br J Radiol. 2015;88(1056):20150633.

44. Frahm J, Bruhn H, Gyngell ML, Merboldt KD, Hänicke W, Sauter R. Localized high-resolution proton NMR spectroscopy using stimulated echoes: initial applications to human brain in vivo. Magn Reson Med. 1989 Jan;9(1):79-93.

45. Garwood M, DelaBarre L. The return of the frequency sweep: designing adiabatic pulses for contemporary NMR. J Magn Reson. 2001;153:155–177

46. Ge Y, Zohrabian VM, Grossman RI. Seven-Tesla magnetic resonance imaging: new vision of microvascular abnormal- ities in multiple sclerosis. Arch Neuro. 2008, 65(6):812– 816.

47. Geyer S, Weiss M, Reimann K, Lohmann G, Turner R. Microstructural Parcellation of the Human Cerebral Cortex - From Brodmann's Post-Mortem Map to in vivo Mapping with High-Field Magnetic Resonance Imaging. Front Hum Neurosci. 2011 Feb 18;5:19.

48. Goncalves, N.R., Ban, H., Sanchez-Panchuelo, R.M., Francis, S.T., Schluppeck, D., Welchman, A.E. 7 tesla FMRI reveals systematic functional organization for binocular disparity in dorsal visual cortex. J Neurosci 2015; 35, 3056-3072.

49. Gonen O, Gruber S, Li BS, Mlynarik V, Moser E. Multivoxel 3D proton spectroscopy in the brain at 1.5 versus 3.0 T: signal-to-noise ratio and resolution comparison. AJNR Am J Neuroradiol 2001;22:1727–1731.

50. Grabner G, Nöbauer I, Elandt K, et al. Longitudinal brain imaging of five malignant glioma patients treated with bevacizumab using susceptibility-weighted magnetic resonance imaging at 7 T. Magn Reson Imaging 2012;30:139 – 47

51. Grams AE, Brote I, Maderwald S, Kollia K, Ladd ME, Forsting M, Gizewski ER. Cerebral magnetic resonance spectroscopy at 7 Tesla: standard values and regional differences. Acad Radiol. 2011 May;18(5):584-7.

52. Hanstock CC, Rothman DL, Prichard JW, Jue T, Shulman RG. Spatially localized 1H NMR spectra of metabolites in the human brain. Proc Natl Acad Sci U S A. 1988 Mar;85(6):1821-5.

53. Hendee WR, Morgan CJ. Magnetic resonance imaging. Part I--physical principles. West J Med. 1984 Oct;141(4):491-500.

54. Henning A, Fuchs A, Murdoch JB, Boesiger P. Slice-selective FID acquisition, localized by outer volume suppression (FIDLOVS) for H-1-MRSI of the human brain at 7 T with minimal signal loss. NMR Biomed. 2009; 22(7): 683–696.

55. Henry TR, Chupin M, Lehericy S, et al. Hippocampal sclerosis in temporal lobe epilepsy: findings at 7 T. Radiology 2011;261: 199 –209.

56. Hetherington HP, Avdievich NI, Kuznetsov AM, Pan JW. RF shimming for spectroscopic localization in the human brain at 7T. Magn. Reson. Med. 2010; 63: 9–19.

57. International Electrotechnical Commission. International Standard. Medical electrical equipment - Part 2-33: particular requirements for the safety of magnetic resonance equipment for medical diagnosis. Edition 2.2. 60601-2-33:2010.

58. Karamat MI, Darvish-Molla S, Santos-Diaz A. Opportunities and Challenges of 7 Tesla Magnetic Resonance Imaging: A Review. Crit Rev Biomed Eng. 2016;44(1-2):73-89.

59. Kerchner GA. Ultra-high field 7T MRI: a new tool for studying Alzheimer's disease. J Alzheimers Dis 2011;26 (suppl3):91–95.

60. Kollia K, Maderwald S, Putzki N, Schlamann M, Theysohn JM, Kraff O, Ladd ME, Forsting M, Wanke I. First clinical study on ultra-high-field MR imaging in patients with multiple sclerosis: comparison of 1.5 T and 7 T. Am. J. Neuroradiol. 2009; 30(4): 699–702.

61. Kraff O, Fischer A, Nagel AM, Christoph M, Ladd ME. MRI at 7 Tesla and above: demonstrated and potential capabilities. J Magn Reson Imaging 2015;41:13–33.

62. Krautmacher C, Willinek WA, Tschampa HJ et al. Brain tumors: full- and half-dose contrast-enhanced MR imaging at 3.0T compared with 1.5T - initial experience. Radiology. 2005;237:1014–1019.

63. Krug R, Carballido-Gamio J, Banerjee S, Burghardt AJ, Link TM, Majumdar S. Invivo ultra-high-field magnetic resonance imaging of trabecular bone microarchitecture at 7 T. J. Magn. Reson. Imaging 2008; 27(4): 854–859.

64. Kumar A, Welti D, Ernst RR. NMR Fourier zeugmatography. J Magn Reson. 1975;18:69-83.

65. Lally N, An L, Banerjee D, Niciu MJ, Luckenbaugh DA, Richards EM, Roiser JP, Shen J, Zarate CA Jr, Nugent AC. Reliability of 7T (1) H-MRS measured human prefrontal cortex glutamate, glutamine, and glutathione signals using an adapted echo time optimized PRESS sequence: A between- and within-sessions investigation. J Magn Reson Imaging. 2016 Jan;43(1):88-98.

66. Laule C, Kozlowski P, Leung E, Li DK, Mackay AL, Moore GR. Myelin water imaging of multiple sclerosis at 7 T: correlations with histopathology. Neuroimage 2008; 40(4): 1575–1580.

67. Lenglet C, Abosch A, Yacoub E, de Martino F, Sapiro G, Harel N. Comprehensive in vivo mapping of the human basal ganglia and thalamic connectome in individuals using 7T MRI. PLoS ONE. 2012, 7(1):e29153.

68. Li Y, Larson P, Chen AP, Lupo JM, Ozhinsky E, Kelley D, Chang SM, Nelson SJ. Short-Echo Three-Dimensional H-1 MR Spectroscopic Imaging of Patients With Glioma at 7 Tesla for Characterization of Differences in Metabolite Levels. J Magn Reson Imaging. 2015a;41(5):1332-41.

69. Li Y, Park I, Nelson SJ. Imaging tumor metabolism using in vivo magnetic resonance spectroscopy. Cancer J. 2015b;21(2):123-8.

70. Lupo JM, Banerjee S, Hammond KE, Kelley DA, Xu D, Chang SM, Vigneron DB, Majumdar S, Nelson SJ. GRAPPA-based susceptibility- weighted imaging of normal volunteers and patients with brain tumor at 7 T. Magn. Reson. Imaging 2009; 27(4): 480–488.

71. Lupo JM, Li Y, Hess CP, Nelson SJ. Advances in ultra-high field MRI for the clinical management of patients with brain tumors. Curr Opin Neurol. 2011 Dec;24(6):605-15.

72. McGonigal A, Bartolomei F, Regis J, et al. Stereoelectroencephalogra- phy in presurgical assessment of MRI-negative epilepsy. Brain 2007;130:3169–3183.

73. Mekle R, Mlynárik V, Gambarota G, Hergt M, Krueger G, Gruetter R. MR spectroscopy of the human brain with enhanced signal intensity at ultrashort echo times on a clinical platform at 3T and 7T. Magnetic Resonance in Medicine 2009;61:1279–1285.

74. Moenninghoff C, Maderwald S, Theysohn JM, Kraff O, Ladd ME, El Hindy N, van de Nes J, Forsting M, Wanke I. Imaging of adult astrocytic brain tumours with 7T MRI: preliminary results. Eur. Radiol. 2009; 20(3): 704–713

75. Moser E, Stahlberg F, Ladd ME, Trattnig S. 7-T MR--from research to clinical applications? NMR Biomed. 2012 May;25(5):695-716

76. Mosewich RK, So EL, O'Brien TJ, et al. Factors predictive of the out- come of frontal lobe epilepsy surgery. Epilepsia 2000;41:843–849.

77. Nakada T, Matsuzawa H, Igarashi H, Fujii Y, Kwee IL. Invivo visualization of senile-plaque-like pathology in Alzheimer's disease patients by MR microscopy on a 7 T system. J. Neuroimaging 2008; 18(2): 125–129.

78. Nobauer-Huhmann IM, Ba-Ssalamah A, Mlynarik V et al. Magnetic resonance imaging contrast enhancement of brain tumors at 3 tesla versus 1.5 tesla. Investig Radiol. 2002;37:114–119.

79. Noebauer-Huhmann IM, Szomolanyi P, Kronnerwetter C, Widhalm G, Weber M, Nemec S, Juras V, Ladd ME, Prayer D, Trattnig S. Brain tumours at 7T MRI compared to 3T-contrast effect after half and full standard contrast agent dose: initial results. Eur Radiol. 2015;25:106–112.

80. Otazo R, Mueller B, Ugurbil K, Wald L, Posse S. Signal-to-noise ratio and spectral linewidth improvements between 1.5 and 7 Tesla in proton echo-planar spectroscopic imaging. Magn Reson Med 2006;56:1200–1210.

81. Oz G, Alger JR, Barker PB, Bartha R, Bizzi A, Boesch C, Bolan PJ, Brindle KM, Cudalbu C, Dinçer A, Dydak U, Emir UE, Frahm J, González RG, Gruber S, Gruetter R, Gupta RK, Heerschap A, Henning A, Hetherington HP, Howe FA, Hüppi PS, Hurd RE, Kantarci K, Klomp DW, Kreis R, Kruiskamp MJ, Leach MO, Lin AP, Luijten PR, Marjańska M, Maudsley AA, Meyerhoff DJ, Mountford CE, Nelson SJ, Pamir MN, Pan JW, Peet AC, Poptani H, Posse S, Pouwels PJ, Ratai EM, Ross BD, Scheenen TW, Schuster C, Smith IC, Soher BJ, Tkáč I, Vigneron DB, Kauppinen RA; MRS Consensus Group. Radiology. Clinical proton MR spectroscopy in central nervous system disorders. Radiology. 2014 Mar;270(3):658-79.

82. Oz G, Tkáč I. Short-echo, single-shot, full-intensity proton magnetic resonance spectroscopy for neurochemical profiling at 4 T: validation in the cerebellum and brainstem. Magn Reson Med. 2011 Apr;65(4):901-10.

83. Pan JW, Duckrow RB, Gerrard J, Ong C, Hirsch LJ, Resor SR Jr, Zhang Y, Petroff O, Spencer S, Hetherington HP, Spencer DD. 7T MR spectroscopic imaging in the localization of surgical epilepsy. Epilepsia. 2013a;54(9):1668-78.

84. Pan JW, Duckrow RB, Spencer DD, Avdievich NI, Hetherington HP. Selective homonuclear polarization transfer for spectroscopic imaging of GABA at 7T. Magn Reson Med. 2013b;69(2):310-6.

85. Pan JW, Kuzniecky RI. Utility of magnetic resonance spectroscopic imaging for human epilepsy. Quant Imaging Med Surg. 2015;5(2):313-322.

86. Penner J and Bartha R. Semi-LASER 1H MR Spectroscopy at 7 Tesla in Human Brain: Metabolite Quantification Incorporating Subject-Specific Macromolecule Removal. Magn Reson Med. 2014 Jul 31. [Epub ahead of print].

87. Pfeuffer J, Adriany G, Shmuel A, Yacoub E, Van De Moortele PF, Hu X, Ugurbil K. Perfusion-based high-resolution functional imaging in the human brain at 7 Tesla. Magn. Reson. Med. 2002; 47(5): 903–911.

88. Posse S, Otazo R, Dager SR, Alger J. MR spectroscopic imaging: principles and recent advances. J Magn Reson Imaging. 2013 Jun;37(6):1301-25.

89. Považan M, Hangel G, Strasser B, Gruber S, Chmelik M, Trattnig S, Bogner W. Mapping of brain macromolecules and their use for spectral processing of (1)H-MRSI data with an ultra-short acquisition delay at 7 T. Neuroimage. 2015 Nov 1;121:126-35.

90. Pradhan S, Bonekamp S, Gillen JS, Rowland LM, Wijtenburg SA, Edden RA, Barker PB. Comparison of single voxel brain MRS AT 3T and 7T using 32-channel head coils. Magn Reson Imaging. 2015 Oct;33(8):1013-8.

91. Scheenen TW, Heerschap A, Klomp DW. Towards 1H-MRSI of the human brain at 7T with slice-selective adiabatic refocusing pulses. MAGMA 2008b;21: 95–101.

92. Scheenen TW, Klomp DW, Wijnen JP, Heerschap A. Short echo time 1H-MRSI of the human brain at 3T with minimal chemical shift displacement errors using adiabatic refocusing pulses. Magn Reson Med 2008a;59:1–6.

93. Schlamann M, Maderwald S, Becker W, et al. Cerebral cavernous hemangiomas at 7 Tesla: initial experience. Acad Radiol 2010;17:3–6.

94. Seo JH, Noh BH, Lee JS, et al. Outcome of surgical treatment in non- lesional intractable childhood epilepsy. Seizure 2009;18:625–629.

95. Shellock FG. www.mrisafety.com.

96. Slotboom J, Bovee W. Adiabatic slice selective RF pulses and a single-shot adiabatic localization pulse sequence. Concepts Magn Reson 1995;7:193–217.

97. Snyder J, Wilman A. Field strength dependence of PRESS timings for simultaneous detection of glutamate and glutamine from 1.5 to 7 T. J. Magn. Reson. 2010; 203(1): 66–72.

98. Soria G, De Notaris M, Tudela R, Blasco G, Puig J, Planas AM, Pedraza S, Prats-Galino A. Improved assessment of ex vivo brainstem neuroanatomy with high-resolution MRI and DTI at 7 Tesla. Anat Rec (Hoboken). 2011 Jun;294(6):1035-44.

99. Speck O, Tempelmann C. Human 7T MRI: first clinical and neuro- scientific applications. Neuroradiol J. 2010;23(5):535–46.

100. Springer, E., Dymerska, B., Cardoso, P.L., Robinson, S.D., Weisstanner, C., Wiest, R., Schmitt, B., Trattnig, S. Comparison of Routine Brain Imaging at 3 T and 7 T. Invest Radiol 2016; 51(8):469-82.

101. Srinivasan, R., Ratiney, H., Hammond-Rosenbluth, K.E., Pelletier, D., Nelson, S.J., 2010. MR spectroscopic imaging of glutathione in the white and gray matter at 7 T with an application to multiple sclerosis. Magnetic resonance imaging 28, 163-170.

102. Takahashi M, Uematsu H, Hatabu H. MR imaging at high magnetic fields. Eur J Radiol. 2003 Apr;46(1):45-52.

103. Tallantyre EC, Brookes MJ, Dixon JE, Morgan PS, Evangelou N, Morris PG. Demonstrating the perivascular dis- tribution of MS lesions in vivo with 7T MRI. Neurology. 2008, 70(22):2076–2078.

104. Tellez-Zenteno JF, Hernandez Ronquillo L, Moien-Afshari F, et al. Surgical outcomes in lesional and non-lesional epilepsy: a systematic review and meta-analysis. Epilepsy Res 2010;89:310–318.

105. Terpstra M, Ugurbil K, Gruetter R. Direct in vivo measurement of human cerebral GABA concentration using MEGA-editing at 7 Tesla. Magn. Reson. Med. 2002; 47(5): 1009–1012.

106. Thomas BP, Welch EB, Niederhauser BD, et al. High-resolution 7T MRI of the human hippocampus in vivo. J Magn Reson Imaging 2008;28:1266 –72.

107. Thomas MA, Yue K, Binesh N, Davanzo P, Kumar A, Siegel B, Frye M, Curran J, Lufkin R, Martin P, Guze B. Localized two-dimensional shift correlated MR spectroscopy of human brain. Magn Reson Med. 2001 Jul;46(1):58-67.

108. Tiberi G, Costagli M, Biagi L, De Ciantis AD, Fontana N, Stara R, Symms MR, Cosottini M, Guerrini R, Tosetti M. SAR prediction in adults and children by

combining measured B1+ maps and simulations at 7.0 Tesla. J Magn Reson Imaging. 2016 Oct;44(4):1048-55.

109. Tkác I, Andersen P, Adriany G, Merkle H, Ugurbil K, Gruetter R. In vivo 1H NMR spectroscopy of the human brain at 7 T. Magn. Reson. Med. 2001; 46(3): 451–456.

110. Tkáč I, Gruetter R. Methodology of H NMR Spectroscopy of the Human Brain at Very High Magnetic Fields. Appl Magn Reson. 2005 Mar;29(1):139-157.

111. Tkáč I, Oz G, Adriany G, Ugurbil K, Gruetter R. In vivo 1H NMR spectroscopy of the human brain at high magnetic fields: metabolite quantification at 4T vs. 7T. Magn Reson Med. 2009;62:868–879

112. Tosetti, M., Schirmer, T., D'Alesio, V., Di Costanzo, A., & Scarabino, T. (2006). 3.0 T MR spectroscopy. In High Field Brain MRI: Use in Clinical Practice. (pp. 51-65). Springer Berlin Heidelberg.

113. Trattnig S, Springer E, Bogner W, Hangel G, Strasser B, Dymerska B, Cardoso PL, Robinson SD. Key clinical benefits of neuroimaging at 7T. Neuroimage. 2016 Nov 13. pii: S1053-8119(16)30651-6. doi: 10.1016/j.neuroimage.2016.11.031. [Epub ahead of print].

114. Trattnig S, Zbýň S, Schmitt B, Friedrich K, Juras V, Szomolanyi P, Bogner W. Advanced MR methods at ultra-high field (7 Tesla) for clinical musculoskeletal applications. Eur Radiol. 2012 Nov;22(11):2338-46.

115. Trattnig, S., Bogner, W., Gruber, S., Szomolanyi, P., Juras, V., Robinson, S., Zbýň, Š., Haneder, S. Clinical applications at ultrahigh field (7 T). Where does it make the difference? NMR in Biomed. 2016 29(9):1316-34.

116. Triantafyllou C, Hoge RD, Krueger G, Wiggins CJ, Potthast A, Wiggins GC, Wald LL. Comparison of physiological noise at 1.5 T, 3 T and 7 T and optimization of fMRI acquisition parameters. Neuroimage 2005; 26(1): 243–250.

117. Ugurbil K, Adriany G, Andersen P, Chen W, Garwood M, Gru- etter R, Henry PG, Kim SG, Lieu H, Tkac I, Vaughan T, Van De Moortele PF, Yacoub E, Zhu XH. Ultrahigh field magnetic resonance imaging and spectroscopy. Magn Reson Imaging. 2003;21(10):1263–81.

118. Umutlu L, Ladd ME, Forsting M, Lauenstein T. 7 Tesla MR imaging: opportunities and challenges. Rofo. 2014 Feb;186(2):121-9.

119. van der Graaf M. In vivo magnetic resonance spectroscopy: basic methodology and clinical applications. Eur Biophys J (2010) 39:527–540.

120. van der Kolk AG, Hendrikse J, Zwanenburg JJ, Visser F, Luijten PR. Clinical applications of 7 T MRI in the brain. Eur J Radiol. 2013 May;82(5):708-18.

121. van der Zwaag W, Francis S, Head K, Peters A, Gowland P, Morris P, Bowtell R. fMRI at 1.5, 3 and 7T: characterising BOLD signal changes. Neuroimage 2009; 47(4): 1425–1434.

122. van Osch MJP and Webb AG. Safety of Ultra-High Field MRI/ What are the Specific Risks? Curr Radiol Rep 2014;2:61.

123. Vaughan JT, Garwood M, Collins CM, Liu W, DelaBarre L, Adria- ny G, Andersen P, Merkle H, Goebel R, Smith MB, Ugurbil K. 7T vs. 4T: RF power, homogeneity, and signal-to-noise comparison in head images. Magn Reson Med. 2001;46(1):24–30.

124. Verma A, Kumar I, Verma N, Aggarwal P, Ojha R. Magnetic resonance spectroscopy - Revisiting the biochemical and molecular milieu of brain tumors. BBA Clin. 2016 Apr 12;5:170-8.

125. Wang ZI, Alexopoulos AV, Jones SE, et al. The pathology of mag- netic-resonance-imaging-negative epilepsy. Mod Pathol 2013;26:1051–1058.

126. Wargo CJ, Moore J, Gore JC. A comparison and evaluation of reduced-FOV methods for multi-slice 7T human imaging. Magn Reson Imaging. 2013;31(8):1349–59.

127. Wieshmann UC, Symms MR, Mottershead JP, MacManus DG, Barker GJ, Tofts PS, Revesz T, Stevens JM, Shorvon SD. Hippocampal layers on high resolution magnetic resonance images: real or imaginary? J Anat. 1999 Jul;195 (Pt 1):131-5.

128. Xu D, Cunningham CH, Chen AP, Li Y, Kelley DAC, Mukherjee P, Pauly JM, Nelson SJ, Vigneron DB. Phased array 3D MR spectroscopic imaging of the brain at 7 T. Magn. Reson. Imaging, 2008; 26(9): 1201–1206.

129. Yacoub E, Shmuel A, Pfeuffer J, Van De Moortele PF, Adriany G, Andersen P, Vaughan JT, Merkle H, Ugurbil K, Hu X. Imaging brain function in humans at 7 Tesla. Magn. Reson. Med. 2001; 45(4): 588–594.

130. Yacoub, E., Van De Moortele PF, Shmuel A, Ugurbil K. Signal and noise characteristics of Hahn SE and GE BOLD fMRI at 7 T in humans. Neuroimage. 2005;24(3):738–50.

131. Yao B, Li TQ, Gelderen P, Shmueli K, de Zwart JA, Duyn JH. Susceptibility contrast in high field MRI of human brain as a function of tissue iron content. NeuroImage 2009; 44(4): 1259–1266.

132. Yuh WT, Christoforidis GA, Koch RM, et al. Clinical magnetic res- onance imaging of brain tumors at ultrahigh field: a state-of-the- art review. Top Magn Reson Imaging 2006;17:53– 61.

133. Zaiss, M., Windschuh, J., Paech, D., Meissner, J.E., Burth, S., Schmitt, B., Kickingereder, P., Wiestler, B., Wick, W., Bendszus, M., Schlemmer, H.P., Ladd, M.E., Bachert, P., Radbruch, A. Relaxation- compensated CEST-MRI of the human brain at 7T: Unbiased insight into NOE and amide signal changes in human glioblastoma. Neuroimage 2015; 112, 180-188.

134. Zentner J, Hufnagel A, Ostertun B, et al. Surgical treatment of extratemporal epilepsy: clinical, radiologic, and histopathologic find- ings in 60 patients. Epilepsia 1996;37:1072–1080.

135. Zhu H, Barker PB. MR spectroscopy and spectroscopic imaging of the brain. Methods Mol Biol. 2011;711:203-26.

136. Zwanenburg JJM,van der Kolk AG, Luijten PR. Ultra-high-field MR imaging: research tool or clinical need? PET Clin. 2013, 8:311–328.

Chapter 2.

Ultra-high field MR imaging in polymicrogyria and epilepsy

Alessio De Ciantis[1], A. James Barkovich[2], Mirco Cosottini[3,4], Carmen Barba[1], Domenico Montanaro[5], Mauro Costagli[6], Michela Tosetti[6], Laura Biagi[6], William B. Dobyns[7] and Renzo Guerrini[1,6]

[1]Pediatric Neurology Unit, A. Meyer Children's Hospital, University of Florence, Florence, 50139, Italy. [2]Department of Radiology and Biomedical Imaging, University of California San Francisco, San Francisco, CA 94143, USA. [3]Department of Translational Research and New Technologies in Medicine and Surgery, University of Pisa, Pisa, 56124, Italy. [4]IMAGO7 Foundation, Pisa, 56128, Italy. [5]Fondazione CNR/Regione Toscana, U.O.S. Neuroradiologia, Pisa, 56124, Italy. [6]IRCCS Stella Maris Foundation, Pisa, 56128, Italy. [7]Center for Integrative Brain Research, Seattle Children's Hospital, Seattle, WA 98101, USA.

This chapter has been published in American Journal of Neuroradiology, vol. 36, pp. 309-316.

2.1 Abstract

2.1.1 Background And Purpose

Polymicrogyria is a malformation of cortical development that is often identified in children with epilepsy or delayed development. We investigated in vivo the potential of 7T imaging in characterizing polymicrogyria to determine whether additional features could be identified.

2.1.2 Materials and Methods

Ten adult patients with polymicrogyria previously diagnosed using 3T MRI underwent additional imaging at 7T. We assessed polymicrogyria according to topographic pattern, extent, symmetry and morphology. Additional imaging sequences at 7T included 3D T2* susceptibility-weighted angiography and 2D tissue border enhancement FSE inversion-recovery. Minimum intensity projections were used to assess the potential of the susceptibility-weighted angiography sequence for depiction of cerebral veins.

2.1.3 Results

At 7T, we observed perisylvian polymicrogyria that was bilateral in six patients, unilateral in three and diffuse in one. Four of the six bilateral abnormalities had been deemed as unilateral at 3T. While 3T imaging revealed two morphologic categories (coarse, delicate), 7T susceptibility-weighted angiography images disclosed a uniform ribbon-like pattern. Susceptibility-weighted angiography revealed numerous dilated superficial veins in all polymicrogyric areas. Tissue border enhancement imaging depicted a hypointense line corresponding to the gray/white interface providing a high definition of the borders and, thereby, improving detection of the polymicrogyric cortex.

2.1.4 Conclusion

7T imaging reveals more anatomical details of polymicrogyria compared to 3T conventional sequences, with potential implications for diagnosis, genetic studies and surgical treatment of associated epilepsy. Abnormalities of cortical veins may suggest a role of vascular dysgenesis in pathogenesis.

2.2 Introduction

Polymicrogyria is a malformation of the cerebral cortex secondary to abnormal migration and postmigrational development.[1] It is characterized by an excessive number of abnormally small gyri separated by shallow sulci, associated with fusion of the overlying molecular layer (layer 1) of the cerebral cortex.[2] This combination of features produces a characteristic appearance of irregularity at both the cortical surface and cortical-white matter junction.[3,4] Its pathogenesis is still poorly understood, and its histopathology, clinical features, topographic distribution and imaging appearance are heterogeneous. Deficiencies in the understanding of this malformation result from both causal heterogeneity (causative factors include destructive events such as congenital infections,[5,6] in utero ischemia,[7] metabolic disorders and several gene mutations and copy number variations[1,8,9]) and the limited number of post-mortem examinations available.

The topographic distribution of polymicrogyria may be focal, multifocal, or diffuse, unilateral or bilateral, symmetrical or asymmetrical.[10-15] Polymicrogyria can occur as an isolated disorder or be associated with other brain abnormalities such as corpus callosum dysgenesis, cerebellar hypoplasia, schizencephaly, periventricular and subcortical heterotopia.[16,17]

Clinical manifestations of patients with polymicrogyria have a large spectrum, ranging from isolated selective impairment of cognitive function[18] to severe encephalopathy and intractable epilepsy[19]. The severity of neurologic manifestations and the age at presentation are in part influenced by extent and location of the cortical malformation but may also depend on its specific etiology.

Neuroimaging has a primary role in the diagnosis and classification of polymicrogyria due to its non-invasive nature. Imaging findings are variable and are primarily determined by

the morphology of the malformed cortex itself but also by the maturity of myelination and imaging related technical factors (slices thickness, gray-white matter contrast).[20] In addition, polymicrogyria-like patterns can be seen in certain malformations, such as tubulinopathies[21] and cobblestone malformations[22-24]; these have different histological appearances but similar MRI appearances to polymicrogyria, which can lead to false diagnoses.

Based on morphological characteristics, Barkovich[2,20] described the variable appearance of polymicrogyria on MRI and suggested that the gyral-sulcal dysmorphisms may be roughly divided into three main categories: *coarse* with thick, bumpy cortex and irregular surface in both the pial and gray-white junction sides; *delicate* with multiple small, fine gyri of thin cortex that remains thin even after myelination; and *sawtooth,* composed of thin microgyri separated by deep sulci (primarily seen in diffuse polymicrogyria and before myelination develops). However, numerous gradations of morphology exist within these groups. To date, neither functional nor etiologic associations have been inferred based on this imaging categorization of polymicrogyric cortex.

Over the last several years, ultra high-field (UHF) 7T MRI has been available for in vivo human brain imaging. In vivo 7T MRI can provide greater tissue type identification than is obtained in vitro without stains.[25] As a result of increased signal-to-noise ratio, enhanced image contrast and improved resolution, MR at 7T can visualize small anatomic structures not previously appreciated at lower fields.[25-28] As 7T MRI has already provided diagnostic benefits in different pathologies[28] such as multiple sclerosis,[29] cerebrovascular diseases (strokes, microbleeds),[30,31] aneurysms,[32] cavernous malformations,[33] brain tumors[34] and degenerative brain diseases like dementia and Parkinson's disease,[35,36] we tested the added value of 7T MRI in providing details of structural changes and their extent in ten patients with polymicrogyria with respect to conventional 3T imaging. We also addressed the limitations we encountered while exploring the polymicrogyric brain with 7T.

2.3 Material and Methods

2.3.1 Ethics Statement

Written informed consent was obtained from all patients and is recorded on file. The experimental protocol named "Evaluation of dysplastic cortical lesions and dysembryoplastic tumors using ultra-high field MRI target imaging" Project 133/11 was funded by the Pisa Foundation and approved by the local competent ethics committee and the Italian Ministry of Health. The procedures followed were in accordance with institutional guidelines and included an adverse event form.

2.3.2 Subjects

Between June 2013 and October 2013, we enrolled from our cortical malformations database ten adult patients (four men and six women) with polymicrogyria previously imaged at 3T. Exclusion criteria were age under 18 years and any contraindications to MRI scanning. Polymicrogyria, as assessed by previous 3T MR imaging, had been classified as bilateral perisylvian in two patients, unilateral perisylvian in seven patients, diffuse in one patient. Mean age was 30.1 years (range 21-53 years). Clinical details are described in On-line Table 1.

2.3.3 Data Acquisition

All ten patients were imaged at both 3T (General Electric Excite HDx, GE, Milwaukee, WI, U.S.A., equipped with an eight-channel head coil) and 7T (General Electric 950 MR scanner, equipped with a two-channel transmit/32channel-receive head coil (Nova Medical, Wilmington, MA USA). All participants received earplugs and a pair of pads covering the ears for limiting the acoustic noise.

The 3T MRI standard protocol included the following sequences: 3D T1-weighted fast spoiled gradient-echo (FSPGR), 2D T2 FLAIR, 2D T2-weighted FSE and 2D white matter suppressed FSE inversion-recovery (IR). The 7T MRI protocol included the following sequences: 3D T1-weighted FSPGR, 3D susceptibility-weighted angiography (SWAN), 2D

T2*-weighted targeted dual-echo gradient-echo (GRE), 2D T2-weighted FSE and 2D gray-white matter tissue border enhancement (TBE) FSE-IR. TBE is an IR sequence that employs an appropriate inversion time to produce images where the interface between two neighboring tissues of interest is hypointense, therefore tissue borders are clearly represented by dark lines. This effect is achieved by setting imaging parameters such that the neighboring tissues have magnetization with equal magnitude but out of phase; therefore the voxels containing a mixture of each tissue (that is, the tissue interface) possess minimal net signal.[37] Therefore the hypointense line marking tissue interface produced by TBE does not reflect any specific fiber structure. Details of imaging parameters for 3T and 7T imaging are shown in On-line Table 2.

In order to limit specific absorption rate (SAR) related problems, image distortions and stronger susceptibility phenomena related to UHF, whole brain 7T imaging included only SWAN and FSPGR sequences, with the remaining sequences targeting specific regions of interest using small FOV and a limited number of slices. To select the areas of interest for targeted imaging, we were guided by initial 7T whole brain sequences.

2.3.4 Data Analysis

All 7T images were independently assessed by three reviewers and later as a group to reach a consensus for eligibility. 3T and 7T images were assessed separately in each patient. Polymicrogyria was diagnosed when the combination of these characteristics was satisfied 1) the cortex had an irregular outer surface with an abnormal gyral pattern, 2) the cortex appeared thickened or overfolded and 3) the cortical-white matter junction was irregular.[38]

We reviewed all images for the following findings: 1) topographic pattern of polymicrogyria, 2) extent, 3) symmetry (if bilateral), 4) range of gyral-sulcal dysmorphisms and 5) associated abnormalities. We classified the topographic pattern according to the different patterns described in the literature: focal, bilateral frontal, bilateral perisylvian (which varies in extent of involvement), bilateral parieto-occipital and diffuse polymicrogyria.

The 3T and 7T images were assessed digitally with a GE workstation (Advantage 4.1). 3D images were reformatted in orthogonal planes to better evaluate the cortical thickening and to rule out partial volume artifacts.

The post-processing of SWAN images was performed using the minimum intensity projection algorithm (MinIP) and multiplanar reformation techniques. The MinIP algorithm has the characteristic of enhancing the visualization of veins while attenuating the signal from the brain tissue. Conversely, tissue border enhancement images do not require additional post-processing.

2.4 Results

All imaging sessions were well tolerated by the patients and no adverse events occurred. Brain MRI findings and clinical details of all patients are summarized in On-line Table 1.

At 3T we observed perisylvian polymicrogyria that was unilateral in seven patients and bilateral in two. Of the seven patients with unilateral polymicrogyria, six had multilobar involvement and in one only a portion of the Sylvian fissure was involved (Fig 1). One patient had diffuse polymicrogyria.

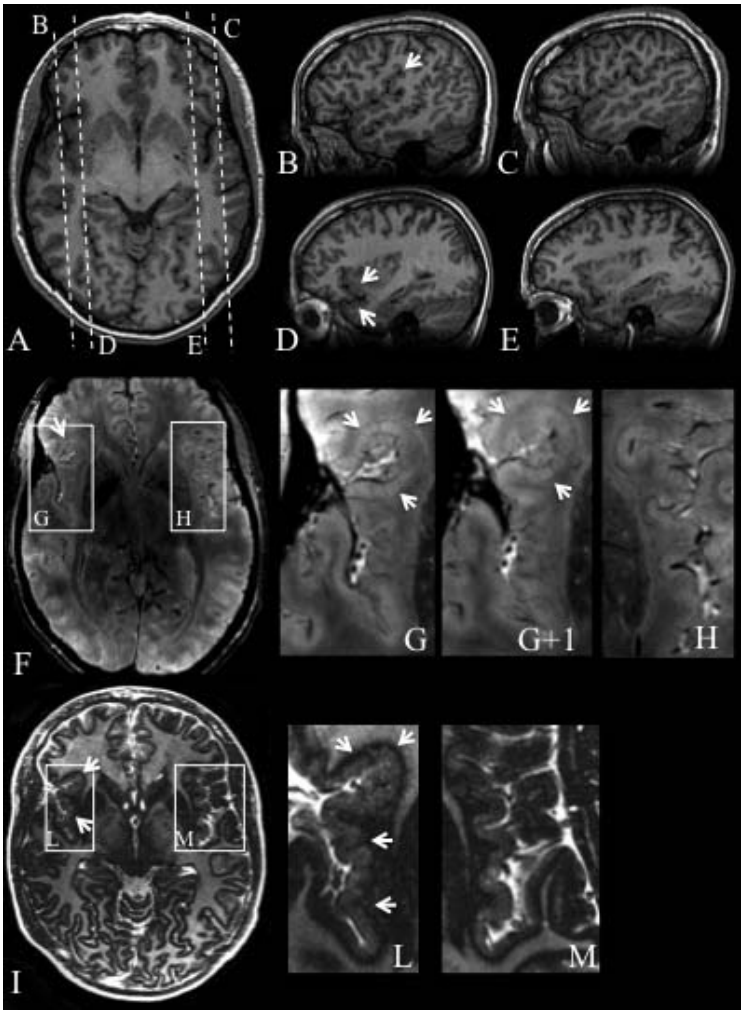

Fig 1. *Patient 8. 3T axial (A) and sagittal (B-E) 3D FSPGR, 7T 3D SWAN (F) and magnified images (G, G+1, H), 7T axial 2D TBE FSE-IR (I) and magnified images (L, M). Figure A shows mild cortical thickening in the right frontal operculum. Contiguous sagittal sections across the frontal operculum and the Sylvian fissure on the right (B, D) and left (C, E) side provide a better comparative view of the morphologic characteristics of malformed versus normal cortex. Figure B shows an abnormal right Sylvian fissure (arrow), which is vertically orientated, shortened and bordered by thick and irregular cortex. Figure D shows thickening of the cortex in the inferior frontal gyrus and superior temporal gyrus (arrows). Figure F and its two contiguous expanded views, from caudal (G) to rostral (G+1) provide ultra-high resolution details of the right frontal operculum which are not visible at 3T (A-E) substantiating the presence of polymicrogyric cortex. Figure H, which is a magnification of the homologous contralateral region, clearly enhances the appreciation of the difference in folding of the polymicrogyric and normal cortex. Figure I and magnifications (L, M) show a hypointense line representing the gray-white matter interface and provides a high definition of the polymicrogyric (L, arrows) and normal cortex (M) making it easier to appreciate irregularities in thickness and folding of the polymicrogyric cortex.*

A range of gyral-sulcal dysmorphisms emerged at 3T (Fig 2A; On-line Fig 1A) all falling into the categorization formulated by Barkovich,[2] with six out of ten patients having coarse appearance and the remaining four coarse together with delicate appearance.

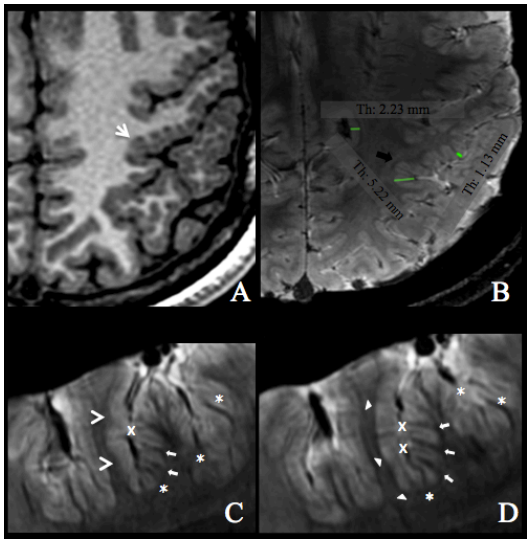

Fig 2. *Patients 1 (A, B) and 9 (C, D). Comparison of 3T axial 3D FSPGR (A) and 7T axial 3D SWAN (B) images. Contiguous 7T axial 3D SWAN acquisitions showing anatomic details of the polymicrogyric cortex (C, D). Figure A shows the "delicate" appearance of the polymicrogyric cortex in the left pre and post central sulci, characterized by multiple small and delicate gyri of thin cortex (arrow). Figure B discloses a thin and undulated polymicrogyric cortex, in which the spaces between microgyri are filled by thin white matter digitations, which have a low periodicity and are loosely packed. The gray-white matter junction is bordered by a thin hypointense line. 7T can therefore resolve the individual microgyri, revealing how grossly different morphologic characters (coarse or delicate) at 3T result in fact from variations of a common underlying morphologic pattern. Figure B shows examples of cortical thickness measurements of normal (2.23 mm) and polymicrogyric cortex (1.13 to 5.22 mm) using the straight-line distance measure between surface and depth of the cortex. Figure C and D have been chosen to show how SWAN images show details of cortical structures and allow to disentangle the structural units underlying the radiologic appearance of polymicrogyria. The typical undulated aspect is clearly detectable following the hypointense lines of the cortical border (arrowheads), which we assume to represent arcuate white matter fibers, the white matter digitations within the gyri (arrows), the small vessels joining the pial veins (asterisks) and the fused molecular layer (crosses).*

The thickness of the polymicrogyric cortex, measured with FSPGR imaging, ranged from 3.7 to 12 mm (thickness of the normal cortex at 3T ranged from 1.6 to 4 mm), with great variability even between adjacent cortical regions.

In three patients, polymicrogyria was an isolated abnormality while in the remaining seven patients additional subcortical abnormalities were detected: unilaterally (n=1) or bilaterally (n=4) dilated ventricles, unilateral (n=2) or bilateral (n=2) hippocampal abnormalities, absence of septum pellucidum (n=2), cavum vergae (n=1), unilateral periventricular nodular heterotopia (n=2) and unilateral open lip schizencephaly (n=1). White matter volume reduction was apparent under the polymicrogyric cortex in all patients. One patient exhibited left intraorbital cavernous hemangiomas and a left soft tissue hemangioma as well as hypertrophy of the right Sylvian and medullary veins.

7T provided additional details to 3T findings and revealed more extensive areas of polymicrogyria in all patients. In particular, in three patients (Patients 4, 7 and 8) in whom 3T FSPGR imaging had revealed unilateral polymicrogyria, 7T SWAN imaging confirmed a unilateral distribution but detected more extensive involvement (Fig 1). In three patients with bilateral polymicrogyria at 3T (Patients 1, 3 and 9), 7T SWAN revealed more extensive involvement. Four patients (Patients 2, 5, 6 and 10), who had been classified as having unilateral polymicrogyria at 3T, exhibited bilateral involvement at 7T (On-line Fig 2). In patient 2, 3T FSPGR showed left posterior polymicrogyria engaging the left temporo-insulo-parietal region and the medium and superior occipital gyri. 7T SWAN imaging disclosed that polymicrogyria also involved the right posterior insula. In patient 5, in whom 3T FSPGR showed left fronto-temporo-parietal polymicrogyria along the whole Sylvian fissure, 7T SWAN revealed polymicrogyria also in the right frontal operculum. In patients 6 and 10, the polymicrogyric cortex had right temporo-parietal distribution at 3T SPGR while 7T disclosed abnormal infolding and thickening of the left frontal operculum. In patient 10, 7T SWAN also showed that the polymicrogyria involved the area around the whole left Sylvian fissure, left anterior insula and left anterior temporal region.

The increased signal-to-noise ratio and the increased sensitivity to magnetic susceptibility effects on SWAN sequences at 7T combined to high-resolution images with enhanced intracortical contrast provided improved polymicrogyria detailing by making it possible to identify details in the entire cortex: the lowest part of the sulcus, the intermediate zone and the crown of the gyrus. The different categories of gyral and sulcal dysmorphisms seen at 3T (coarse, delicate, sawtooth) were not identifiable as such at 7T, in that SWAN images revealed a homogeneous morphologic character (Fig 2B; On-line Fig 1B). The malformed cortex, measured using SWAN imaging, was 0.78 to 7 mm thick (normal cortex was 1 to

2.89 mm), exhibiting an undulated profile at the gray/white matter junction and bordered by a thin hypointense line, which was considered to represent the arcuate white matter fibers. Within the abnormal cortex, small linear hypointense transcortical lines perpendicular to the cortical layers, probably representing the larger transcortical blood vessels, were present. The hypointense lines of the cortical border combined with those within the cortex contributed in generating the typical polymicrogyric appearance of the cortical ribbon at 7T (Fig 2C and D).

In all patients, SWAN imaging revealed numerous dilated superficial veins draining the deeper infoldings of polymicrogyria, which were not visible at 3T using conventional (FSPGR, FSE and IR) sequences. These large venous structures, which have been described previously,[39] appeared to be roughly proportional to the depth/size of the cortical infolding and extent of polymicrogyria (Fig 3).

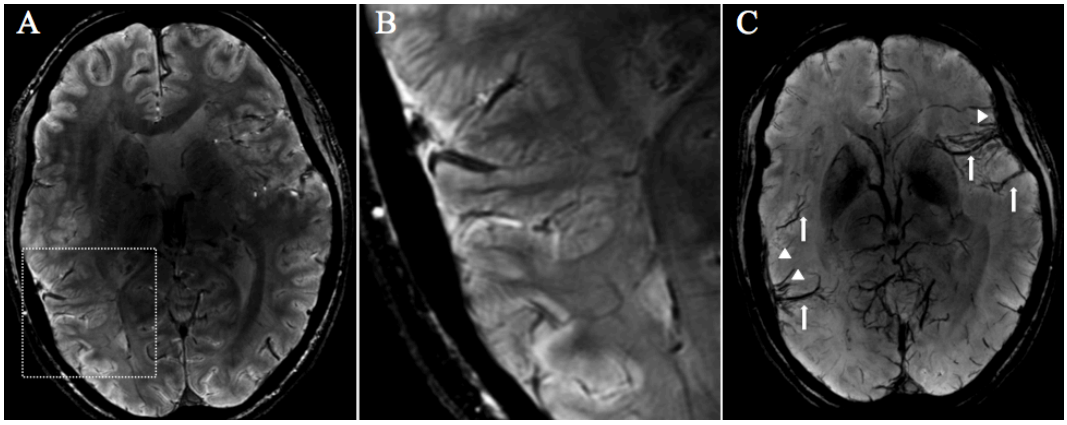

Fig 3. *Patient 9. 7T axial 3D SWAN (A, magnified in B) and its MinIP reconstruction (C). Image A shows bilateral polymicrogyria involving the left frontal operculum and Sylvian fissure and the right Sylvian fissure and temporal lobe. The magnified image B shows details of the polymicrogyric cortex in the right temporal lobe. MinIP reconstruction in C shows dilated superficial veins in correspondence of the polymicrogyric areas (arrowheads); the large vascular structures running through the polymicrogyric sulci (arrows) define the location and the extent of the malformation.*

In all patients, TBE imaging revealed a hypointense line corresponding to the gray/white matter interface, providing a high definition of the borders of the polymicrogyric cortex (On-line Fig 3 and 4). TBE imaging substantiated SWAN findings and, providing a precise topographical definition of the gray/white matter junction, made the examiner more confident about the extent of polymicrogyria, especially where the border between gray

and white matter was poorly defined or the polymicrogyric cortex merged with seemingly normal cortex (On-line Fig 3 and 4).

The diagnostic gain obtained at 7T originated from the improved image and contrast resolution of SWAN sequences and, to a lesser degree, from 2D GRE images. GRE sequences revealed cortical and pial veins, as well as small vessels inside the cortex, less precisely than SWAN. Using GRE, cortical layering was less defined, the arcuate white matter fibers could not be visualized and white matter digitations within the gyri were less conspicuous than observed using SWAN or TBE. GRE defined the complexity of cortical gyration better than SPGR but worse than SWAN and TBE. T2W FSE at 7T did not provide additional information with respect to the same sequence at 3T and had lower contrast and spatial resolution than GRE.

2.5 Discussion

Accurate MRI depiction of polymicrogyria has important implications for correlating clinical severity with the extent of cortical abnormality,[20,38,40] guiding genotyping of specific malformation patterns[1] and delineating the resection margins in patients who are candidates for epilepsy surgery.[41-44]

In this series, 7T SWAN imaging provided improved structural cortical details with more accurate information on cortical thickness, sulcal pattern and cerebral veins. At 7T, the polymicrogyric cortex exhibited a highly variable thickness, ranging from 0.78 to 7 mm, close to pathology specimen measures,[25] with bumpy inner and outer surfaces, broad gyri and shallow sulci.

7T SWAN imaging also allowed better qualitative assessment of sulcal patterns as compared to conventional 3T imaging. Thanks to high spatial resolution and increased contrast within the cortex of 7T SWAN imaging, the gyral-sulcal dysmorphisms of polymicrogyria[2] visible at 3T SPGR appeared as a highly characteristic undulated pattern of contiguous densely packed microgyri. The polymicrogyric cortex seen in some of the 3T FSPGR images as thick, rough and blurred was merely a poorly resolved image of more deeply undulating thin gyri, with the apparent cortical thickening generated by lower

contrast and resolution that results from conventional sequences and field strengths. The significance of the deeper undulations remains to be determined.

Combining 7T high spatial resolution together with 3D SWAN sequences we uncovered bilateral involvement in four patients who had been diagnosed as exhibiting unilateral abnormalities at 3T. In addition to the SWAN imaging, we used a custom-designed TBE sequence, which produced a hypointense line along the gray and white matter interface, thereby providing a high definition of the undulating polymicrogyric borders and, together with improved resolution on SWAN images, allowed improved differentiation from adjacent normal cortex. TBE images substantiated the extent of malformation observed using SWAN imaging and also revealed the borders of polymicrogyria in those areas where the gray/white matter junction was poorly defined or the polymicrogyric cortex merged with the normal cortex.

In addition to producing more accurate morphological details of the polymicrogyric cortex, SWAN imaging at 7T detected deoxygenated venous blood that allowed visualization of the superficial and deep cerebral veins. Although 3T SWAN can also visualize venous abnormalities, there is no previous report emphasizing this finding at 3T. At 7T, the polymicrogyric cortex was shown to harbor numerous dilated superficial veins, whose representation seemed to be roughly proportional to the extent and severity of the cortical malformation. The pial veins were visible as linear hypointensities, orthogonal to and penetrating into the cortex. Following the expected course of the sulci, the pial veins defined the complexity of cortical gyration revealing the contour of polymicrogyria. SWAN-MinIP images, which enhance the visualization of veins while attenuating the signal from the brain tissue, revealed large vascular structures running through the sulci, draining from the polymicrogyric cortex into the pial veins. These findings reinforce previous imaging observations pointing out anomalous venous drainage in dysplastic cortical areas.[39,45] On the other hand, although perfusion failure is a recognized cause of polymicrogyria, there is no reported neuropathological evidence of vascular malformations associated with it.[6,46-49]

Abnormal venous drainage might develop as a response to an event, such as cortical injury, during fetal development[50] and are probably the result of a lack of condensation of cortical veins with persistence of embryonic dural plexus tributaries.[45] Based on the prominence of vascular abnormalities in polymicrogyria, one may hypothesize that they are involved in its

etiopathogenesis. For instance, a causative role of venous abnormalities has been suggested in patients with Sturge-Weber syndrome and polymicrogyria in the region underlying pial angiomatosis.[38,51,52] One hypothesis concerning the cause of Sturge-Weber is that leptomeningeal vascular dysplasia leads to impaired perfusion, especially as regards microvenular drainage, which produces blood stasis with progressive hypoperfusion and ischemia.[53] Alternatively, cortical dysgenesis could result from the abnormal expression of a factor playing a role in both vascular and cortical development.[54] Based on the observation that cryogenic lesions in the cortex of neonatal rats can produce focal microgyria and subsequent abnormal vascularization, it has also been suggested that cortical venous abnormalities in polymicrogyria might be the consequence, and not the cause, of abnormal cortical development.[55] However, it is not clear that lesion-induced polymicrogyria in the normally agyric rat cortex is the same malformation as the polymicrogyria found in gyrencephalic humans.

Based on the frequent location of polymicrogyria in watershed vascular territories and on evidence of laminar necrosis in brain specimens[7,49,56-59] some authors have suggested that polymicrogyria might result from arterial ischemia during the second trimester of gestation. Due to lack of arterial sequences in our study, however, we could not exclude the presence of an arterial dysplasia in our patients, and can only speculate on arterial dysgenesis as a possible cause of pre-natal ischemia. In addition, we studied adult patients with normal or nearly normal cognitive function, whose main clinical problem was epilepsy. These clinical characteristics might have selected a subpopulation with a specific subtype of polymicrogyria or a specific etiology, which is certainly not representative of the larger population of individuals with polymicrogyria in which varied etiologic factors, other than vascular, might be prevalent.

Polymicrogyria and polymicrogyria-like malformations have indeed been associated with mutations of various genes, including COL18A1, PAX6, KIAA1279, RAB3GAP1, RAB3GAP2, TUBA1A, TUBB2B, TUBB3, TUBA8, TUBB5, TBR2, WDR62 and to different copy number variations.[8,60-64] However, paucity of neuropathological observations limits our ability to understand how comparable morphological changes are in these conditions. Moreover, the large majority of cases of polymicrogyria are not caused by alterations of any known gene. 7T MRI will hopefully make it possible to better evaluate and classify specific polymicrogyria phenotypes and, by reducing sample

heterogeneity, improve the approach to genetic studies, leading to a higher diagnostic yield. Genetic characterization of patients with polymicrogyria might ultimately lead to improved outcome prediction.[65] Quantitative measurements of abnormal sulcal patterns have made it possible to correlate morphological abnormalities with language impairment.[66] Future 7T functional MRI studies are needed to clarify the correlation between abnormal sulcal patterns and functional impairment.

About 78-87% of patients with polymicrogyria have epilepsy.[38,67] Associated epilepsy is often intractable, but only a limited number of patients are eligible for surgical treatment and invasive recordings are necessary in most in order to define eloquent cortex and the area to be removed.[41,43,44] Although the final surgical margins are determined by the use of depth electrode recordings or by corticography in the operating theatre, 7T MRI may help presurgical planning for patients with polymicrogyria-related epilepsy by providing a clearer assessment of the margins of the polymicrogyric cortex and revealing previously undetected bilateral abnormalities.

Although we demonstrated some obvious advantages offered by 7T, we also found limitations inherent its use. The protocols and acquisition methods we used for 3T and 7T MRI were different, and both relaxivity and susceptibility effects differ significantly at these different field strengths. In addition, optimal protocols at 7T have not yet been implemented. SWAN and TBE sequences were not included in our standard 3T MR protocol and could not be directly compared to 7T acquisitions. When imaged at conventional field strengths, patients with polymicrogyria are not evaluated with GRE images but primarily with FSPGR, FSE or IR sequences. At 7T the inhomogeneous RF energy deposition and the increased susceptibility effect may cause signal inhomogeneity or image distortion. In order to remain within the SAR limits and reduce image distortion and stronger susceptibility phenomena, we acquired targeted images with small FOV and a few slices focused on regions of interest at 7T. As a consequence, we did not image the entire brain, as it is usually done at lower field strength. In particular, in order not to exceed the SAR limits imposed by regulations (IEC EN 60601-2-33), for FSE it was possible to acquire 10 slices within one single acquisition, while for TBE 10 slices were acquired during two separate series of 5 slices each.

An additional limitation of our study is that none of our patients had undergone epilepsy surgery and no pathology and post-operative outcome were available to be correlated with

7T imaging. Furthermore, our MRI comparison was based on visual, qualitative analysis. Nevertheless, we found substantially more and different information at 7T that we hope will be useful in future analyses of patients with polymicrogyria.

2.6 Conclusions

UHF 7T imaging allows assessment of structural brain abnormalities that cannot be obtained from conventional MR imaging and represents an important tool for the diagnosis and characterization of polymicrogyria.

2.7 References

1. Barkovich AJ, Guerrini R, Kuzniecky RI, et al. A developmental and genetic classification for malformations of cortical development: update 2012. *Brain* 2012;135:1348-69
2. Barkovich AJ. MRI analysis of sulcation morphology in polymicrogyria. *Epilepsia* 2010;51:17-22
3. Barkovich AJ, Kuzniecky RI, Jackson GD, et al. A developmental and genetic classification for malformations of cortical development. *Neurology* 2005;65:1873-87
4. Harding B, Copp AJ. Malformations. In: Graham DI, Lantos PL, eds. Greenfield's Neuropathology 6th ed. London: Arnold; 1997:397-533
5. Barkovich AJ, Lindan CE. Congenital cytomegalovirus infection of the brain: imaging analysis and embryologic considerations. *AJNR Am J Neuroradiol* 1994;15:703-15
6. Crome L, France NE. Microgyria and cytomegalic inclusion disease in infancy. *J Clin Pathol* 1959;12:427-34
7. Barkovich AJ, Rowley H, Bollen A. Correlation of prenatal events with the development of polymicrogyria. *AJNR Am J Neuroradiol* 1995;16:822-27
8. Guerrini R, Parrini E. Neuronal migration disorders. *Neurobiol Dis* 2010;38:154-66

9. Robin NH, Taylor CJ, McDonald-McGinn DM, et al. Polymicrogyria and deletion 22q11.2 syndrome: window to the etiology of a common cortical malformation. *Am J Med Genet A* 2006;140:2416-25

10. Chang BS, Piao X, Bodell A, et al. Bilateral frontoparietal polymicrogyria: clinical and radiological features in 10 families with linkage to chromosome 16. *Ann Neurol* 2003;53:596-606

11. Chang BS, Piao X, Giannini C, et al. Bilateral generalized polymicrogyria (BGP): a distinct syndrome of cortical malformation. *Neurology* 2004;62:1722-28

12. Guerrini R, Dubeau F, Dulac O, et al. Bilateral parasagittal parietooccipital polymicrogyria and epilepsy. *Ann Neurol* 1997;41:65-73

13. Guerrini R, Genton P, Bureau M, et al. Multilobar polymicrogyria, intractable drop attack seizures, and sleep-related electrical status epilepticus. *Neurology* 1998;51:504-12

14. Guerrini R, Barkovich AJ, Sztriha L, et al. Bilateral frontal polymicrogyria: a newly recognized brain malformation syndrome. *Neurology* 2000;54:909-13

15. Kuzniecky R, Andermann F, Guerrini R. Congenital Bilateral Perisylvian Syndrome - Study of 31 Patients. *Lancet* 1993;341:608-12

16. Barkovich AJ. Morphologic characteristics of subcortical heterotopia: MR imaging study. *AJNR Am J Neuroradiol* 2000;21:290-95

17. Wieck G, Leventer RJ, Squier WM, et al. Periventricular nodular heterotopia with overlying polymicrogyria. *Brain* 2005;128:2811-21

18. Galaburda AM, Sherman GF, Rosen GD, et al. Developmental dyslexia: four consecutive patients with cortical anomalies. *Ann Neurol* 1985;18:222-33

19. Guerrini R, Dobyns WB, Barkovich AJ. Abnormal development of the human cerebral cortex: genetics, functional consequences and treatment options. *Trends Neurosci* 2008;31:154-62

20. Barkovich AJ. Current concepts of polymicrogyria. *Neuroradiology* 2010;52:479-87

21. Cushion TD, Dobyns WB, Mullins JG, et al. Overlapping cortical malformations and mutations in TUBB2B and TUBA1A. *Brain* 2013;136:536-48

22. Bahi-Buisson N, Poirier K, Boddaert N, et al. GPR56-related bilateral frontoparietal polymicrogyria: further evidence for an overlap with the cobblestone complex. *Brain* 2010;133:3194-209

23. Devisme L, Bouchet C, Gonzales M, et al. Cobblestone lissencephaly: neuropathological subtypes and correlations with genes of dystroglycanopathies. *Brain* 2012;135:469-82

24. Singer K, Luo R, Jeong SJ, et al. GPR56 and the developing cerebral cortex: cells, matrix, and neuronal migration. *Mol Neurobiol* 2013;47:186-96

25. Cho ZH, Kim YB, Han JY, et al. New brain atlas-mapping the human brain in vivo with 7.0 T MRI and comparison with postmortem histology: Will these images change modern medicine? *Int J Imag Syst Tech* 2008;18:2-8

26. Abosch A, Yacoub E, Ugurbil K, et al. An assessment of current brain targets for deep brain stimulation surgery with susceptibility-weighted imaging at 7 tesla. *Neurosurgery* 2010;67:1745-56

27. Metcalf M, Xu D, Okuda DT, et al. High-Resolution Phased-Array MRI of the Human Brain at 7 Tesla: Initial Experience in Multiple Sclerosis Patients. *J Neuroimaging* 2010;20:141-47

28. van der Kolk AG, Hendrikse J, Zwanenburg JJ, et al. Clinical applications of 7 T MRI in the brain. *Eur J Radiol* 2013;82:708-18

29. Tallantyre EC, Dixon JE, Donaldson I, et al. Ultra-high-field imaging distinguishes MS lesions from asymptomatic white matter lesions. *Neurology* 2011;76:534-39

30. Conijn MM, Geerlings MI, Biessels GJ, et al. Cerebral microbleeds on MR imaging: comparison between 1.5 and 7T. *AJNR Am J Neuroradiol* 2011;32:1043-49

31. Madai VI, von Samson-Himmelstjerna FC, Bauer M, et al. Ultrahigh-field MRI in human ischemic stroke--a 7 tesla study. *PloS one* 2012;7:e37631

32. Monninghoff C, Maderwald S, Wanke I. Pre-interventional assessment of a vertebrobasilar aneurysm with 7 tesla time-of-flight MR angiography. *Rofo* 2009;181:266-68

33. Dammann P, Barth M, Zhu Y, et al. Susceptibility weighted magnetic resonance imaging of cerebral cavernous malformations: prospects, drawbacks, and first experience at ultra-high field strength (7-Tesla) magnetic resonance imaging. *Neurosurg focus* 2010;29:E5

34. Lupo JM, Li Y, Hess CP, et al. Advances in ultra-high field MRI for the clinical management of patients with brain tumors. *Curr Opin Neurol* 2011;24:605-15

35. Cosottini M, Frosini D, Pesaresi I, et al. MR Imaging of the Substantia Nigra at 7 T Enables Diagnosis of Parkinson Disease. *Radiology* 2014;271:831-38

36. Kwon DH, Kim JM, Oh SH, et al. Seven-tesla magnetic resonance images of the substantia nigra in Parkinson disease. *Ann Neurol* 2012;71:267-77

37. Costagli M, Kelley DA, Symms MR, et al. Tissue Border Enhancement by inversion recovery MRI at 7.0 Tesla. *Neuroradiology* 2014;56:517-23

38. Leventer RJ, Jansen A, Pilz DT, et al. Clinical and imaging heterogeneity of polymicrogyria: a study of 328 patients. *Brain* 2010;133:1415-27

39. Barkovich AJ. Abnormal vascular drainage in anomalies of neuronal migration. *AJNR Am J Neuroradiol* 1988;9:939-42

40. Guerrini R, Dravet C, Raybaud C, et al. Epilepsy and focal gyral anomalies detected by MRI: electroclinico-morphological correlations and follow-up. *Dev Med Child Neurol* 1992;34:706-18

41. Chassoux F, Landre E, Rodrigo S, et al. Intralesional recordings and epileptogenic zone in focal polymicrogyria. *Epilepsia* 2008;49:51-64

42. Guerrini R. Polymicrogyria and epilepsy. *Epilepsia* 2010;51:10-12

43. Maillard L, Koessler L, Colnat-Coulbois S, et al. Combined SEEG and source localisation study of temporal lobe schizencephaly and polymicrogyria. *Clin Neurophysiol* 2009;120:1628-36

44. Ramantani G, Koessler L, Colnat-Coulbois S, et al. Intracranial evaluation of the epileptogenic zone in regional infrasylvian polymicrogyria. *Epilepsia* 2013;54:296-304

45. Thompson JE, Castillo M, Thomas D, et al. Radiologic-pathologic correlation polymicrogyria. *AJNR Am J Neuroradiol* 1997;18:307-12

46. Friede RL. Developmental neuropathology. Berlin: Springer-Verlag; 1989

47. Golden JA, Harding BN. Pathology and Genetics. Developmental Neuropathology. Basel: ISN Neuropath Press; 2004

48. Judkins AR, Martinez D, Ferreira P, et al. Polymicrogyria includes fusion of the molecular layer and decreased neuronal populations but normal cortical laminar organization. *J Neuropathol Exp Neurol* 2011;70:438-43

49. Marques Dias MJ, Harmant-van Rijckevorsel G, Landrieu P, et al. Prenatal cytomegalovirus disease and cerebral microgyria: evidence for perfusion failure, not disturbance of histogenesis, as the major cause of fetal cytomegalovirus encephalopathy. *Neuropediatrics* 1984;15:18-24

50. Pryor J, Setton A, Berenstein A. Venous anomalies and associated lesions. *Neurosurg Clin N Am* 1999;10:519-25

51. Simonati A, Colamaria V, Bricolo A, et al. Microgyria associated with Sturge-Weber angiomatosis. *Childs Nerv Syst* 1994;10:392-95

52. Terdjman P, Aicardi J, Sainte-Rose C, et al. Neuroradiological findings in Sturge-Weber syndrome (SWS) and isolated pial angiomatosis. *Neuropediatrics* 1991;22:115-20

53. Cagneaux M, Paoli V, Blanchard G, et al. Pre- and postnatal imaging of early cerebral damage in Sturge-Weber syndrome. *Pediatr Radiol* 2013;43:1536-39

54. Comi AM. Pathophysiology of Sturge-Weber syndrome. *J Child Neurol* 2003;18:509-16

55. Dvorak K, Feit J, Jurankova Z. Experimentally induced focal microgyria and status verrucosus deformis in rats-pathogenesis and interrelation. Histological and autoradiographical study. *Acta Neuropathol* 1978;44:121-29

56. Aeby A, Guerrini R, David P, et al. Facial hemangioma and cerebral corticovascular dysplasia: A syndrome associated with epilepsy. *Neurology* 2003;60:1030-32

57. Evrard P, Kadhim H, de Saint-Georges P, et al. Abnormal development and destructive processes of the human brain during the second half of gestation. In: Evrard P, Minkowski A, eds. Developmental Neurobiology. New York:Vevey-Raven Press;1989:21-41

58. Richman DP, Stewart RM, Caviness VS Jr. Cerebral microgyria in a 27-week fetus: an architectonic and topographic analysis. *J Neuropathol Exp Neurol* 1974;33:374-84

59. Suzuki M, Choi BH. Repair and reconstruction of the cortical plate following closed cryogenic injury to the neonatal rat cerebrum. *Acta Neuropathol* 1991;82:93-101

60. Abdollahi MR, Morrison E, Sirey T, et al. Mutation of the Variant alpha-Tubulin TUBA8 Results in Polymicrogyria with Optic Nerve Hypoplasia. *Am J Hum Genet* 2009;85:737-44

61. Breuss M, Heng JI, Poirier K,et al. Mutations in the beta-tubulin gene TUBB5 cause microcephaly with structural brain abnormalities. *Cell Rep* 2012;2:1554-62

62. Guerrini R, Dobyns WB. Malformations of cortical development: clinical features and genetic causes. *Lancet Neurol* June 14. [Epub ahead of print]

63. Jaglin XH, Chelly J. Tubulin-related cortical dysgeneses: microtubule dysfunction underlying neuronal migration defects. *Trends Genet* 2009;25:555-66

64. Poirier K, Saillour Y, Bahi-Buisson N, et al. Mutations in the neuronal ss-tubulin subunit TUBB3 result in malformation of cortical development and neuronal migration defects. *Hum Mol Genet* 2010;19:4462-73

65. Shain C, Ramgopal S, Fallil Z, et al. Polymicrogyria-associated epilepsy: a multicenter phenotypic study from the Epilepsy Phenome/Genome Project. *Epilepsia* 2013;54:1368-75

66. Im K, Pienaar R, Paldino MJ et al. Quantification and discrimination of abnormal sulcal patterns in polymicrogyria. *Cereb Cortex* 2013;23:3007-15

67. Guerrini R, Filippi T. Neuronal migration disorders, genetics, and epileptogenesis. *J Child Neurol* 2005;20:287-99

2.8 Supplemental On-Line Materials

Clinical details									MRI findings								
No	Age (yrs)/ sex	Cognitive level	Early dev	Neurological examination	Age at seizure onset (yrs)	Seizure type/freq	Epilepsy syndrome	EEG at the time of the study	Topographic pattern	Lateralization/ symmetry		PMG character		Vascular abnormalities		Associated abnormalities	
									3T/7T	3T	7T	3T	7T	3T	7T	3T	7T
1	21/F	Mild impairment	Severe language delay	Mild L hemiparesis	4	CPS/ remission since age 5 yrs	Focal	R T sharp waves, diffuse SW during HPN	Diffuse	Bilateral/ symmetric	Bilateral/ symmetric	Delicate/ coarse	Undulated profile	None	Increased number and dilatation of superficial veins in PMG cortex	Bilateral hippocampal malrotation, ventricular dilatation	Same as seen at 3T
2	33/M	Normal	Normal	Normal	16	CPS/ monthly	Focal	L T SW with possible contralateral spreading	Perisylvian	Unilateral	Bilateral/ asymmetric	Coarse	Undulated profile	None	Increased number and dilatation of superficial veins in PMG cortex	None	None
3	21/F	Normal	Mild language delay	Opercular syndrome	15	CPS/ monthly	Focal	Bilateral CT SW	Perisylvian	Bilateral/ asymmetric	Bilateral/ asymmetric	Coarse	Undulated profile	None	Increased number and dilatation of superficial veins in PMG cortex	None	None
4	33/M	Normal	Normal	Normal	16	CPS/ yearly	Focal	R hem spikes with possible contralateral spreading	Perisylvian	Unilateral	Unilateral	Delicate/ coarse	Undulated profile	None	Increased number and dilatation of superficial veins in PMG cortex	R T NH, cavum vergae, bilateral ventricular dilatation	Same as seen at 3T
5	24/M	Moderate impairment	Mild motor delay, moderate language delay	Mild R hemiparesis	4	Focal, atypical absences since age 4 yrs/ remission since age 6 yrs	ESES	L hem spikes with possible contralateral spreading	Perisylvian	Unilateral	Bilateral/ asymmetric	Coarse	Undulated profile	L intraorbital cavernous hemangiomas, L soft tissue hemangioma, R Sylvian vein hypertrophy, medullary veins hypertrophy	L intraorbital cavernous hemangiomas, L soft tissue hemangioma, R Sylvian vein hypertrophy, medullary veins hypertrophy, increased number and dilatation of superficial veins in PMG cortex	L hippocampal atrophy	Same as seen at 3T
6	21/M	Borderline functioning	Mild language delay	Dysarthria, dyspraxia, mild R hemiparesis	1	Focal seizures from age 1 to 7 yrs, negative myoclonus and atypical absences since age 6 yrs/ remission since age 9 yrs	Focal, ESES	Vertex spikes	Perisylvian	Unilateral	Bilateral/ asymmetric	Delicate/ coarse	Undulated profile	None	Increased number and dilatation of superficial veins in PMG cortex	Absence of septum pellucidum, bilateral ventricular dilatation	Same as seen at 3T
7	53/F	Normal	Normal	Mild L hemiparesis	9	CPS/ weekly	Focal	Bilateral CT spikes and diffuse SW	Perisylvian	Unilateral	Unilateral	Coarse	Undulated profile	None	Increased number and dilatation of superficial veins in PMG cortex	L hippocampal dysplasia, R TO NH	Same as seen at 3T
8	26/F	Mild impairment	Mild motor delay	Awkwardness, dysarthria, dyspraxia	8	CPS/ remission since age 10 yrs	Focal	Diffuse SW	Perisylvian	Unilateral	Unilateral	Coarse	Undulated profile	None	Increased number and dilatation of superficial veins in PMG cortex	R Sylvian fissure vertically oriented and shortened and, mild thickening in the inferior frontal gyrus and superior T gyrus	Abnormal thickening and folding of the R Sylvian fissure and frontal operculum, R and L anterior NH
9	39/F	Mild cognitive impairment	Mild motor delay, moderate language delay	Dysarthria, dyspraxia, mild R hemiparesis	0.7	SPS/ monthly	Focal	Bilateral PO spikes	Perisylvian	Bilateral/ asymmetric	Bilateral/ asymmetric	Coarse	Not detectable	None	Increased number and dilatation of superficial veins in PMG cortex	R P open-lip SCZ, absent septum pellucidum, bilateral ventricular dilatation	R P open-lip SCZ, absent septum pellucidum, L frontal incomplete cleft, adhesion between ependyma and subarachnoid space in the frontal horn of the L lateral ventricle, bilateral ventricular dilatation
10	28/F	Normal	Mild motor delay	Mild L hemiparesis	17	Focal/ remission since age 17 yrs	Focal	Normal	Perisylvian	Unilateral	Bilateral/ asymmetric	Delicate/ coarse	Undulated profile	None	Increased number and dilatation of superficial veins in PMG cortex	None	None

On-line Table 1: *Clinical details and MRI findings in the PMG cohort.*

3T	Sequence type	TR (ms)	TE (ms)	TI (ms)	Voxel size (mm^3)	FA (°)	RBW (kHz)	FOV (mm)	No. of slices/ partitions	Slice thickness (mm)	Scan time (min)
T1W FSPGR	3D	6.6	2.8	450	1x1x1	13	31.3	256	156	1	04:12
T2 FLAIR	2D	9027	155	2250	0.75x0.75x4	90	50	240	24	4	04:50
T2W FSE	2D	2840	78.8	-	0.75x0.75x4	90	62.5	240	24	4	02:45
White matter suppressed FSE-IR	2D	5000	39.5	350	0.94x0.94x2.5	90	31.2	240x180	30	2.5	05:16
7T	**Sequence type**	**TR (ms)**	**TE (ms)**	**TI (ms)**	**Voxel size (mm^3)**	**FA (°)**	**RBW (kHz)**	**FOV (mm)**	**No. of slices/ partitions**	**Slice thickness (mm)**	**Scan time (min)**
T1W FSPGR	3D	6.3	2.3	450	1x1x1	12	50	224	96	1	05:47
SWAN	3D	54.1	5.6, 12.0, 18.3, 24.7, 31.1, 37.5, 43.9	-	0.5x0.5x1	15	50	224	66	1	09:38
T2*W targeted dual-echo GRE	2D	500	10, 20	-	0.25x0.25x2	30	31.25	112	15	2	07:32
T2W FSE	2D	6000	87	-	0.5x0.5x2	90	20.83	224	10	2	05:00
Gray-White matter TBE FSE-IR	2D	4875	7.9	700	0.5x0.5x2	90	62.5	224	10	2	08:18

FA = flip angle; kHz = kilohertz; min = minute; mm = millimeter; mm^3 = cubic millimeter; ms = millisecond; No. = number; RBW = receiver bandwidth; ° = degree. Note: The final SWAN image is obtained by averaging the images obtained at each echo-times.

On-line Table 2: *Synopsis of the parameters of the 3T and 7T imaging techniques used.*

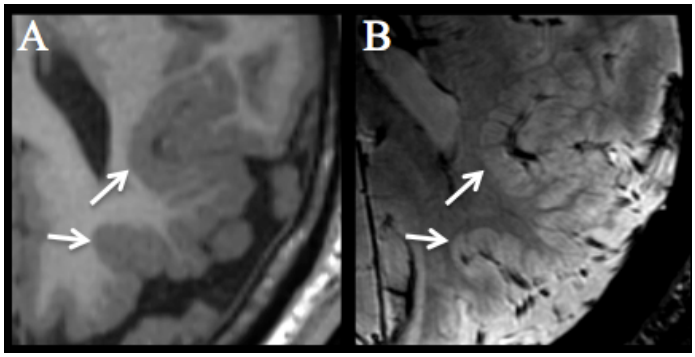

On-line Fig 1. *Patient 2 (A, B). Comparison of 3T axial 3D FSPGR (A) and 7T axial 3D SWAN (B) images. Figure A shows "coarse", thick and bumpy polymicrogyric cortex in the left parietal lobe (arrows). Figure B reveals a pattern with a thinner cortex and higher periodicity of the microgyri, which are tightly packed.*

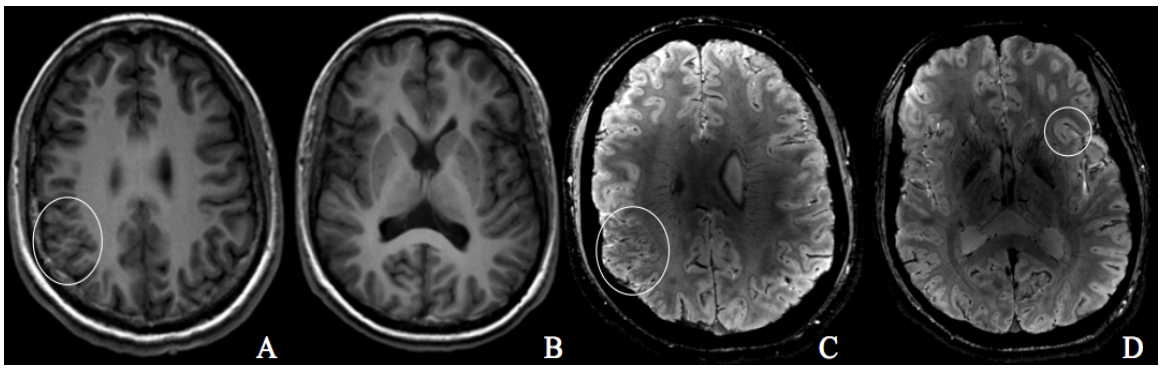

On-line Fig 2*. Patient 6. 3T axial 3D FSPGR (A, B), 7T axial 3D SWAN (C, D) images. A: 3T FSPGR shows unilateral polymicrogyria involving the supramarginal gyrus and the lateral sulcus of right parietal lobe (white circle). B: 3T FSPGR at a lower level does not show any relevant abnormality. C: 7T SWAN confirms with high detail the unilateral polymicrogyria in the supramarginal gyrus and the lateral sulcus of right parietal lobe (white circle) D: 7T SWAN imaging discloses abnormal cortical infolding at the level of the left frontal operculum (white circle) with respect to 3T FSPGR images.*

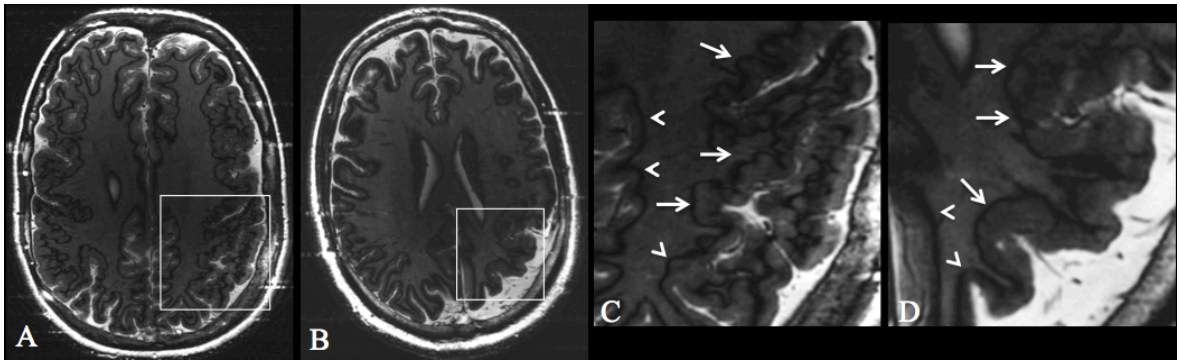

On-line Fig 3. *Patients 1 (A and magnified C) and 2 (B and magnified D). 7T axial 2D TBE FSE-IR. TBE images show a hypointense line along the gray/white matter interface, which provides a better definition of the polymicrogyric border and distinction of the normal (arrowheads) versus polymicrogyric cortex (arrows).*

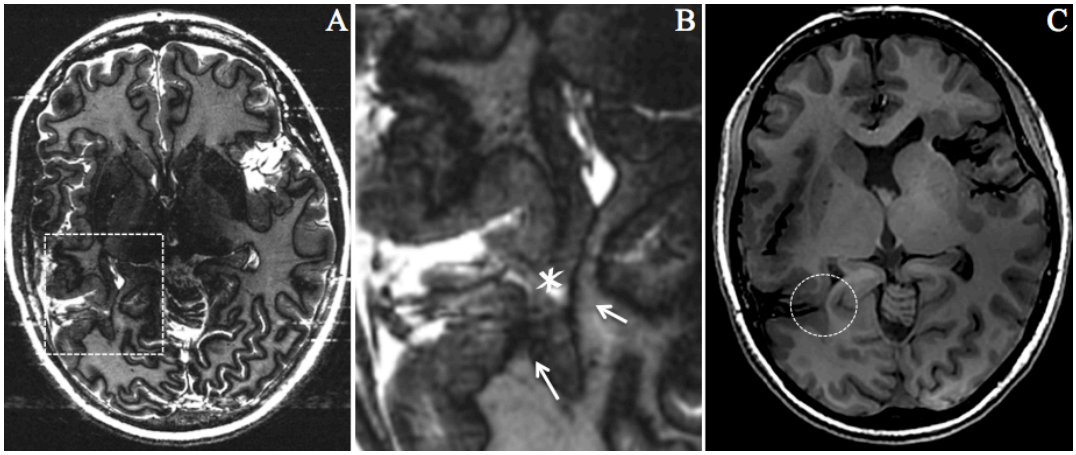

On-line Fig 4. Patient 9. 7T axial 2D FSE-IR TBE (A, magnified in B) and 3D FSPGR (C) images. TBE imaging in A enhances detection of the borders of the polymicrogyric cortex and discloses a cleft, with open lips in its most superficial aspect and closed lips in its deepest aspect, adjacent to the wall of the occipital horn. The magnified image B shows the thickened and irregular gray matter that reaches the ventricle (arrows) and the cleft (asterisk). Image C is a FSPGR image, acquired 1 mm above the TBE image. Image C shows a small open-lip schizencephalic cleft with separated lips (white circle).

Chapter 3.

7T MRI in focal epilepsy with unrevealing conventional field strength imaging

Alessio De Ciantis.[1,2] Carmen Barba,[1] Laura Tassi,[3] Mirco Cosottini,[4,5] Michela Tosetti,[2,5] Mauro Costagli,[2,5] Manuela Bramerio,[6] Emanuele Bartolini,[1,2] Laura Biagi,[2,5] Massimo Cossu,[3] Veronica Pelliccia,[3] Mark R. Symms,[7] and Renzo Guerrini.[1,2]

[1] Pediatric Neurology Unit and Laboratories, Children's Hospital A. Meyer-University of Florence, Florence, Italy. [2] IRCCS Stella Maris Foundation, Pisa, Italy. [3] "C. Munari" Epilepsy Surgery Centre, Niguarda Hospital, Milan, Italy.[4] Department of Translational Research and New Technologies in Medicine and Surgery, University of Pisa, Pisa, Italy. [5] IMAGO7 Foundation, Pisa, Italy.[6] Department of Pathology, Niguarda Hospital, Milan, Italy.[7] General Electric MR Scientist, Imago7, Pisa, Italy.

This chapter has been published in Epilepsia, vol 57, no.3, pp 445-454, 2016.

3.1 Summary

3.1.1 Objective

To assess the diagnostic yield of 7T MRI in detecting and characterizing structural lesions in patients with intractable focal epilepsy and unrevealing conventional (1.5 or 3T) MRI.

3.1.2 Methods

We conducted an observational clinical imaging study on 21 patients (17 adults, 4 children) with intractable focal epilepsy, exhibiting clinical and electroencephalographic features consistent with a single seizure onset zone (SOZ) and unrevealing conventional MR imaging. Patients were enrolled at two tertiary epilepsy surgery centers and imaged at 7T, including whole brain (3D T1W FSPGR, 3D susceptibility-weighted angiography [SWAN], 3D FLAIR) and targeted imaging (2D T2*-weighted dual-echo gradient-recalled echo [GRE] and 2D gray-white matter tissue border enhancement [TBE] FSE-IR). 1.5 or 3T MRIs deemed unrevealing at the referral center were reviewed by three experts in epilepsy imaging. Reviewers were provided information regarding the suspected localization of the SOZ. The same team subsequently reviewed 7T images. Agreement in imaging interpretation was reached through consensus-based discussions based on visual identification of structural abnormalities and their likely correlation with clinical and electrographic data.

3.1.3 Results

7T MRI revealed structural lesions in six out of 21 patients (29%). The diagnostic gain in detection was obtained using GRE and FLAIR images. Four of the six patients with abnormal 7T underwent epilepsy surgery. Histopathology revealed focal cortical dysplasia (FCD) in all. In the remaining 15 patients (71%) 7T MRI remained unrevealing; four of them underwent epilepsy surgery and histopathology revealed gliosis.

3.1.4 Significance:

7T MRI improves detection of epileptogenic FCD that is not visible at conventional field strengths. A dedicated protocol including whole brain FLAIR and GRE images at 7T targeted at the suspected SOZ increases the diagnostic yield.

3.2 Introduction

Magnetic resonance imaging (MRI) is a non-invasive tool to detect structural brain lesions and assess potential candidates for epilepsy surgery.[1] Absence of a structural lesion on MRI still represents a challenge for surgical management as it entails a poorer prognosis in both children and adults.[2-5] Although epileptogenic lesions, mainly focal cortical dysplasia (FCD), have been demonstrated in 30 to 50% of histopathology specimens of MRI negative patients,[6-12] 16 to 43% of patients referred for presurgical assessment have negative brain MRI.[9, 10, 13, 14]

The diagnostic yield of MRI in detecting subtle lesions is influenced by reader expertise and the accuracy with which the suspected epileptogenic zone is indicated, but it is also strongly dependent on technical considerations such as the field strength, use of phased array head coils, dedicated epilepsy MRI protocols and novel quantitative analyses.[6, 15-20]

Although applying a higher magnetic field strength could theoretically increase image resolution, the few studies comparing the diagnostic yield of 3T versus 1.5T imaging in detecting structural lesions in patients with focal epilepsy reached contradictory conclusions concerning the rates of newly detected lesions at 3T (5% to 65%).[15-20] So far, no comparative studies have investigated the diagnostic yield of 7T with respect to conventional MRI.

In the past few years, 7T MRI has been used for in vivo brain imaging, providing several advantages.[21-23] Compared to conventional field strengths (1.5-3T), 7T MRI offers higher signal-to-noise ratio (SNR), which enables higher spatial resolution. As a result, 7T can provide better depiction of anatomical structures and enhance both detection and characterization of brain lesions, increasing diagnostic confidence.[22,23] By revealing small anatomical details, 7T MRI might therefore detect structural lesions not visible at conventional MRI.

We evaluated the diagnostic yield of 7T MRI in 21 patients with intractable focal epilepsy and unrevealing conventional MRI.

3.3 Methods

3.3.1 Patients

We consecutively enrolled, from two centers (Pediatric Neurology Unit, Meyer Hospital in Florence, Italy and "C. Munari" Epilepsy Surgery Center, Niguarda Hospital in Milan, Italy) 21 patients with intractable focal epilepsy in whom clinical and EEG data suggested focal seizure onset zone, and either 1.5T or 3T MRI, or both, had failed to identify an epileptogenic lesion.

We used the following inclusion criteria: 1) age ≥ 8 years; 2) intractable focal epilepsy; 3) unrevealing MRI at conventional field strengths. Exclusion criteria: 1) any contraindications to MRI; 2) the need for sedation during MRI scanning; 3) lack of consent. Patients were imaged at 7T after longer than 48 hours from the last seizure. The experimental protocol was approved by the Italian Ministry of Health and the Pediatric Ethics Committee of the Tuscany Region. The procedures followed were in accordance with institutional guidelines and included an adverse event form. Written informed consent was obtained from all adult patients or from the parents for juvenile subjects.

3.3.2 Scalp and invasive video-EEG recordings

Twenty patients underwent prolonged video-EEG monitoring (> 24h) with scalp electrodes placed according to the International 10-20 System. One patient underwent one hour video-EEG recording while awake and asleep. Five out of the 21 patients were studied with invasive recordings (Stereo electroencephalography, SEEG) to better localize the seizure onset zone (SOZ) for the purpose of epilepsy surgery.

3.3.3 MRI Acquisition

The 1.5 MR (Philips ACS-NT & Achieva) imaging standard protocol included the following sequences: 3D T1-weighted fast field echo (FFE), 2D T2 fluid-attenuated inversion recovery (FLAIR), 2D T2-weighted turbo-spin-echo (TSE), and 2D T1 weighted inversion recovery (IR).

The 3T MR (GE Medical System SignaHDx) imaging standard protocol included the following sequences: 3D T1-weighted fast-spoiled gradient echo (FSPGR), 2D T2 fluid-attenuated inversion recovery (FLAIR), 2D T2-weighted fast spin echo (FSE), and 2D white matter–suppressed FSE inversion recovery (IR).

7T MRI was performed on a Discovery MR 950 MR scanner (GE Healthcare) equipped with a 2-channel transmit/32-channel receive head coil (Nova Medical, Wilmington, Massachusetts). All participants received earplugs and a pair of pads covering the ears to limit acoustic noise. We used a dedicated epilepsy research MRI protocol including the following sequences: 3D T1-weighted FSPGR, 3D susceptibility-weighted angiography (SWAN), 2D T2*-weighted targeted dual-echo gradient-recalled echo (GRE), 2D T2-weighted FSE, 2D gray-white matter tissue border enhancement (TBE) FSE-IR.[24] GRE and TBE sequences were targeted based on the localization of the SOZ. Since July 2014, 3D MP-FLAIR sequence[25] was included in the protocol. No contrast medium was injected. 1.5 T, 3T and 7T sequence parameters are reported in Table 1.

1.5T	Sequence type	TR (ms)	TE (ms)	TI (ms)	Voxel size (mm^3)	FA (°)	RBW (kHz)	FOV (mm)	No. of slices/ partitions	Slice thickness (mm)
T1W FFE	3D	7.2	3.2	-	0.9x1.1x3	8	67.5	256	178	0.9
T2W TSE	2D	3214	100	-	0.9x0.75x3	90	36.1	230	32	3
T2W FLAIR	2D	11000	140	2800	1x0.85x3	90	54.4	252	35	3
T1W IR	2D	2352	15	400	0.9x0.73x3	90	38.1	230	32	3
3T	**Sequence type**	**TR (ms)**	**TE (ms)**	**TI (ms)**	**Voxel size (mm^3)**	**FA (°)**	**RBW (kHz)**	**FOV (mm)**	**No. of slices/ partitions**	**Slice thickness (mm)**
T1W FSPGR	3D	6.6	2.8	450	1x1x1	13	31.3	256	156	1
T2 FLAIR	2D	9027	155	2250	0.75x0.75x4	90	50	240	24	4
T2W FSE	2D	2840	78.8	-	0.75x0.75x4	90	62.5	240	24	4
White matter suppressed FSE-IR	2D	5000	39.5	350	0.94x0.94x2.5	90	31.2	240	30	2.5
7T	**Sequence type**	**TR (ms)**	**TE (ms)**	**TI (ms)**	**Voxel size (mm^3)**	**FA (°)**	**RBW (kHz)**	**FOV (mm)**	**No. of slices/ partitions**	**Slice thickness (mm)**
T1W FSPGR	3D	6.3	2.3	450	1x1x1	12	50	224	96	1
SWAN	3D	54.1	5.6, 12.0, 18.3, 24.7, 31.1, 37.5, 43.9	-	0.5x0.5x1	15	50	224	66	1
T2*W targeted dual-echo GRE	2D	500	10, 20	-	0.25x0.25x2	30	31.25	112	15	2
Gray-White matter TBE FSE-IR	2D	4875	7.9	700	0.5x0.5x2	90	62.5	224	10	2
T2 FLAIR	3D	8000	121	2051	0.x0.7x0.7	90	62.5	202	226	0.7

FA = flip angle; kHz = kilohertz; mm = millimeter; mm^3 = cubic millimeter; ms = millisecond; No. = number; RBW = receiver bandwidth; ° = degree. Note: The final SWAN image is obtained by averaging the images obtained at each echo-times.

Table 1. *1.5T, 3T and 7T sequence parameters.*

3.3.4 MRI Evaluation

To confirm inclusion criteria, 1.5 or 3T deemed unrevealing at the referral center were reviewed on a dedicated workstation (Advantage 4.1; GE Healthcare) by three experts with long-standing experience in epilepsy imaging. The same team subsequently reviewed 7T images using the same workstation. Reviewers were provided information regarding the suspected localization of the SOZ, as determined based on clinical and EEG findings. Agreements in imaging interpretation were reached through consensus-based discussions based on visual identification of structural abnormality and of its likely correlation with clinical and electrographic data.

3.3.5 Surgery and Post-operative outcome

All resections were performed based on the location of the SOZ as defined through epilepsy surgery conferences. All patients were re-examined at fixed intervals for follow-up. Surgical outcome was determined according to Engel's classification.[26]

3.3.6 Histopathology

Histopathological specimens were reviewed by a neuropathologist. Focal cortical dysplasia was classified according to the International League Against Epilepsy (ILAE) criteria.[27]

3.4 Results

3.4.1 Patients

Of the 21 patients included in the study, there were 12 males (57%) and nine females (43%), mean age at the time of the 7T MRI scan was 24.19 ± 8.66 years (range 9-42 years). Twenty patients exhibited drug-resistant seizures at the time of the study while one remaining patient (19) was seizure-free on polytherapy after a long period of intractability. Clinical details for the entire cohort are summarized in Table 2.

No.	Age (yr)/Sex	Scalp EEG		SEEG	Surgery	Histopathology	Seizure outcome	MRI findings		
		Interictal	Ictal	SOZ				1.5T	3T	7T
1	20/M	L TPO SW and low amplitude high frequency discharges	L TPO	L posterior T area	Y	Gliosis	Class Ia	Negative	Not performed	Negative
2	21/M	L FC and vertex SW	L FCP	L insulo-opercular area	Y	FCD type IIA	Class III	Negative	Not performed	Abnormal infolding and thickening of the L insula and central operculum
3	40/F	R posterior T slow waves	NA	R fronto-basal	Y	Gliosis	Class III	Negative	Not performed	Negative
4	34/M	Bilateral FT slow waves (L predominance), L T SW	L T	Not performed	Y	Gliosis + PNH	Short follow-up	Negative	Negative	Negative
5	25/F	L T spikes	L T	Not performed	Y	Gliosis	Class Ib	Negative	Negative	Negative
6	42/M	L FC SW	L anterior F	L superior and middle F gyri, L F opercular area	Y	FCD type IIA	Class Ia	Dubious abnormal L anterior F gyration	Not performed	Abnormal L F gyration with adjacent white matter hyperintensity
7	27/F	R anterior F SW	R anterior F	Not performed	Y	FCD type IIB	Short follow-up	Negative	Negative	R F cortical thickening with cortical dyslamination and underlying transmantle sign
8	13/M	R FT SW	R FT	Not performed	Y	FCD type IIIA	Short follow-up	Negative	Negative	R T pole and insular hyperintensity
9	32/M	L posterior T SW	L TO	Not performed	N	NA	NA	Negative	Not performed	Negative
10	14/F	L FT sharp waves	L T	Not performed	N	NA	NA	Negative	Not performed	Negative
11	24/M	R FT SW	NA	Not performed	N	NA	NA	Negative	Negative	Negative
12	21/F	L anterior T spike and sharp waves	NA	Not performed	N	NA	NA	Not performed	Negative	Negative
13	26/M	Bilateral F (L predominance) SW	Bilateral F (L predominance)	Not performed	N	NA	NA	Negative	Negative	Negative
14	28/F	L FT spikes and polyspikes	L hemispheric with FT predominance	Not performed	N	NA	NA	Not performed	Negative	Negative
15	19/M	L T spikes and polyspikes	L hemispheric with FT predominance	Multifocal (independent L T, L premotor and opercular ictal activity)	N	NA	NA	Negative	Negative	Negative
16	18/F	R FC spikes and polyspike-waves	R FC	Not performed	N	NA	NA	Not performed	Negative	Negative

Continued.

17	31/F	R posterior T sharp waves	R T	Not performed	N	NA	NA	Not performed	Negative	Negative	
18	9/M	L CT spikes	NA	Not performed	N	NA	NA	Not performed	Negative	Negative	
19	13/M	Normal at the time of the study, previously multifocal spikes with L FT predominance	L FT	Not performed	N	NA		Negative	Negative	Negative	
20	23/M	R F	NA	Not performed	N	NA	NA	R F venous dysplasia	Not performed	Subcortical hyperintensity in the R inferior F gyrus associated with venous dysplasia	
21	28/F	L TP sharp waves and spikes	L TP	Not performed	N	NA	NA	Negative	Negative	L P cortical thinning with hypointense subcortical lamina	

Abbreviations: C = central; F = frontal; FCD = focal cortical dysplasia; L = left; NA = not available; No. = number; O = occipital; P = parietal; PNH = periventricular nodular heterotopia; R = right; SEEG = stereo electroencephalography; SOZ = seizure onset zone; SW = spike waves; T = temporal.

Table 2. *Clinical data and study findings in 21 patients with focal epilepsy and unrevealing conventional MRI.*

3.4.2 Video-EEG and Stereo-EEG recordings

Scalp EEG and SEEG features are summarized in Table 2. Seizures were recorded in 16 patients (1, 2, 4-10, 13-17, 19, and 21) using prolonged scalp Video-EEG recordings and in five patients (1-3, 6 and 15) during SEEG. Based on electroclinical findings, the SOZ was localized in the right hemisphere in seven patients, in the left hemisphere in 14 patients. Of the 21 patients, five had frontal lobe epilepsy, six had temporal lobe epilepsy, ten had seizure onset from a multilobar SOZ (4 fronto-temporal, 1 fronto-central, 1 centro-temporal, 1 temporo-parietal, 1 insulo-opercular, 1 temporo-occipital, 1 temporo-opercular).

3.4.3 7T MRI

No adverse events occurred during the 7T MRI scans, whose duration was on average one hour. None of the patients reported any discomfort or side effects during or after the procedure. There were no severe adverse events requiring the premature interruption of the imaging session. 7T MRI features of all patients are summarized in Table 2.

In nine patients (4, 7, 9, 10, 16, 18-21) the complete MRI protocol was acquired. In the remaining 12 patients the protocol was incomplete as FLAIR (1-3, 5, 6, 11-15) or TBE (3, 6, 8, 11, 13-15, 17) or GRE (8) could not be applied, as they had not yet been implemented at the time of the scan.

In six patients (29%) (2, 6-8, 20 and 21) 7T detected a structural abnormality that had not been previously revealed by conventional MRI. In all, the newly detected abnormality was concordant with the hypothesized SOZ (Table 2). In brief, in one patient each we identified structural abnormalities consistent with left insulo-temporo-opercular dysplasia (patient 2) (Figure 1), left frontal dysplasia (patient 6) (Figure 2), right frontal dysplasia (patient 7) (Figure 3), right temporal and insular dysplasia (patient 8), right frontal dysplasia associated with vascular dysplasia (patient 20). One additional patient (patient 21) had a left parietal area of cortical thinning with a hypointense subcortical lamina (Figure 4).

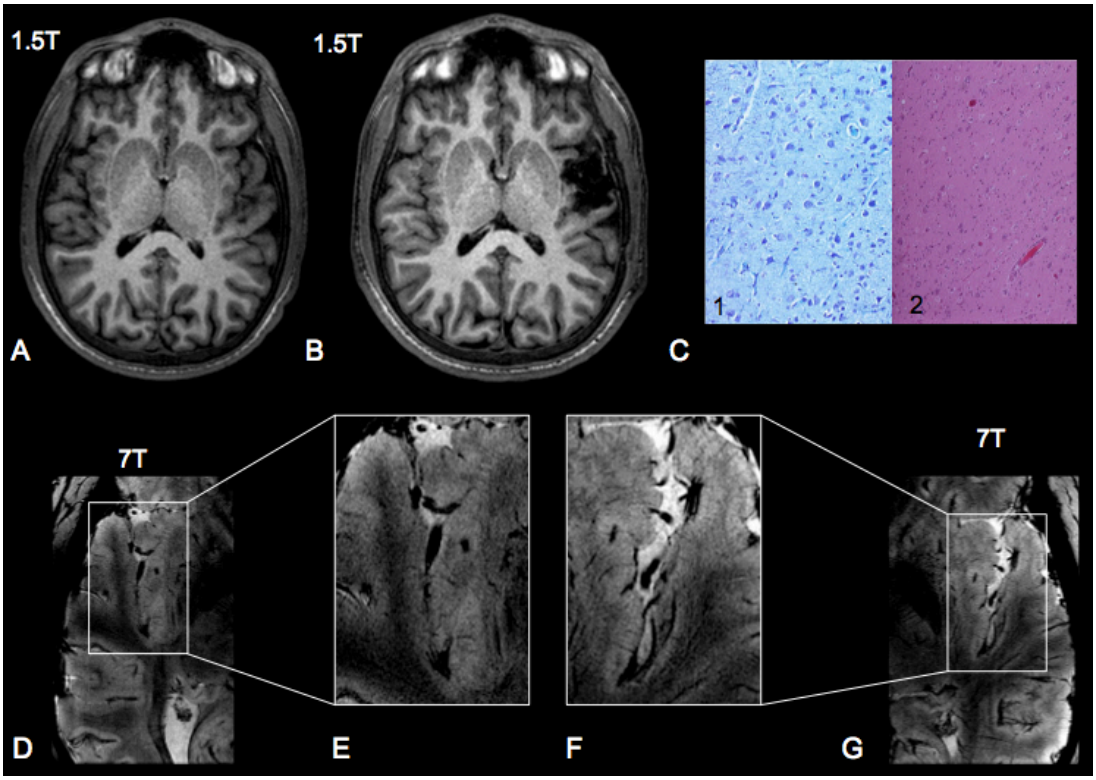

Figure 1. *1.5T and 7T MRI images in a patient with intractable focal epilepsy (Patient 2). Pre-operative (A) and post-operative (B) 1.5T axial 3D SPGR; histopathology (C); 7T axial 2D GRE, right hemisphere (D) magnified in E; 7T axial 2D GRE, left hemisphere (G) magnified in F. A, D and E reveal no structural abnormalities. B is a post-operative MRI showing the extent of resection. C: histological section (C1: Kluver 200X; C2: Ematoxylin and Eosin 100X) demonstrating cortical laminar disruption and dysmorphic neurons, consistent with FCD IIA. Of note, Figure D, and its magnified image E show normal distinction between white and grey matter in the right superior temporal gyrus and the insula. Conversely, Figure G, and its magnified image F show blurring of the grey-white matter junction in the anterior part of the left superior temporal gyrus and in the insular gyri.*

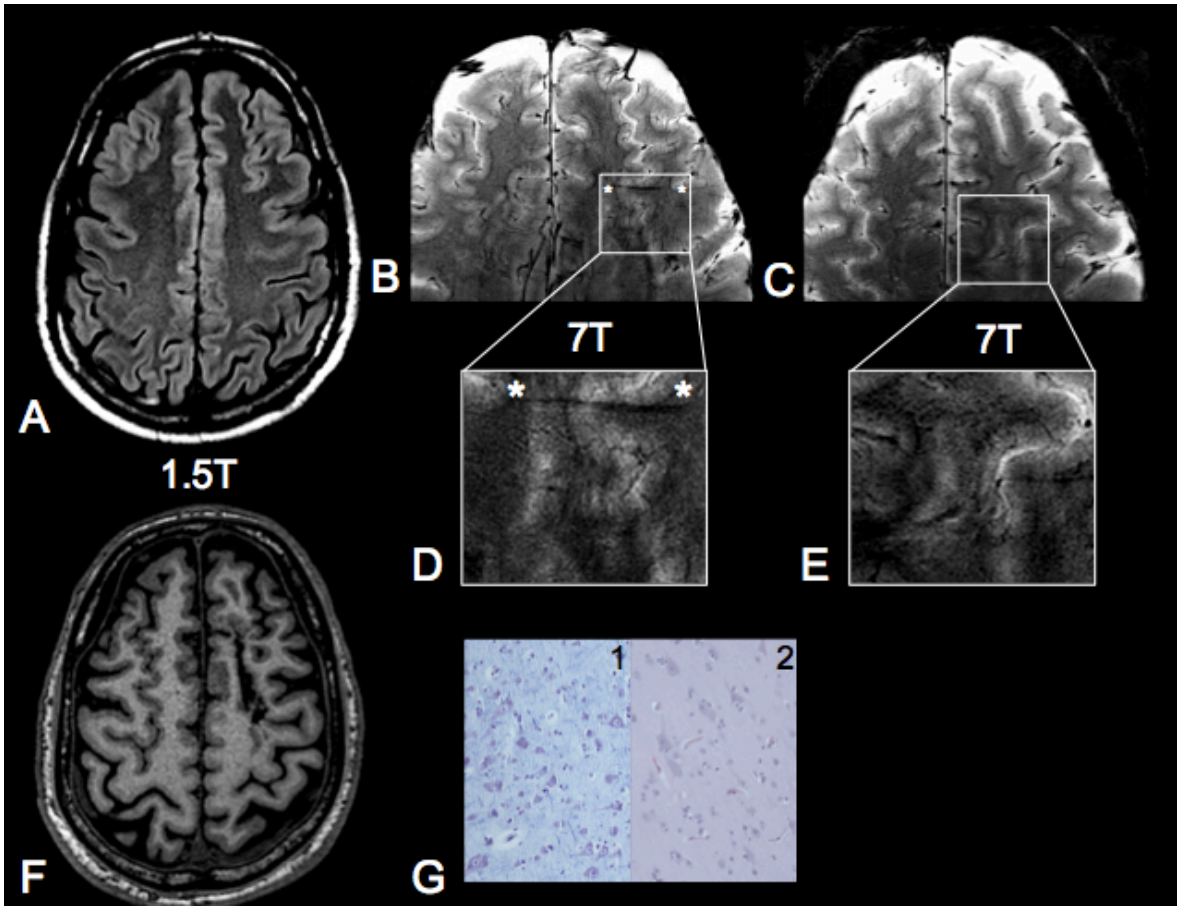

Figure 2. *Pre-operative 1.5T and 7T images, post-operative 1.5T and histopathology in a patient with FCD IIA. (Patient 6). 1.5T axial 3D FLAIR (A), 7T axial 2D GRE (B, C) and magnified images (D, E), post-operative 1.5T axial 3D SPGR (F) and histopathology (G). No relevant structural abnormality is visible in 'A'. Figure B and its expanded view (D) reveal an area of increased white matter signal in the left frontal lobe at the cortical subcortical junction, close to the linear low intensity strip (spanning between the two asterisks) caused by the stereo-EEG depth electrode. Figure C and magnification (E) substantiate the presence of a subcortical high signal intensity zone with blurring of the grey-white matter junction. Figure F is a post-operative MRI showing the extent of resection. Figure G shows a histological brain tissue section (G1: Kluver 200X; G2: Ematoxylin and eosin 400X) with cortical laminar disruption and dysmorphic neurons, without balloon cells, consistent with FCD IIA.*

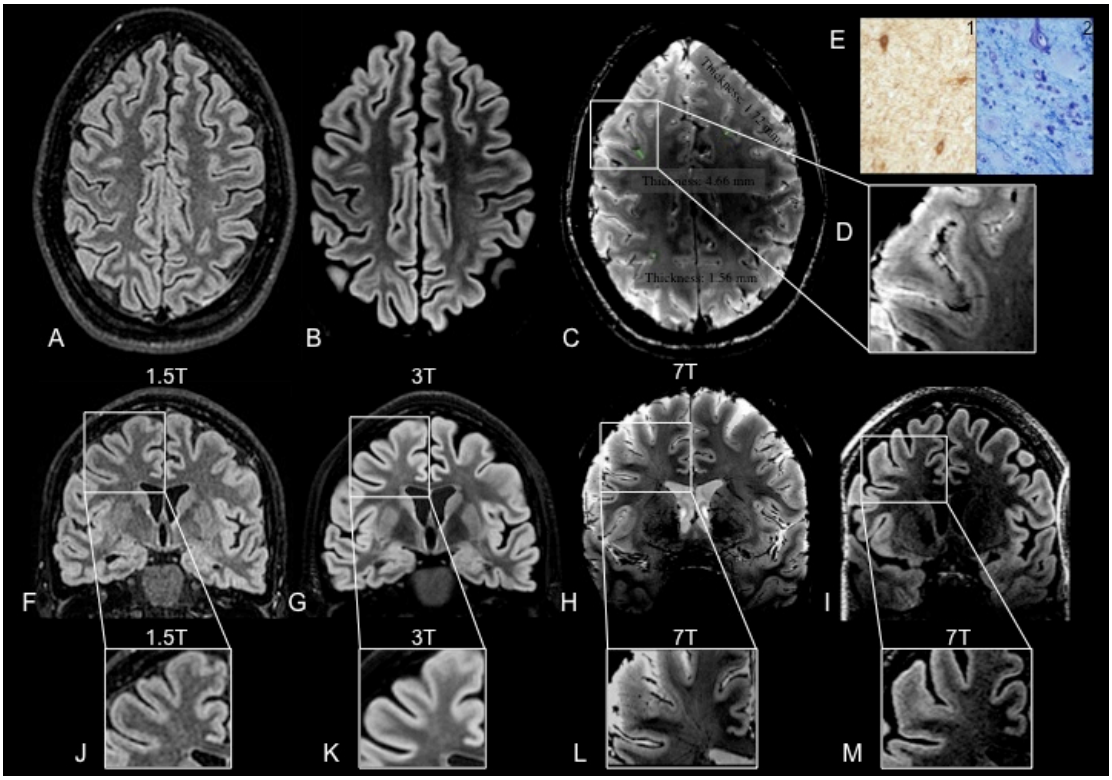

Figure 3. *Pre-operative 1.5T, 3T and 7T images, and histopathology in a patient with FCD IIB. (Patient 7). 1.5T axial 3D FLAIR (A), 3T axial 3D FLAIR (B), 7T axial 3D SWAN (C, magnified in D), histopathology (E), 1.5T coronal 3D FLAIR (F, magnified in J), 3T coronal 3D FLAIR (G, magnified in K), 7T coronal 2D GRE (H, magnified in L) and 7T coronal 3D FLAIR (I, magnified in M). Figures A and B reveal no structural abnormalities. Figures F, G, and their magnified images J and K, reveal a subtle transmantle sign, whose appreciation is facilitated, with hindsight, after the more convincing 7T imaging revealed additional morphological markers of FCD, such as cortical thickening, a hypointense intracortical layer, blurring of the grey-white matter junction and tapering to the ventricle (see Figures H and I). Figure C and magnification D show with high definition thickening of a right frontal sulcus, associated with a hypointense intracortical layer and derangement of cortical structure. Figure E shows a histological brain tissue section (D1: Bielchowsky 200X; D2: Kluver 400X) demonstrating cortical laminar disruption, dysmorphic neurons and abundant balloon cells, consistent with FCD IIB. Figure H and magnification L provide ultra-high resolution details of the dysplastic cortex, revealing abnormal thickening, the hypointense intracortical layer, blurring of the grey-white matter junction and tapering to the ventricle. Figure I and magnification M, albeit with less cortical details, corroborate the findings provided by GRE images and provide an enhanced detection of both blurred grey-white matter junction and a slight depth of the sulcus hyperintensity with transmantle sign.*

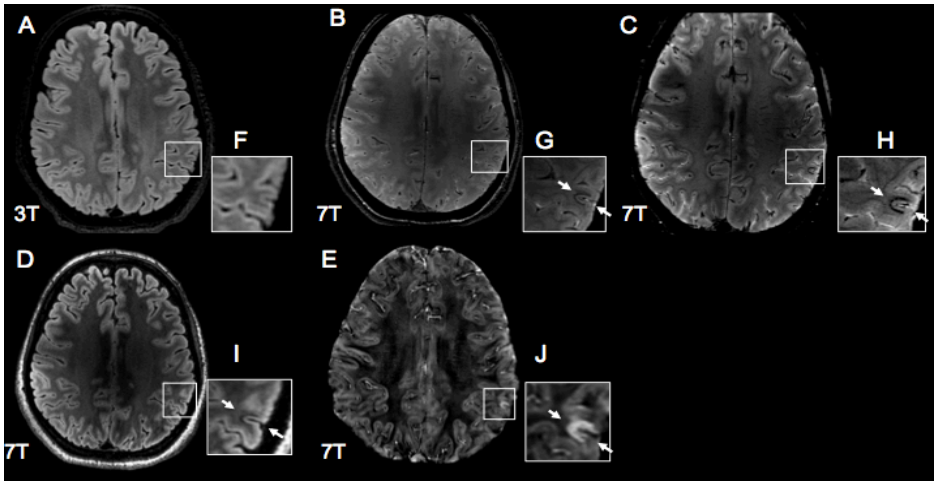

Figure 4. *3T and 7T images, with 7T magnetic susceptibility map in a patient with intractable focal epilepsy. (Patient 21). The top row shows 3T axial 3D FLAIR (A), 7T axial 3D SWAN (B), 2D GRE (C), 3D FLAIR (D) images and 7T magnetic susceptibility map (E). The bottom row shows zoomed images of the boxed regions. Figure A and magnified image (F) reveal no structural abnormalities. Figure B-D discloses cortical thinning associated with a hypointense subcortical lamina in the left parietal lobe, characterized by along the grey-white matter interface (white arrows). Figures G-I, which are the magnifications of the boxed regions, enhance the detection of the epileptogenic lesion showing with high detail the reduced cortical thickness and hypointense line underlying the cortex (arrows). Of note, the lower resolution and contrast obtained enlarging 3T FLAIR image (F) compared to 7T zoomed images (G-I). Figure E and the magnified image J, show the magnetic susceptibility map in which a strong high signal intensity line (arrows) in the area concordant with the hypothesized SOZ, indicating different levels of paramagnetic substances with respect to the normal cortex.*

The added value of 7T in detecting structural lesions was achieved using GRE (patients 2 and 6), FLAIR (patient 8), or both (patients 7, 20 and 21). Due to the high spatial resolution and the increased sensitivity to magnetic susceptibility, GRE images allowed a better evaluation of the different components within the cortex, which were otherwise uniform in the other sequences. However, GRE sequences uncovered structural lesions in two patients (2 and 6) in whom FLAIR was not performed. In one patient (8), FLAIR detected right temporal and insular signal changes not otherwise identifiable with GRE.

We did not come across incidental (and potentially false positive) structural findings unrelated to the SOZ. In this study, 7T MRI was tailored to the suspected SOZ and, in both participating epilepsy surgery Centers, integrated in a multimodal presurgical evaluation protocol including advanced neurophysiological and neuroimaging techniques. This

approach reduces the chances of false positive findings and the influence they might have on surgical planning.

3.4.4 Surgery and Post-operative outcome

Eight out of 21 patients (38%) underwent epilepsy surgery (Table 2). The surgical intervention consisted of cortectomy in six patients (2 left temporal, 1 left insulo-opercular, 1 right frontal, 2 left frontal) and temporal lobectomy in two (1 left, 1 right). At last follow up, two patients (1 and 6) were seizure-free (Engel class Ia); one patient (5) experienced simple partial seizures only (class Ib) and two patients (2 and 3) had worthwhile improvement (class III). Three patients (4, 7 and 8) were seizure free post-surgery but their follow-up was too short (< 1 year) at the time of writing to classify outcome.

3.4.5 Histopathology

Histopathology revealed FCD type IIA in two patients (2 and 6), FCD IIB in one (7), FCD IIIA in one (8) and gliosis in four (1, 3-5).

3.5 Discussion

In this study, 7T MRI revealed structural abnormalities not previously detected using conventional MRI in six out of 21 patients (29%) with focal epilepsy. Previous studies had compared the diagnostic yield of 3T vs 1.5T MRI in patients with focal epilepsy, reporting rates of improved lesion detection of 3T scanners ranging from 5% to 65%.[15-20] These highly variable rates were likely influenced by multiple factors, including differences in field strength,[15-20] coils used,[15, 17-19] expertise between reviewers,[15-18, 20] use of a dedicated epilepsy protocol[15-17] and clinical characteristics of patients.[15-17, 19] Although an accurate comparison remains difficult, there seems to be no doubt that in a non-negligible percentage of patients 3T provides additional information compared to lower field strengths.

The added diagnostic value of 7T, compared to lower field strengths, has been demonstrated for polymicrogyria,[28] vascular malformations,[29] hippocampal sclerosis,[30] brain tumors,[31] stroke,[32] multiple sclerosis[33] and degenerative brain diseases.[34] However, no studies using a field strength of 7T have addressed its diagnostic yield in focal epilepsy of presumed lesional origin. The 29% detection rate of epileptogenic lesions we found comparing 7T to conventional MRI could in the first instance be attributed to inherent advances related to 7T imaging. 7T offers higher SNR, enabling higher spatial resolution with better depiction of anatomical structures.[21-23]

An additional factor contributing to the diagnostic gain of 7T MRI might derive from the use of a dedicated protocol, in particular the GRE and FLAIR images. Due to the high spatial resolution and sensitivity to the magnetic susceptibility properties of tissues, GRE imaging allows better evaluation of the different components within the cortex, which are otherwise uniform using other sequences. Conversely, FLAIR imaging, which emphasizes signal changes of the cortex and along the cortical-white matter interface, uncovered even slight signal hyperintensities not otherwise visible using GRE.

All patients included in this study had severe chronic epilepsy and had been extensively investigated in two tertiary epilepsy surgery centers for precisely defining the SOZ. Such a thorough selection makes the cohort under study not representative of the larger population of individuals with focal epilepsy who are seen in non-epilepsy surgery centers and could have determined an increased pre-test probability to detect an epileptogenic lesion.

Although unblinded interpretation of MRI scans with respect to clinical and EEG data improves the diagnostic yield of MRI in epilepsy,[15,20,38] this factor is unlikely to have contributed to the increase in diagnostic yield at 7T as also images performed at conventional field were interpreted unblinded to the suspected SOZ.

Identifying a structural lesion on MRI is crucial in patients with drug-resistant focal epilepsy as its concordance with electrophysiological data facilitates presurgical decision-making and carries a better surgical outcome.[4, 5, 35, 36] The rate of seizure freedom after epilepsy surgery falls from 71% when an MRI visible lesion is present to around 40% when MRI is negative.[5, 10, 37-40] Depiction of potentially epileptogenic lesions provides target areas for subsequent intracerebral electrode implantation or obviates the need for intracranial monitoring, facilitating surgery without further invasive procedures. While in some of the patients in whom 7T MRI detected, or better characterized, structural lesions

we could adopt more focused and less invasive approach, due to the preliminary nature of the study in none of the patients did we switch from the originally planned procedure to a minimally invasive approach.

A structural lesion is found at histopathology in 30-50% of patients with unrevealing conventional MRI who undergo epilepsy surgery.[6] Focal cortical dysplasia and, less often, gliosis are the most common findings.[6-12] Four out of the six 7T MRI positive patients in this study underwent epilepsy surgery. In all of them, the epileptogenic lesions supposed to be FCD at 7T were histologically confirmed. In the four out of 15 patients with unrevealing 7T MRI who underwent surgery (27%), histopathology revealed gliosis. However, associated mild cortical dysplasia might have escaped both 7T and histopathology detection.

Our study has some limitations. The number of patients studied was relatively low, which prevented us from statistical validation of the diagnostic yield of 7T versus conventional imaging. While GRE sequences were implemented earlier and could be applied to a larger number of patients (20/21), FLAIR sequences were only developed in the course of the study and applied to a limited number of patients (11/21). The incomplete protocol might have affected the diagnostic yield of 7T MRI in some patients, overall reducing its detection rate. The previous use of MRI scans of different field strength resulted in variations of protocols and acquisition methods between conventional MRI and 7T. In addition, two patients in whom 7T MRI revealed FCD did not undergo 3T MR, which might have detected the lesion.

In spite of these limitations, our findings suggest that re-imaging at 7T patients with focal epilepsy and unrevealing conventional MRI offers considerable chances of identifying an underlying FCD and improving presurgical work-up and surgical planning.

We confirm that we have read the Journal's position on issues involved in ethical publication and affirm that this report is consistent with those guidelines.

3.6 Acknowledgment

This research was supported by the European Union Seventh Framework Programme FP7/2007–2013 under the project 'DESIRE' (grant agreement 602531) to R.G. and the Pisa Foundation (Project 133/11) 'Ultra-high field MRI targeted imaging of dysplastic

cortical lesions and dysembryoplastic tumours' to R.G. The authors thank the patients and their families for participating in the research and Dr Manojkumar Saranathan, Dept. of Medical Imaging, University of Arizona, for his help in implementing the MP-FLAIR sequence.

3.7 References

1. Daghistani R, Widjaja E. Role of MRI in patient selection for surgical treatment of intractable epilepsy in infancy. Brain Dev 2013;35:697-705.

2. Berkovic SF, McIntosh AM, Kalnins RM, et al. Preoperative MRI predicts outcome of temporal lobectomy: an actuarial analysis. Neurology 1995;45:1358-1363.

3. Zentner J, Hufnagel A, Ostertun B, et al. Surgical treatment of extratemporal epilepsy: clinical, radiologic, and histopathologic findings in 60 patients. Epilepsia 1996;37:1072-1080.

4. Mosewich RK, So EL, O'Brien TJ, et al. Factors predictive of the outcome of frontal lobe epilepsy surgery. Epilepsia 2000;41:843-849.

5. Téllez-Zenteno JF, Hernandez Ronquillo L, Moien-Afshari F, et al. Surgical outcomes in lesional and non-lesional epilepsy: a systematic review and meta-analysis. Epilepsy Res 2010;89:310-318.

6. Bernasconi A, Bernasconi N, Bernhardt BC, et al. Advances in MRI for 'cryptogenic' epilepsies. Nat Rev Neurol 2011;7:99-108.

7. Alarcón G, Valentin A, Watt C, et al. Is it worth pursuing surgery for epilepsy in patients with normal neuroimaging? J Neurol Neurosurg Psychiatry 2006;77:474-480.

8. Chapman K, Wyllie E, Najm I, et al. Seizure outcome after epilepsy surgery in patients with normal preoperative MRI. J Neurol Neurosurg Psychiatry 2005;76:710-713.

9. McGonigal A, Bartolomei F, Regis J, et al. Stereoelectroencephalography in presurgical assessment of MRI-negative epilepsy. Brain 2007;130:3169-3183.

10. Bien CG, Szinay M, Wagner J, Clusmann H, et al. Characteristics and surgical outcomes of patients with refractory magnetic resonance imaging-negative epilepsies. Arch Neurol 2009;66:1491-1499.

11. Seo JH, Noh BH, Lee JS, et al. Outcome of surgical treatment in non-lesional intractable childhood epilepsy. Seizure 2009;18(9):625-629.

12. Wang ZI, Alexopoulos AV, Jones SE, J, et al. The pathology of magnetic-resonance-imaging-negative epilepsy. Mod Pathol 2013;26:1051-1058.

13. Duncan JS. Imaging in the surgical treatment of epilepsy. Nat Rev Neurol 2010;6:537-550.

14. Berg AT, Vickrey BG, Langfitt JT, et al. The multicenter study of epilepsy surgery: recruitment and selection for surgery. Epilepsia 2003;44:1425-1433.

15. Winston GP, Micallef C, Kendell BE, et al. The value of repeat neuroimaging for epilepsy at a tertiary referral centre: 16 years of experience. *Epilepsy Res* 2013;105:349-355.

16. Nguyen DK, Rochette E, Leroux JM, et al. Value of 3.0 T MR imaging in refractory partial epilepsy and negative 1.5 T MRI. Seizure 2010;19:475-478.

17. Zijlmans M, de Kort GA, Witkamp TD, et al. 3T versus 1.5T phased-array MRI in the presurgical work-up of patients with partial epilepsy of uncertain focus. J Magn Reson Imaging 2009;30:256-262.

18. Phal PM, Usmanov A, Nesbit GM, et al. Qualitative comparison of 3-T and 1.5-T MRI in the evaluation of epilepsy. AJR Am J Roentgenol 2008;191:890-895.

19. Strandberg M, Larsson EM, Backman S, et al. Pre-surgical epilepsy evaluation using 3T MRI. Do surface coils provide additional information? Epileptic Disord 2008;10:83-92.

20. Knake S, Triantafyllou C, Wald LL, et al. 3T phased array MRI improves the presurgical evaluation in focal epilepsies: a prospective study. Neurology 2005;65:1026-1031.

21. Umutlu L, Ladd ME, Forsting M, et al. 7 Tesla MR imaging: opportunities and challenges. RoFo 2014;186:121-129.

22. van der Kolk AG, Hendrikse J, Zwanenburg JJ, et al. Clinical applications of 7 T MRI in the brain. Eur J Radiol 2013;82:708-718.

23. Balchandani P, Naidich TP. Ultra-High-Field MR Neuroimaging. AJNR Am J Neuroradiol 2014;36:1204-1215.

24. Costagli M, Kelley DA, Symms MR, et al. Tissue Border Enhancement by inversion recovery MRI at 7.0 Tesla. Neuroradiology 2014;56:517-523.

25. Saranathan M, Tourdias T, Kerr AB, et al. Optimization of magnetization-prepared 3-dimensional fluid attenuated inversion recovery imaging for lesion detection at 7 T. Invest Radiol 2014;49:290-298.

26. Engel J Jr, Van Ness PC, Rasmussen TB, Ojemann LM. Outcome with respect to epileptic seizures, 2nd ed. New York, NY: Raven Press; 1993.

27. Blümcke I, Thom M, Aronica E, et al. The clinicopathologic spectrum of focal cortical dysplasias: a consensus classification proposed by an ad hoc Task Force of the ILAE Diagnostic Methods Commission. Epilepsia 2011;52:158-174.

28. De Ciantis A, Barkovich AJ, Cosottini M, et al. Ultra-high-field MR imaging in polymicrogyria and epilepsy. AJNR Am J Neuroradiol 2015;36:309-316.

29. Schlamann M, Maderwald S, Becker W, et al. Cerebral cavernous hemangiomas at 7 Tesla: initial experience. Acad Radiol 2010;17:3-6.

30. Henry TR, Chupin M, Lehericy S, et al. Hippocampal sclerosis in temporal lobe epilepsy: findings at 7 T. Radiology 2011;261:199-209.

31. Lupo JM, Li Y, Hess CP, et al. Advances in ultra-high field MRI for the clinical management of patients with brain tumors. Curr Opin Neurol 2011;24:605-615.

32. Madai VI, von Samson-Himmelstjerna FC, Bauer M, et al. Ultrahigh-field MRI in human ischemic stroke--a 7 Tesla study. PloS One 2012;7:e37631.

33. Tallantyre EC, Dixon JE, Donaldson I, et al. Ultra-high-field imaging distinguishes MS lesions from asymptomatic white matter lesions. Neurology 2011;76:534-539.

34. Cosottini M, Frosini D, Pesaresi I, et al. MR imaging of the substantia nigra at 7 T enables diagnosis of Parkinson disease. Radiology 2014;271:831-838.

35. Kuzniecky R, Burgard S, Faught E, et al. Predictive value of magnetic resonance imaging in temporal lobe epilepsy surgery. Arch Neurol 1993;50:65-69.

36. Spencer S, Huh L. Outcomes of epilepsy surgery in adults and children. Lancet Neurol 2008;7:525-537.

37. Immonen A, Jutila L, Muraja-Murro A, et al. Long-term epilepsy surgery outcomes in patients with MRI-negative temporal lobe epilepsy. Epilepsia 2010;51:2260-2269.

38. Von Oertzen J, Urbach H, Jungbluth et al. Standard magnetic resonance imaging is inadequate for patients with refractory focal epilepsy. J Neurol Neurosurg Psychiatry. 2002;73:643-647.

39. Bast T. Outcome after epilepsy surgery in children with MRI-negative non-idiopathic focal epilepsies. Epileptic Disord 2013;15:105-113.

40. Jayakar P, Dunoyer C, Dean P, et al. Epilepsy surgery in patients with normal or nonfocal MRI scans: integrative strategies offer long-term seizure relief. Epilepsia 2008;49:758-764.

Chapter 4.

SAR Prediction in Adults and Children by Combining Measured B1+ Maps and Simulations at 7.0T

Gianluigi Tiberi, PhD[1,2,*], Mauro Costagli, PhD[1,2], Laura Biagi, PhD[2], Alessio De Ciantis, MD[3], Nunzia Fontana, PhD[4,5], Riccardo Stara, PhD[5], Mark Roger Symms, PhD[6], Mirco Cosottini, MD[7], Renzo Guerrini, MD[3], Michela Tosetti, PhD[2,1]

[1] Imago7 Foundation, Pisa, Italy. [2] Laboratory of Medical Physics and Biotechnologies for Magnetic Resonance, IRCCS Stella Maris Foundation, Pisa, Italy. [3] Meyer Children's Hospital, Firenze, Italy.[4] Department of Information Engineering, University of Pisa, Pisa, Italy. [5] National Institute of Nuclear Physics (INFN), Pisa, Italy. [6] General Electric ASL (EMEA), Pisa, Italy. [7] Department of Translational Research and New Surgical and Medical Technologies, University of Pisa, Pisa, Italy.

This chapter has been published in Journal of Magnetic Resonance Imaging, vol. 44, pp. 1048-1055.

4.1 Abstract

4.1.1 Purpose

To predict local and global Specific Absorption Rate (SAR) in individual subjects.

4.1.2 Materials and Method

SAR was simulated for a head volume coil for two imaging sequences: axial T1-weighted "Zero" Time-of-Echo (ZTE) sequence, sagittal T2-weighted FLuid Attenuated Inversion Recovery (FLAIR). Two head models (one adult, one child) were simulated inside the coil. For 19 adults and 27 children, measured B_1^+ maps were acquired, and global (head) SAR estimated by the system was recorded. We performed t-test between the B_1^+ in models and human subjects. The B_1^+ maps of individual subjects were used to scale the SAR simulated on the models, to predict local and global (head) SAR. A phantom experiment was performed to validate SAR prediction, using a fiberoptic temperature probe to measure the temperature rise due to ZTE scanning.

4.1.3 Results

The normalized B_1^+ standard deviation in subjects was not significantly different from that of the models ($p>0.68$ and $p>0.54$). The rise in temperature generated in the phantom by ZTE was 0.3 °C; from the heat equation it followed that the temperature-based measured SAR was 2.74 W/Kg, while the predicted value was 3.1 W/Kg.

4.1.4 Conclusions

For ZTE and FLAIR, limits on maximum local and global SAR were met in all subjects, both adults and children. To enhance safety in adults and children with 7.0 T MR systems, we suggest the possibility of using SAR prediction.

4.2 Introduction

The management of Specific Absorption Rate (SAR) is a critical issue in MR, especially at ultra-high field (UHF) strength. In fact, at UHF, the energy deposition due to the radiofrequency (RF) field increases and its distribution inside the subject becomes extremely inhomogeneous (1-4). The increase of RF energy deposition and of its spatial variability at UHF is due to the higher operating frequency of the UHF MR system.

MR systems provide an estimation of the global SAR in the subject under test during the exam. During MR exams, global SAR exposure is monitored and must remain below the regulatory limit imposed by the International Electrotechnical Commission (IEC), as given in the standard IEC-60601-2-33. The limit for the head is 3.2 W/kg during any 6-minute time average (5); head SAR limit is based not on whole body weight but on the mass of the head. Head SAR estimation is obtained through empirical formulation, which takes into account the forward and reflected power during MR acquisition, and patient parameters (6). If the global SAR remains below the limit, then the maximum head local SAR should also remain at a safe level, i.e. below the IEC limit of 10 W/kg during any 6-minute time average (5), being the local SAR defined as the SAR averaged over any 10 g of tissue. SAR limits are intended to limit the increase of tissue temperature to safe values, i.e. temperature is the critical parameter (5).

This estimation presents drawbacks, which include the following: i) the monitoring of forward and reflected power is performed in real time, but offers no capability for SAR prediction; ii) global SAR is determined by empirical formulation and thus it is not subject-specific since subject anatomy and subject position with respect to the transmitting coil are not taken into account; iii) local SAR is not evaluated. Moreover, it has been shown that global SAR estimation routines differ from system to system: thus, they should not be taken as the primary and only way to evaluate MR safety (7, 8).

While many B_1^+ field-mapping techniques exist, subject-specific SAR measurements are not available on current MR systems; thus, electromagnetic simulations must be performed for RF fields and SAR analysis. Subject-specific anatomic simulations models would require acquisition and segmentation images of each subject before the MR in question (9, 10): however, such an approach is rarely feasible and therefore models are used instead.

This practice introduces a mismatch between real and simulated data, which can be compensated by simulating and comparing different human models (2, 11).

The purpose of this work is to predict local and global subject SAR exposure in two 7.0 T imaging sequences in both adults and children by combining electromagnetic simulations on two generic anatomic human head models (one adult and one child) with subject-specific B_1^+ maps measured in vivo.

4.3 Materials and Methods

4.3.1 Electromagnetic simulations

The Finite Integration Technique (FIT) in the CST MW Suite (CST-Computer Simulation Technology AG, Darmstadt, Germany) was used. We simulated a ^{1}H quadrature birdcage head coil manufactured by Nova Medical (Wilmington, MA, USA), operating at 298 MHz. In simulations, a human head model derived from the 2×2×2 mm^3 voxel-size anatomic human model Ella (woman, 59 kg), (Virtual population, IT'IS Foundation, Zurich, Switzerland) was placed inside the coil, as shown in Figure 1.

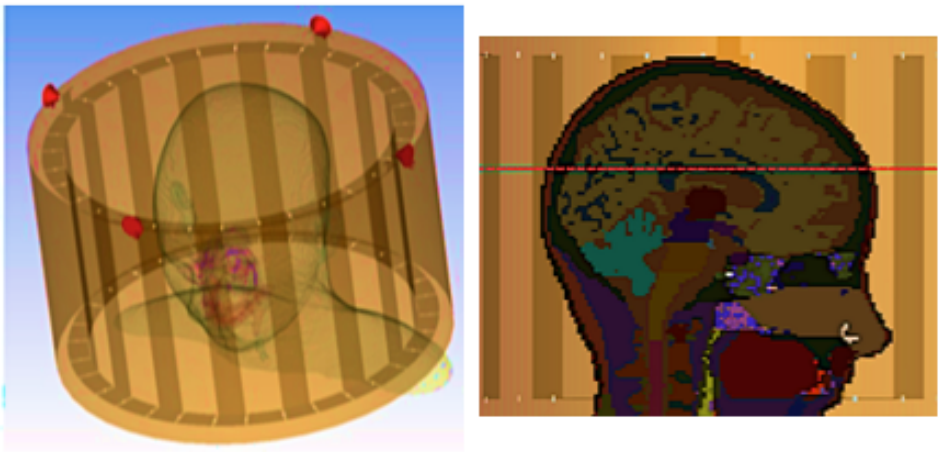

Figure 1: *Left: Ella's head inside the MR quadrature birdcage coil (accessible diameter of 29.5 cm). The 4 red cones displayed in the superior part indicate the 4 sources. Right: Sagittal view of Ella's head inside the birdcage coil (red dots: slice crossing the corpus callosum).*

The coil elements (copper flat strips having width of 2.5 cm and thickness of 35 μm) were equally spaced along a circle of diameter of 29.5 cm, and were connected through two copper end-rings (having width of 1 cm). A quadrature feed with 4 sources of 1W, equally spaced azimuthally by p/2, with a relative electrical phase shift of p/2, was simulated.

B_1^+ was calculated in the axial slice crossing the corpus callosum and in the central sagittal slice. The maximum local SAR [W/kg] (local SAR we report the SAR averaged over 10g) was calculated in the entire head; the global SAR [W/kg] (global SAR we report the SAR averaged over the head) was calculated as well.

The maximum local and global SAR for a given sequence applied on a given slice were then determined by a scaling factor which accounts for all the sequence-related parameters: TR, number and waveform of RF pulses, and the corresponding nominal Flip Angle (FA) averaged on the slice (which are related to the nominal B_1^+, i.e. $B^+_{1,nominal}$). The two sequences addressed in this study were: 1) Axial "Zero" Time-of-Echo (ZTE) sequence ("SILENT") (12, 13) with central slice crossing the corpus callosum and 2) Sagittal FLAIR (14) with central slice through the mid-sagittal plane. Details of each sequence are given in the next sub-sections. The ratio r_{SAR} between maximum local and global SAR was also computed. Next, we simulated various positions of the head model inside the coil: i) rotating the head at 15°, 30°, 45° from the original position on z-axis; ii) moving the head of ±1cm along the 3 axes.

We repeated the simulations with a different human head, derived from the 2×2×2 mm^3 voxel-size anatomic human model Billie, girl, 35 kg, (Virtual population IT'IS Foundation, Zurich, Switzerland).

An overview of the details of anatomic models described above is given in Table 1, while details of the segmented tissue can be found in Tiberi et al. (15).

Model	gender	age [y]	weight [kg]	height [m]	Head maximum axis [mm]	Number of tissues used in the model
Ella	Female	26	58.7	1.63	214	76
Billie	Female	11	35.4	1.47	194	75

Table 1. *Anatomic human models used in this paper.*

Further simulations were performed by placing a homogeneous sphere of radius 90 mm in the center of the coil. The sphere had dielectric constant = 52 and conductivity = 0.55 S/m (thus mimicking the white matter of the human brain (16)). B_1^+ was calculated in the axial slice crossing the center of the sphere, while the maximum local (10g) and global SAR [W/kg] were calculated in the entire sphere. Simulations were repeated decreasing the radius of the sphere to 88 mm, 86 mm and 84 mm, respectively.

To allow comparison with the actual phantom experiments (see the correspondent sub-section), simulations were performed also with a cylindrical phantom having height of 12.5 cm and radius of 3 cm, positioned in the center of the coil and with its axis parallel to the birdcage axis, with dielectric constant = 77.52 and conductivity = 1.886 S/m. B_1^+ was calculated in the axial slice through the center of the cylinder. The maximum local (10g) SAR [W/kg] was calculated in the entire cylindrical phantom for SILENT sequence prescribed axially and centered on the center of the cylinder.

4.3.2 Phantom Experiments

A GE MR950 7T human system (GE HealthCare, Milwaukee, WI, USA) equipped with the birdcage coil mentioned above (operating in quadrature) and with a 32-element receiving array was used. A cylindrical phantom having height of 12.5 cm and radius of 3 cm was placed in the center of the coil, with its axis parallel to the birdcage axis. The phantom was prepared by dissolving agar (7 g/L), NaCl (10 g/L) and $CuSO_4$ (1 g/L) in hot water and then allowing the solution to cool and solidify in the cylindrical plastic former. The recipe was taken from (17); the density of the mixture is 1054 kg/m^3, the heat capacity is 4200 J/kg/°C, the dielectric permittivity is 77.52, the conductivity is 1.886 S/m (all these values are given in (17)). The heat equation for a thermally insulated and nonperfused material with an internal heat source (in our case, SAR) can be written as:

$$c\frac{\Delta T}{\Delta t} = SAR \qquad [1]$$

where c is the heat capacity and ΔT is the temperature rise after a time of Δt (8).

The ΔT generated by SILENT, prescribed axially and centered on the center of the cylinder, was measured with a fiberoptic temperature probe (Neoptix Canada LP, Quebec, Canada, temperature resolution: 0.1 °C) placed at the location of anticipated maximum local SAR. Scan duration Δt was 462 s. The temperature sensor was inserted radially, near the surface of the phantom, on the central axial plane. Before performing the measurement, the phantom was equilibrated to room temperature; thermal insulation was achieved by inserting the phantom in an extruded polystyrene cavity and turning off the patient ventilation fan (8). Thus, by applying eq [1], a temperature-based measurement of SAR was determined. The temperature sensor had a length of approximately 2 cm; since the mass of 2 cm^3 of the agar solution is approximately 10 g, we can assume that the temperature-based measurement of SAR corresponds to a measurement of 10g SAR .

We also acquired a B_1^+ magnitude map ($|B^+_{1,map}|$) in the axial slice crossing the center of the phantom using a Bloch-Siegert sequence (18). Bloch-Siegert parameters are given in the next sub-section. For the slice where $|B^+_{1,map}|$ was measured, a coefficient C, proportional to average($|B^+_{1,map}|$)/$B^+_{1,nominal}$, was calculated (note that $|B^+_{1,map}|$ is obtained from measurements, while $B^+_{1,nominal}$ is obtained from the nominal FA). The coefficient C was then used to scale the maximum local simulated SAR for the SILENT sequence, allowing phantom local SAR prediction. Since C refers to B_1^+, SAR scaling must be performed with a multiplication by C^2 (19).

4.3.3 In-Vivo Measurements

A GE MR950 7T human system (GE HealthCare, Milwaukee, WI, USA) equipped with the birdcage coil mentioned above (operating in quadrature) and with a 32-element receiving array was used. The first 46 patients who completed the scanning protocol of studies "133/11" and "133/11A" (Italian Ministry of Health DGDFSC 0035162-P-09/05/2013 and DGDFSC 0028690-P-08/04/2014) concerning adult and pediatric patients, respectively, with cortical dysplasia and epileptogenic tumors (20, 21) were included in the analysis.

Participants were 19 adults (aged 18-42 y; weight ranging between 46 kg and 100 kg; 14 subjects with cortical dysplasia and 5 with epileptogenic tumors; 10 males and 9 females) and 27 children (aged 9-17 y; weight ranging between 27 kg and 95 kg; 19 subjects with

cortical dysplasia and 8 with epileptogenic tumors; 16 males and 11 females). Subjects were placed in the scanner in supine position, head first, as in simulations (Figure 1). Written informed consent was obtained from all adult subjects, and from parents or guardians of all children. All procedures performed in this study were in accordance with the ethical standards of the institutional and/or national research committee and with the 1964 Helsinki declaration and its later amendments or comparable ethical standards. The research project was approved by the Ethical Committee of Meyer Children's Hospital, Firenze, Italy and it was carried out in accordance with the Code of Ethics of the World Medical Association (Declaration of Helsinki) for experiments involving humans.

For each subject: we recorded age and weight. We acquired B_1^+ magnitude maps ($|B^+_{1,map}|$) with a Bloch-Siegert sequence (18) centered on slices corresponding to those used in the simulations: parameters TR=33 ms, TE=15 ms, bandwidth=15.6 kHz, slice thickness=3.5mm, matrix-size 64x64, square FOV 22 cm, 2 averages (acquisition time: 9 s per slice). For the axial slice, we calculated the average of $|B^+_{1,map}|$ and standard deviation of $|B^+_{1,map}|$ for a FA=90° sinc-pulse. We also recorded the values of global (head) SAR estimated by the system during the two 3D whole-brain sequences that were common to all subjects (the other sequences in the scanning protocol were tailored to each case, and they targeted different brain regions).

The two sequences assessed were: 1) Axial "Zero" Time-of-Echo (ZTE) sequence ("SILENT") (12, 13), 384 FA=4° hard pulses of duration=12 μs and 5 inversion and saturation pulses per TR (TR=525 ms), TE=16 μs, post-segment time of delay TD=2 s, FOV=192x192x192mm^3, data matrix=192x192x192 (resulting in a spatial resolution of 1x1x1mm^3); 2) Sagittal FLAIR (14), 240 FA=120° hard pulses of duration=336 μs per TR (TR=8 s), TE=122.4 ms, TI=2048 ms, FOV=202x202x155.4 mm^3, data matrix=288x288x222 (resulting in a spatial resolution of 0.7x0.7x0.7mm^3).

4.3.4 SAR Prediction by Combining B_1^+ In-Vivo Measurements with Electromagnetic Simulations

For each subject and for each slice where $|B^+_{1,map}|$ was measured, a coefficient *C*, proportional to average($|B^+_{1,map}|$)/$B^+_{1,nominal}$, was calculated (note that $|B^+_{1,map}|$ is obtained from measurements, while $B^+_{1,nominal}$ is obtained from the nominal FA). The subject-

dependent coefficient C is then used to scale the SAR obtained through electromagnetic simulations on the generic anatomic models, predicting both local and global SAR; in this context, the choice to use SAR simulated in Ella or in Billie is made on a subject-weight basis; specifically for subjects whose weight was ≥ 47 kg (the average weight between Ella and Billie) we used SAR simulated in Ella, while for the others we used SAR simulated in Billie. Since C refers to B_1^+, SAR scaling must be performed with a multiplication by C^2 (19). The predicted maximum local SAR was derived by multiplying the predicted global SAR by the correspondent r_{SAR}

4.3.5 Statistical Analysis

We calculated the relative error between predicted SAR and temperature based SAR measurement in phantom. To validate the birdcage coil model for the head simulation studies, we calculated the normalized standard deviations (the ratio between standard deviation and average) of B_1^+ magnitude map were calculated in each subject; such normalized standard deviations were compared to those in either Ella (for subjects heavier than 47kg) or Billie (for subjects lighter than 47 kg) with a t-test.

For adults (age ≥18 years) and children we calculated the maximum, minimum, average and standard deviation of age and weight. For adults and children and for each sequence, we calculated the maximum, minimum, average and standard deviation of predicted global SAR. The lines of regression of both estimated and predicted global SAR with respect to the subject weight were also determined.

4.4 Results

The measured ΔT generated in the cylindrical phantom by SILENT was 0.3 °C; therefore from Eq. [1] the temperature-based SAR measurement was 2.74 W/Kg. The predicted phantom maximum local SAR (10 g) for SILENT sequence was 3.1 W/Kg. The relative error between predicted SAR and temperature based SAR measurement was 11%.

Figure 2 shows: the measured $|B^+_{1,map}|$ for a FA=90° sinc-pulse axial slice, acquired on the scanner for 8 subjects (selected arbitrarily among the participants, for demonstration purpose only); the simulated B^+_1 magnitude for a FA=90° sinc-pulse, axial slice, in Billie

and Ella. For visual comparison, the B^+_1 fields were normalized to the correspondent maximum value in the slice center. Weights, ages, average and standard deviation of B^+_1 magnitude before normalization are given in the insert. Concerning the average of B^+_1 magnitude before normalization, the values which refer to Billie and Ella are equal to 7.2 μT, i.e. the $B^+_{1,nominal}$ for the FA=90° sinc-pulse (having length of 3.2 ms); conversely, the values which refer to the 8 subjects vary from 6.55 μT to 6.97 μT.

The average of normalized standard deviations of B^+_1 magnitude in all participants heavier than 47 kg was 0.209, and was not significantly different from 0.211 found in Ella (t-test, $p>0.68$). The average of normalized standard deviations the B^+_1 magnitude in subjects whose weight was < 47 Kg was 0.196, and was not significantly different from 0.200 obtained in Billie (t-test, $p>0.54$).

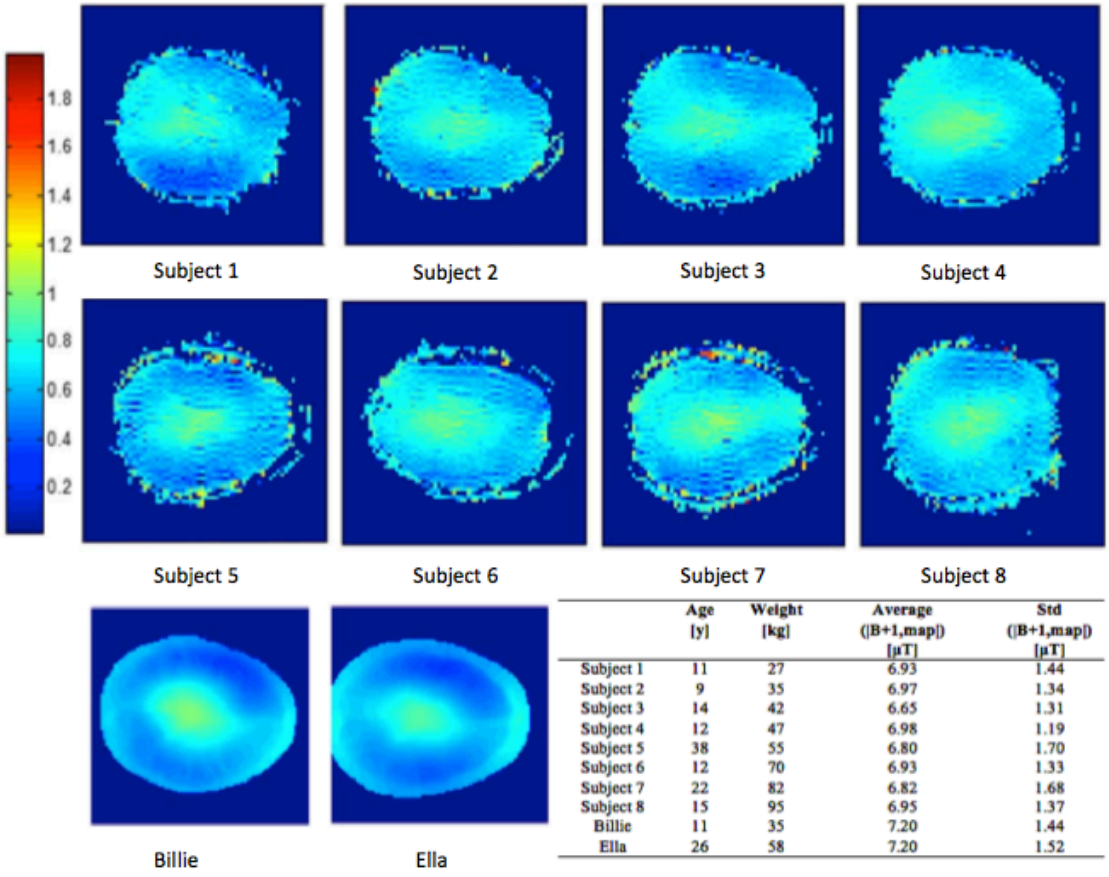

	Age [y]	Weight [kg]	Average (|B+1,map|) [μT]	Std (|B+1,map|) [μT]
Subject 1	11	27	6.93	1.44
Subject 2	9	35	6.97	1.34
Subject 3	14	42	6.65	1.31
Subject 4	12	47	6.98	1.19
Subject 5	38	55	6.80	1.70
Subject 6	12	70	6.93	1.33
Subject 7	22	82	6.82	1.68
Subject 8	15	95	6.95	1.37
Billie	11	35	7.20	1.44
Ella	26	58	7.20	1.52

Figure 2: *Measured $|B^+_{1,map}|$ for a FA=90° sinc-pulse [normalized unit], axial slice, FOV= 22 cm x 22 cm, acquired on the scanner for 8 subjects; the simulated B^+_1 magnitude for a FA=90° sinc-pulse, axial slice, FOV= 22 cm x 22 cm, in Billie and Ella. For visual comparison, the B^+_1 fields were normalized to the correspondent maximum value achieved in the central region. Weights, ages average and standard deviation of B^+_1 magnitude are given in the insert (before*

normalization). The 8 subjects shown in this figure have been selected arbitrarily among the participants for demonstration purpose only.

Table 2 shows the highest values with respect to model positions inside the coil, obtained for maximum and global SAR in Ella and Billie after scaling the simulations to achieve the B_1^+ magnitude average value of 1 μT in the axial or sagittal slices.

Model	Max(SAR) [W/kg] after scaling axial B1+ to 1 μT	Global (SAR) [W/kg] after scaling axial B1+ to 1 μT	Max(SAR) [W/kg] after scaling sag B1+ to 1 μT	Global (SAR) [W/kg] after scaling sag B1+ to 1 μT
Ella (adult)	1.73	0.56	1.76	0.57
Billie (child)	1.85	0.68	1.54	0.51

Table 2. *Maximum and global SAR in Ella/Billie after scaling the simulations to achieve the B_1^+ magnitude average value of 1 μT in the axial/sagittal slices.*

Table 3 shows the highest values with respect to model positions obtained for maximum and global SAR in SILENT and FLAIR sequence in Ella and Billie. The highest r_{SAR} is 3.4 for Ella and 3.2 for Billie.

Model	Max local SAR,SILENT [W/kg]	Global SAR, SILENT [W/kg]	Max local SAR, FLAIR [W/kg]	Global SAR, FLAIR [W/kg]
Ella (adult)	7.6	2.47	9.48	3.07
Billie (child)	8.2	2.8	8.3	2.85

Table 3. *Maximum and global SAR in Ella/Billie in SILENT/FLAIR sequence.*

The SAR analysis performed on generic anatomic models is then combined with the subject-specific $|B^+_{1,map}|$. In Figure 3a and Figure 3b we report the values of global SAR predicted by our method and estimated by the MR system for the SILENT sequence in 19 adults and 27 children; Figure 3d and Figure 3e refer to the FLAIR sequence. Figure 3c and Figure 3f show the values of global SAR predicted by our method and estimated by the MR system for both sequences with respect to weight. The slope of the regression lines are 0.011 W/kg for the SILENT estimated global SAR (offset=0.88 W/kg) and 0.017 W/kg for the FLAIR estimated global SAR (offset=0.95 W/kg). The slope of the regression line for the SILENT predicted global SAR (offset=2.17 W/kg) can be assumed equal to 0, being

the maximum difference (in the weight range here considered) <1/200 of the offset. Also the slope of the regression line for the FLAIR predicted global SAR (offset=2.59 W/kg) can be assumed equal to 0, being the maximum difference (in the weight range here considered) <1/200 of the offset.

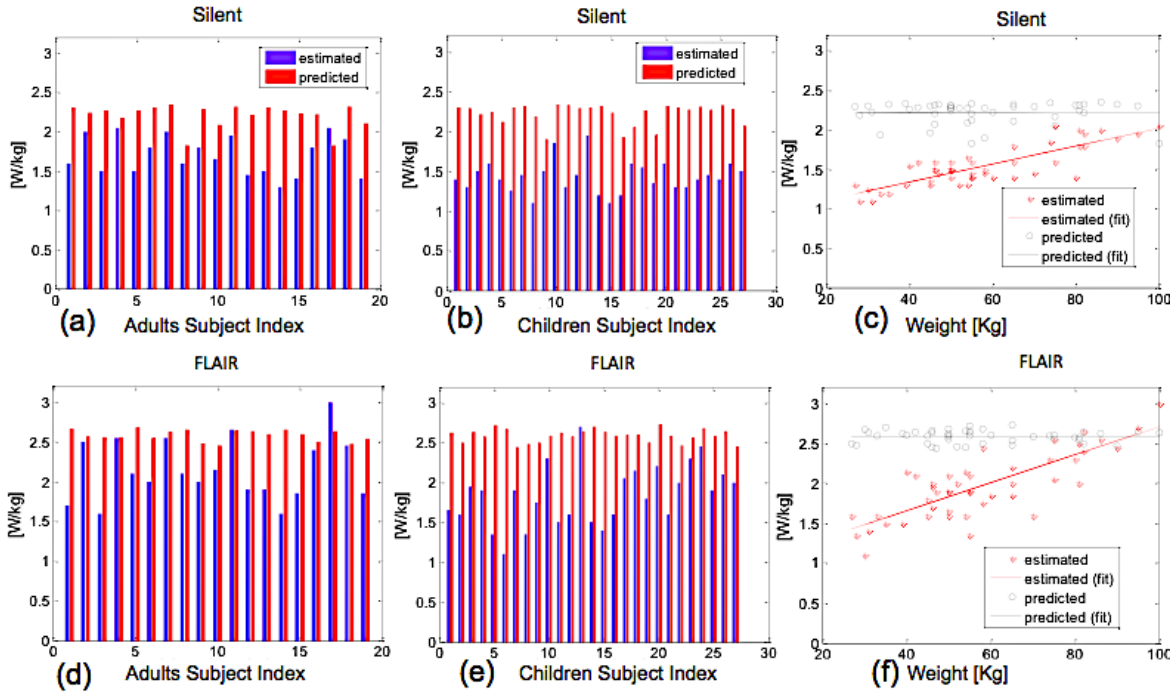

Figure 3: *a,d: Global SAR predicted by the proposed method and estimated by the system for SILENT and FLAIR sequence in 19 adults. b,d: Global SAR predicted by the proposed method and estimated by the system for SILENT and FLAIR sequence in 27 children. c,f: global SAR predicted by the proposed method and estimated by the system for SILENT and FLAIR sequences with respect to subjects weight; linear fit plots are also given.*

Table 4 summarizes the minimum, maximum, average and standard deviation of the age, weight and predicted global SAR for the 19 adults and 27 children used in this study.

	age [y]	weight [kg]	SILENT, predicted global SAR [W/kg]	FLAIR, predicted global SAR [W/kg]
adults, min	18	46	1.83	2.45
adults, max	42	100	2.35	2.68
adults, avg	29.1	67.5	2.2	2.58
adults, std	6.5	16.4	0.15	0.07
children, min	9	27	1.9	2.44
children, max	17	95	2.34	2.73
children, avg	12.4	50.7	2.2	2.58
children, std	2.2	17	0.12	0.08

Table 4. *Minimum (min), Maximum (max), Average (avg) and Standard Deviation (std) of the Age, Weight and Predicted Global SAR for the 19 adults and 27 children used in this study. The two sequences here considered are axial SILENT, sagittal FLAIR.*

Figure 4 shows the predicted maximum local SAR for both sequences for all the subjects.

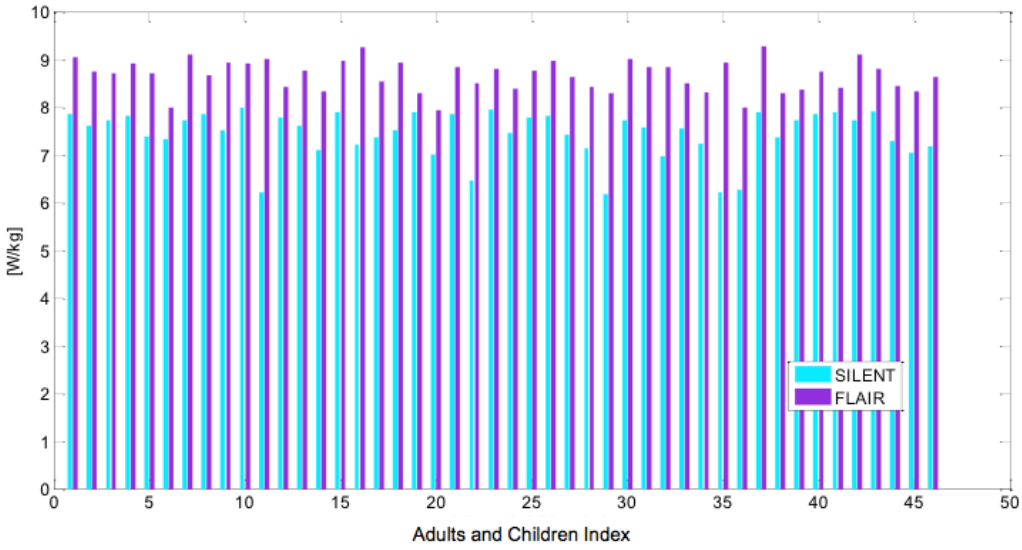

Figure 4. *Predicted maximum local SAR for SILENT and FLAIR for all the subjects.*

Table 5 refers to the simulations using homogeneous spheres with different radii: specifically, the second and third column of Table 5 show the global and maximum local SAR after scaling the simulations to achieve the same B_1^+ magnitude average value of 1μT. In the spheres here simulated, r_{SAR} oscillates slightly (<3%) around the mean value of 1.36.

	Global (SAR) [W/kg] after scaling axial B1+ to 1 μT	Max(SAR) [W/kg] after scaling axial B1+ to 1 μT
Sphere 90 mm radius	0.412	0.575
Sphere 88 mm radius	0.404	0.549
Sphere 86 mm radius	0.398	0.545
Sphere 84 mm radius	0.390	0.526

Table 5. *Maximum and global SAR in homogeneous spheres with different radii after scaling the simulations to achieve the B_1^+ magnitude average value of 1 μT in the central axial slices.*

4.5 Discussion

SAR regulatory limits do not distinguish between adults (age ≥18 years) and children, but particular care must be paid when scanning juvenile subjects due to the lack of data on children SAR exposure at UHF in the literature. We predicted, for a 7.0 T system, the global (head) and local subject-specific SAR exposure for two 3D whole-brain sequences, namely SILENT and FLAIR, by combining B_1^+ in-vivo measurements (that have a short acquisition time: 9 s per slice) with electromagnetic simulations. We introduced a safety margin by choosing the worst-case simulated SAR. Limits on maximum local and global SAR were met in all subjects, both adults and children. The FLAIR sequence resulted more SAR demanding than the SILENT sequence.

The ratio r_{SAR} quantifies the hot spots, i.e. the locations where the maximum local SAR occurs; r_{SAR} is calculated through simulations. The r_{SAR} in Ella and Billie is more than twice the r_{SAR} in spheres. A high r_{SAR} , i.e. r_{SAR}>3.13 (where 3.13 is the ratio between the maximum local SAR limit = 10 W/kg and the global head SAR limit = 3.2 W/kg), can occur

at 7.0 T; this is due to the operating frequency which gives a wavelength in tissue comparable with the head dimensions and results in major field distortions. Hot spots depend on each head's unique features and on its position inside the coil. In our simulations we found that the highest r_{SAR} is 3.4 for Ella (very similar to what was reported in (22), where a different anatomic model has been used) and 3.2 for Billie; such r_{SAR}>3.13 implies that maximum local SAR limit can be reached before global SAR limit.

A good agreement was bserved between the temperature-based measured SAR on phantom and the predicted one, with a relative error of 11%. The residual discrepancy may be related to the temperature resolution of the probe and to approximations in the heat capacity value of the agar solution (17).

Simulated and measured $B^{+}_{1,map}$ had the same qualitative appearance; all the simulated and measured maps exhibited the typical central focusing effect and a slight left/right asymmetry, observed also in (23) where a similar coil with a different human head model obtained through a manual segmentation was used. Despite subjects had different weight, size and age, the normalized standard deviation of their $|B^{+}_{1,map}|$ was not significantly different from the normalized standard deviation of the maps obtained with Ella and Billie. Specifically, the average normalized standard deviation in subjects heavier than 47 kg was not significantly different from that of Ella (t-test, p>0.68), and in patients whose weight was < 47 Kg it was not significantly different from that of Billie (t-test, p>0.54).

|B+1,map| for FA=90° gives the field, produced by the MR scanner after RF power calibration, for maximum signal intensity (4), since RF power is calibrated from a projection of the slice signal intensity. The high dielectric constant of human tissues (15) leads to very inhomogeneous B_1^{+} maps, which explains why $|B^{+}_{1,map}|$ values can differ from $B^{+}_{1,nominal}$. B_1^{+} maps were acquired in each subject to calculate the coefficient C to be used in scaling the simulations. From electromagnetic theory it can be demonstrated that the same coefficient holds for scaling both the magnetic and the electric field, while C^2 holds for SAR, being the SAR proportional to the square of the electric field (22); the ratio r_{SAR} instead is not affected by simulation scaling. The use of B_1^{+} maps for scaling the simulations does not require any information about transmitted power, reflected power, or power lost in the transmitting chain.

From the simulations we observe that: for the axial slice (and, thus, in calculations related to SILENT sequence) SAR is higher in Billie (this is in agreement with what reported in

(15)); for the sagittal slice (and, thus, in calculations related to FLAIR) SAR is higher in Ella.

By considering the global SAR predicted by our method, we observed that SAR exposure does not increase with subject weight; this finding is consistent with what was reported in (11). To be thorough, we also reported the values of global SAR estimated by the system, and we observed that, according to these data, the SAR exposure seems to increase with subject weight. This finding is consistent with what was previously reported in (24), however it should be noted that the MR system estimates global SAR by means of an empirical formulation using data that are not directly accessible by the experimenters, such as the reflected RF power and the fraction of subject's mass that is exposed to RF (in our case, the head) (6). For example, in our scanner the head mass exposed to RF is determined directly by the system using an equation (whose details are not disclosed to the vendor's customers) that combines subject weight and coil parameters. This type of empirical formulae for estimating SAR assume homogeneous loads and unperturbed magnetic field; however, such assumptions are not valid for human heads using a 7.0 T birdcage coil, and the RF fields generated by the coil inside the heads are highly inhomogeneous.

To simulate SAR exposure, we used two different anatomical models. While there was a substantial difference in age and weight of the two models, they do not represent the true anatomical variability of clinical patients, Here, Ella and Billie were used because they were felt to be representative of the worse case SAR scenarios for adults and children, respectively (15). One limitation of our study is the fact that the variation of dielectrical properties of tissues with age was not considered. However, Wang et al. (25) have shown that variation of dielectrical properties of tissues with age does not affect significantly the SAR (i.e., less than 10% in the extreme case). Further, a phantom experiment for validating the SAR prediction has been performed on a homogenous cylinder, while validation of the birdcage coil model for the head simulation studies has been performed using a limited number of subjects; experiments on anthropomorphic phantoms and a higher number of subjects would increase the confidence of SAR prediction. The present study has been performed using the 7.0 T system of one single vendor equipped with a quadrature head coil; moreover, only two sequences have been considered.

In conclusion, here we suggest to predict SAR exposure by combining B1+ in-vivo measurements with electromagnetic simulations; in case limits are exceeded by

predictions, appropriate actions can be taken before further scanning, such as by decreasing RF power and/or increasing TR (where possible). Although we are aware that there is no abrupt physiological change at the age of 18 years, throughout the paper we maintained the regulatory distinction between adults and minors to highlight that the use of the studied sequences at 7.0 T is safe, concerning SAR exposure and according to our predicted local and global SAR, in both adults and children.

4.6 Acknowledgment

Contract grant sponsor: Pisa Foundation (Project 133/11, "Ultra-high field MRI targeted imaging of dysplastic cortical lesions and dysembryoplastic tumours"); Italian Ministry of Health, RC 5/2015 to IRCCS Fondazione Stella Maris; the European Union Seventh Framework Programme FP7/ 20072013 (under the project "DESIRE: Development and Epilepsy: Strategies for Innovative Research to improve diag- nosis, prevention and treatment in Children with difficult to treat Epilepsy", Grant Agreement: 602531). We thank Patrick J. Ledden for the helpful discussions in coil modelling.

4.7 References

1. Collins CM, Li S, Smith MB. SAR and B1 field distributions in heterogeneous human head model within a birdcage coil. Magn Reson Med 1998;40:846–856.

2. Collins CM. Numerical field calculations considering the human subject for engineering and safety assurance in MRI. NMR Biomed 2009; 22:919–926.

3. Kraff O, Fischer A, Nagel AM, Christoph M, Ladd ME. MRI at 7 Tesla and above: demonstrated and potential capabilities. J Magn Reson Imaging 2015;41:13–33.

4. Vaughan JT, Garwood M, Collins CM, et al. 7T vs. 4T: RF power, homogeneity, and signal-to-noise comparison in head images. Magn Reson Med 2001;46:24–30.

5. International Electrotechnical Commission. International Standard. Medical electrical equipment - Part 2-33: particular requirements for the safety of magnetic resonance equipment for medical diagnosis. Edition 2.2. 60601-2-33.

6. Van Osch MHP, Webb AW. Safety at ultra-high field MRI: what are the specific risks? Curr Radiol Rep 2014;2:1–8.

7. Baker KB, Tkach JA, Nyenhuis JA, et al. Evaluation of specific absorption rate as a dosimeter of MRI-related implant heating. J Magn Reson Imaging 2004;20:315–320.

8. Sammet CL, Yang X, Wassenaar PA, et al. RF-related heating assessment of extracranial neurosurgical implants at 7T. Magn Reson Imaging 2013;31:1029–1034.

9. Homann H, Bo€rnert P, Eggers H, Nehrke K, Do€ssel O, Graesslin I. Toward individualized SAR models and in vivo validation. Magn Reson Med 2011;66:1767–1776.

10. Voigt T, Homann H, Katscher U, Doessel O. Patient-individual local SAR determination: in vivo measurements and numerical validation. Magn Reson Med 2012;68:1117–1126.

11. de Greef M, Ipek O, Raaijmakers AJE, Crezee J, van den Berg CAT. Specific absorption rate intersubject variability in 7T parallel transmit MRI of the head. Magn Reson Med 2013;69:1476–1485.

12. Madio DP, Lowe IJ. Ultra-fast imaging using low flip angles and FIDs. Magn Reson Med 1995;34:525–529.

13. Costagli M, Symms MR, Angeli L, et al. Application of "Zero" Time- of-Echo (ZTE) MRI sequence for "Silent" T1-weighted imaging at 7.0 Tesla. In: Proceedings of the European Congress of Radiology (ECR), Wien, Austria, 2015. B-1083.

14. Saranathan M, Tourdias T, Zeineh M, et al. Optimization of Cube- FLAIR 3D FSE Imaging at 7T. In: Proceedings of the 21st Annual Meeting of ISMRM, Salt Lake City, 2013. (abstract 248).

15. Tiberi G, Fontana N, Costagli M, et al. Investigation of maximum local specific absorption rate in 7T magnetic resonance with respect to load size by use of electromagnetic simulations. Bioelectromagnetics 2015;36:358–366.

16. Zhang X, Liu J, Schmitter S, Van de Moortele PF, He B. B1-based SAR estimation for human brain imaging with average brain property values substitution. In: Proceedings of the 21st Annual Meeting of ISMRM, Salt Lake City, 2013. (abstract 4429).

17. Oh S, Webb AG, Neuberger T, Park B, Collins CM, Experimental and numerical assessment of MRI-induced temperature change and SAR distributions in phantoms and in vivo. Magn Reson Med 2010;63:218– 223.

18. Sacolick, LI, Wiesinger F, Hancu I, Vogel MW. B1 mapping by Bloch- Siegert shift. Magn Reson Med 2010;63:1315–1322.

19. Cassidy PJ, Grieve S, Clarke K, Edwards DJ. Electromagnetic charac- terisation of MR RF coils using the transmission-line modelling method. MAGMA 2002;14:20–29.

20. De Ciantis A, Barkovich AJ, Cosottini M, et al. Ultra-high-field MR imaging in polymicrogyria and epilepsy. AJNR Am J Neuroradiol 2015;36:309–316.

21. De Ciantis A, Barba C, Tassi L, et al. 7T MRI in focal epilepsy with unrevealing conventional field strength imaging. Epilepsia 2016;57:445–454.

22. Restivo MC, van den Berg CA, van Lier AL, et al. Local specific absorption rate in brain tumors at 7 tesla. Magn Reson Med 2016;75:381–389.

23. van Lier AL, Kotte AN, Raaymakers BW, Lagendijk JJ, van den Berg CA. Radiofrequency heating induced by 7T head MRI: thermal assessment using discrete vasculature or Pennes' bioheat equation. J Magn Reson Imaging 2012;35:795–803.

24. Bottomley PA, Redington RW, Edelstein WA, Schenck JF. Estimating radiofrequency power deposition in body NMR imaging. Magn Reson Med 1985;2:336–349.

25. Wang J, Fujiwara O, Watanabe S. Approximation of aging effect on dielectric tissue properties for SAR assessment of mobile telephones. IEEE Trans Electromagn Compatibil 2006;48:408–413.

Chapter 5.

In Vivo 7T MR Spectroscopy in patients with brain lesions: Preliminary Data

5.1 Introduction

MRS is a non-invasive tool for investigating metabolism in the brain. Important applications of MRS are in providing information for diagnosis, monitoring progression and evaluating therapy in brain lesions. Localized proton MRS of the human brain, first reported more than 20 years ago (Bottomley et al. 1985; Hanstock et al. 1988; Frahm et al. 1989), today is used clinically in many medical centres worldwide for the evaluation of brain lesions, however, it has not been established yet as a routine tool for clinical diagnostics.

The recent availability of 7T human MR scanners for clinical applications offers advantages in higher SNR and enhanced spectra quantification (Mekle et al. 2009) improving spatial resolution and detection of a higher range of metabolites in the brain (Grams et al. 2011; Tkáč et al. 2001; Tkáč and Gruetter 2005; Mekle R et al. 2009). In the past few years several clinical papers has been published describing advantages of 7T MRS in specific brain diseases such as brain tumors (Li et al., 2015a; Li et al., 2015b; Emir et al. 2016) and epilepsy (Pan et al. 2013a; Pan et al. 2013b; Pan et al. 2015; Cai et al. 2012) allowing the quantification of more metabolites than at lower field strengths (Tkáč et al., 2009).

We evaluate the metabolite quantification on a series of 24 patients with brain lesions using 7T 1H MRS. In this chapter our preliminary results and the description of three cases were reported.

5.2 Methods

5.2.1 Patients

We enrolled, from our Hospital (Child Neurology Unit, Paediatric Neurosurgery, Neuro-Oncology Unit at Children's Hospital A. Meyer - University of Florence), 24 patients (12 adults, 12 children; 15 female, 9 male) (Table 1). All patients were previously imaged at lower filed strengths for clinical diagnosis. We used the following inclusion criteria: 1) age ≥ 8 years; 2) MRI lesion visible at conventional field strengths. Exclusion criteria: 1) any contraindications to MRI; 2) the need of sedation for MRI scanning and 3) lack of consent.

The experimental protocol was approved by the Italian Ministry of Health and the Pediatric Ethics Committee of the Tuscany Region, Italy. The procedures followed were in accordance with institutional guidelines and included an adverse event form. Written informed consent was obtained from all adult patients or from the parents for juvenile subjects.

No.	Sex	Age	MRI findings	Voxel location	Spectral quality
1	F	13	FCD	Lesion	Good
2	M	19	Tumor	Lesion	Good
3	M	57	Tumor	Lesion + Contralateral	Good
4	M	14	Tumor	Lesion + Contralateral	Good
5	F	22	Tumor	Lesion	Poor/ Rejected
6	M	28	Tumor	Lesion	Good
7	F	26	Tumor	Lesion	Poor/ Rejected
8	F	11	Tumor	Lesion	Poor/ Rejected
9	M	14	Tumor	Lesion	Poor/ Rejected
10	F	12	Tumor	Lesion	Poor/ Rejected
11	F	10	Tumor	Lesion	Poor/ Rejected

12	M	24	Tumor	Lesion	Good
13	F	33	Tumor	Lesion	Poor/ Rejected
14	F	10	Tumor	Lesion	Poor/ Rejected
15	F	23	Tumor	Lesion	Good
16	F	34	Tumor/ Inflammatory lesion	Lesion + Contralateral	Good
17	F	16	Tumor/ Pseudoprogression	Lesion	Good
18	M	13	Tumor/FCD	Lesion	Good
19	F	26	Tumor/FCD	Lesion	Good
20	F	20	Tumor	Lesion	Poor/ Rejected
21	M	11	Tumor	Lesion + Contralateral	Good
22	F	14	Tumor	Lesion	Good
23	F	15	Tumor	Lesion	Good
24	M	25	Tumor	Lesion	Poor/ Rejected

Table 1. Clinical data in 24 patients acquired.

5.2.2 MR Imaging and Spectroscopy

7T structural MR imaging and MR spectroscopy were performed using a Discovery MR 950 MR scanner (GE Healthcare) equipped with a 2-channel transmit/32-channel receive head coil (Nova Medical, Wilmington, Massachusetts). All participants received earplugs and a pair of pads covering the ears to limit acoustic noise and to minimized head movement.

The examination protocol consists in several steps (Figure 1).

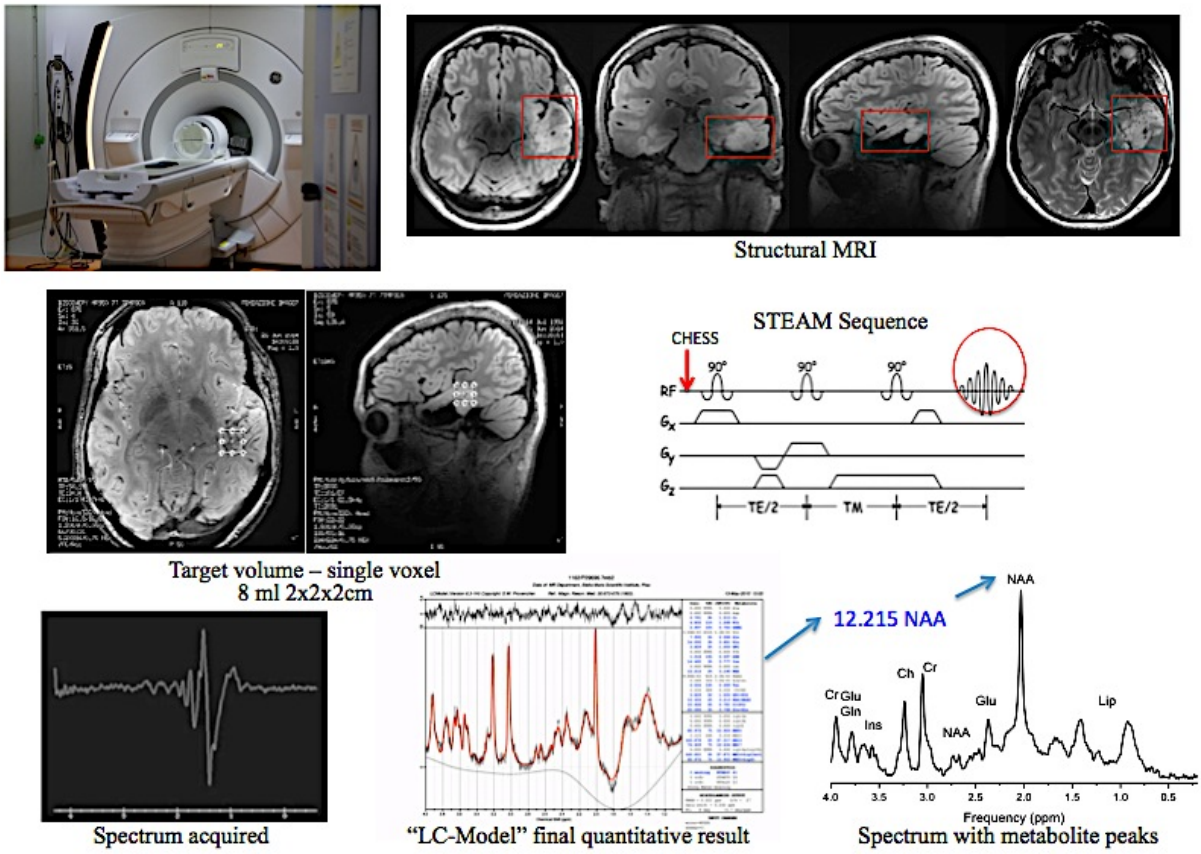

Figure 1. Schematic illustration of the process used to obtain the spectrum of metabolites passing though 7T MRI acquisition, selection of volume of interest (VOI), acquisition of single voxel 7T MRS and data quantification with LC-Model.

We used a dedicated epilepsy research MRI protocol for the anatomical study including the following sequences: 3D T1-weighted FSPGR, 3D susceptibility-weighted angiography (SWAN), 2D T2*-weighted targeted dual-echo gradient-recalled echo (GRE), 2D T2-weighted FSE, 2D grey-white matter tissue border enhancement (TBE) FSE-IR and 3D MP-FLAIR sequences. No contrast medium was injected. MR imaging was used for depiction of morphological brain lesion changes and was an important step for the positioning of the Volume of Interest (VOI) for a single voxel spectroscopy followed by global and localized shim. A cubic volume 2 x 2 x 2 cm3 was positioned inside the region exhibiting the lesion. The voxel was selected through a combination of slice-selective

excitations in three dimensions in space, obtained when a RF pulse is applied and, at the same time, a field gradient is switched on.

A STEAM (STimulated Echo Acquisition Mode) sequence was used for acquiring the MRS data. The STEAM pulse sequence consists of three 90° pulses and relative gradients for a full localization of the voxel in the three spatial dimensions. The STEAM localization scheme can achieve shorter echo times with respect to the PRESS sequence (which uses two 180° refocusing pulses instead of the last two 90° pulses of STEAM), but at the expense of lower SNR. Each dataset of the STEAM sequence is composed by 128 repetitions, which means 128 FIDs each composed of 32 signals from the 32 receiver coil elements. For water suppression the CHESS sequence was used prior to the STEAM localization scheme. CHESS consists in applying optimized frequency selective RF pulses and subsequent suitable field gradients for dephasing water coherences. The major advantages that can be obtained with the use of High-field 1H-MRS are greater SNR and spectral resolution, which can turn to greater spatial and/or temporal resolution and enable the acquisition of high quality spectra or reduction of acquisition time (Zhu and Barker 2011).

As a result, high-field 1H-MRS might allow higher precision in measurement of well-known metabolites (N-acetylaspartate, Choline, creatine/phosphocreatine, myoinositol, lactic acid and lipids), and detection of many novel metabolites not visible at lower fields (glutamate, glutamine, taurine, aspartate, GABA). However, these advantages may be hampered by intrinsic field-dependent technical difficulties, such as increased T2 signal decay, chemical shift displacement errors, increased magnetic susceptibility, magnetic field inhomogeneities, safety issues.

5.2.3 Post-processing and Metabolite Quantification

Data analysis was performed by a physicist with a home-made routine in Matlab (MathWorks, Natick, USA), and consisted in zero-filling, coil combination, Gaussian apodization (1.25 Hz for in-vitro and 4 Hz for in-vivo acquisitions), frequency alignment of the water line (applied only to in-vivo acquisitions), internal water reference, FID average, Fast Fourier Transform, residual water subtraction, and DC correction.

MRS data were quantified using LC-Model software. The software fits the in vivo spectrum as a combination of pure model spectra from each of the compounds in the brain. Furthermore, the model includes automatic phase correction and baseline correction, or the baseline may also be modelled as a combination of macromolecular resonances (Figure 2).

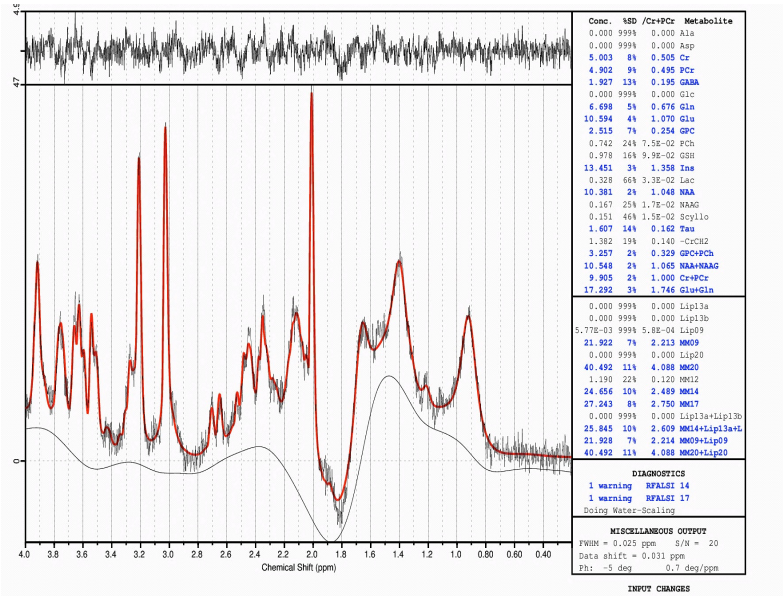

Figure 2: Example of quantitative result using LC Model. The difference between the original experimental data and the results of the curve-fit is shown in the top trace. Metabolite concentrations highlighted in bold corresponds to those with an estimated uncertainty of less 20%.

5.3 Illustrative cases

5.3.1 Focal Cortical Dysplasia (FCD)

Focal cortical dysplasia is a frequent cause of drug-resistant focal epilepsy (Widdess-Walsh et al. 2005). The identification of FCD by MR imaging allows patients with pharmaco-resistant epilepsy to undergo resective surgery (Guerrini et al. 2015). ^{1}H MRS providing quantitative information about the metabolic composition of brain tissue in vivo may allow identification of potential epileptogenic lesion. Spectra measured by MRS in patients with FCD type II show an increase of relative Cho, increase of relative Ins and a reduction of NAA (Tschampa et al. 2015; Kuzniecky et al. 1997; Mueller et al. 2005; Simone 1999; Kaminaga et al. 2001; Fellah et al. 2012).

5.3.2 Case 1

13 years old female with right frontal epilepsy. 7T MRI detected right frontal FCD.

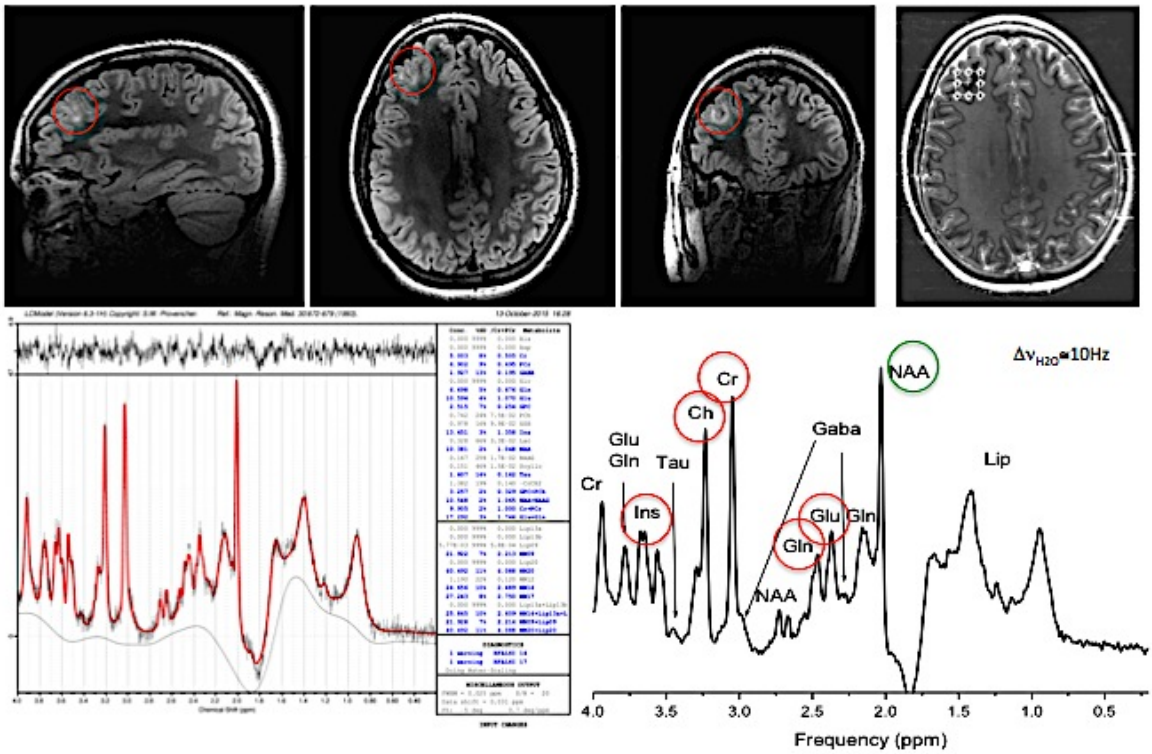

The selection of VOI was positioned on TBE image on the right frontal lobe. The spectrum measured in vivo with STEAM short TE shows an increase of relative Choline (Ch), Inositol (Ins), Creatine (Cr), Glutamate (Glu) and Glutamine (Gln) (red circles) and a very slight reduction of signal intensity of *N-acetylaspartate (*NAA) (green circle). The frequency resolution between individual peaks increases at 7T as a consequence the peaks of Glutamate (Glu) and Glutamine (Gln) are clearly separated (red circles) with respect to lower field strengths where they are usually superimposed.

5.3.3 Tumors

Nearly all brain tumors show (Riyadh et al. 2006; Majos et al. 2004; Li et al. 2015; Graaf 2010):

- decreased N-acetyl aspartate (NAA) signals interpreted as loss, dysfunction or displacement of normal neuronal tissue (NAA is believed to be primarily of neuronal and axonal origin)

- increased levels of Choline (Cho) suggested as increased membrane turnover (Cho is contained in different compounds involved in membrane synthesis and degradation)

- elevated signals in lactate region due to anaerobic glycolysis, insufficient blood flow leading to ischemia and necrosis

- elevated signals in lipid region due to necrosis and membrane breakdown

- sometime increased levels of myoinositol (Ins) due to the increased numbers of glial cells

Unfortunately, the spectrum obtained in the evaluation of brain tumors may vary greatly depending on the region that is sampled by MRS and the fact that the tumors are commonly heterogeneous, with necrotic cores, proliferative rims and invasion of surrounding brain tissue (Horská and Barker 2010).

5.3.4 Case 2

56 years old male with left fronto-parietal epilepsy. 7T MRI revealed high-grade tumor in left rolandic region. Histological diagnosis: glioblastoma multiforme (WHO IV).

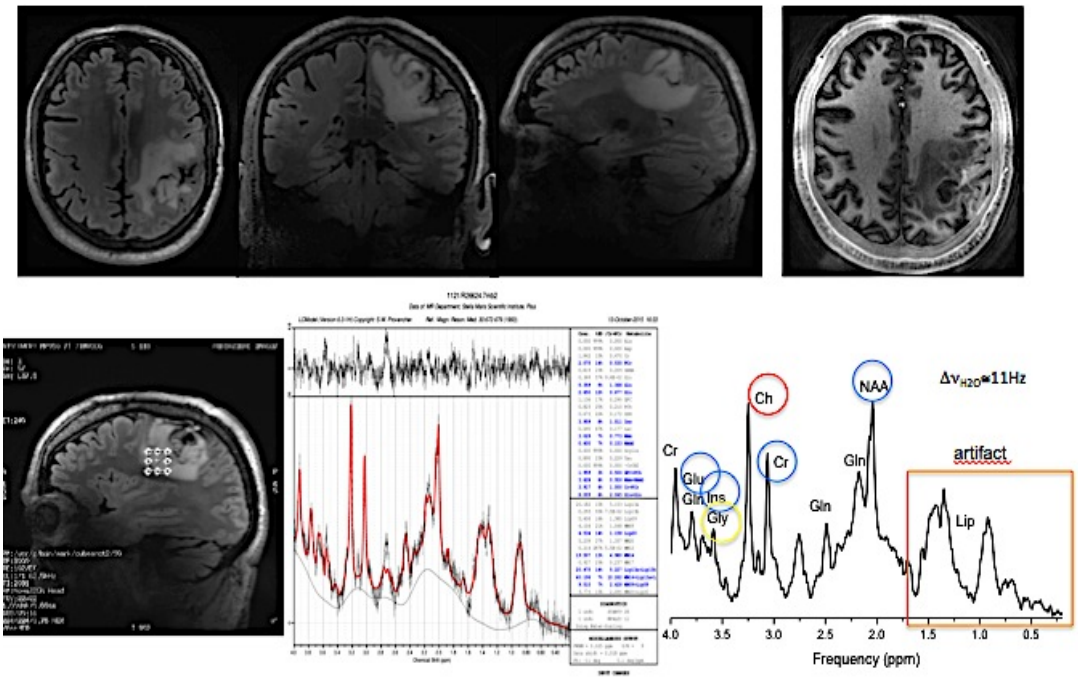

The selection of the VOI was positioned on FLAIR image on the left rolandic area. The spectrum measured in vivo with STEAM short TE show a high Choline (Ch) (red circle) peak and a reduction of NAA, creatine, Glutamate and myoinositol intensity signal (blue circles). It has also been detected a presence of glycine difficult to interpret (green circle). The orange box shows the artefacts in the region of lipids peak due to macromolecules.

5.3.5 Case 3

14 years old male with right frontal epilepsy. 7T MRI exhibited a round-ovalar dubious lesion in the right frontal lesion (low grade tumor, DNET, glial lesion), hyperintense on FLAIR sequence. The patient did not undergo epilepsy surgery.

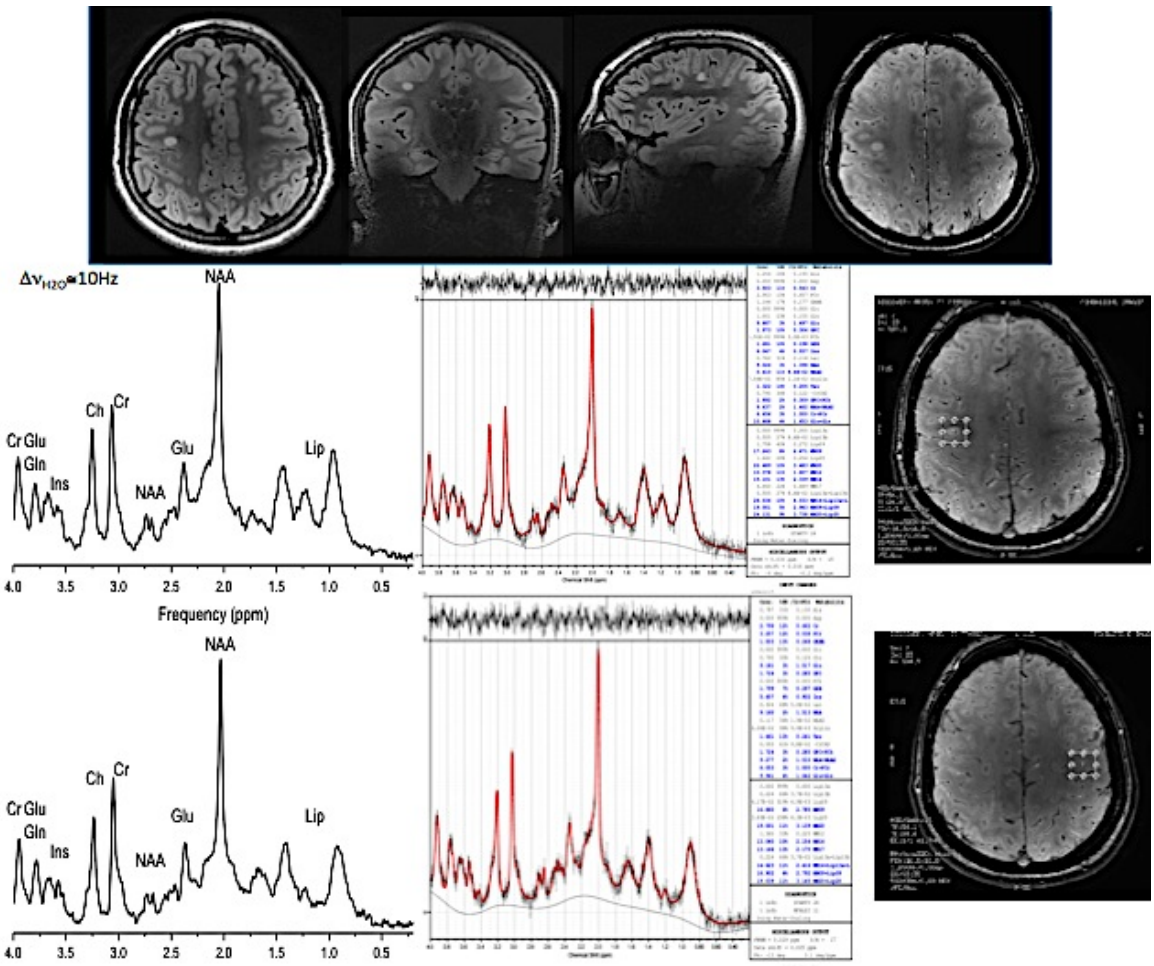

The selection of the VOI was positioned on SWAN image in the right frontal lobe where the lesion is located and another VOI on the contralateral region. The two spectra are superimposable. There are two main hypotheses that can explain this result. Firstly, the VOI may contain a discrete portion of normal tissue due to the small lesion; secondly the lesion could be a silent glial lesion that does not cause appreciable spectral changes.

5.4 Preliminary Results

This study shows that reliable metabolite quantification can be achieved with 7T MRS. However, discarding ten spectra of 24 acquired, we also demonstrate the difficulty in performing 1H MRS at 7T due to technical challenges related directly to UHF strength, issues inherent in voxel placement located in regions near air-tissue interfaces, and lesions inhomogeneity for the presence of necrotic and cystic areas, haemorrhage, calcifications and edema.

Our study had some limitations. The number of patients studied was relatively low. The brain lesion differed both in type and in location. The absence of normative data about the metabolite concentrations located in different brain regions might have affected the result in some patients. The absence of spectra collections from contralateral brain regions (which were assumed to be metabolically normal) has made difficult the evaluation of some lesions.

5.5 Future Perspectives

Increasing the magnetic field strength provides opportunities to explore the signal from nuclei other than protons, revealing new information about brain cellular activity. By using novel RF pulse sequences we can try to exceed the technical issues related directly to UHF strength. 1H MRS at 7T has the potential to be a powerful e non-invasive tool for improved diagnosis, treatment and management of brain diseases.

Our goals for the next few years include the following: (i) the use of new MR spectroscopy sequences such as STEAM-MiTiS (Toncelli et al. 2015) and Semi-LASER ^{1}H MRS (Scheenen et al. 2008; Penner et al. 2014) optimized for the selective metabolites detection not well seen or not visible at lower field strengths (e.g., Alanine, GABA, Ascorbic acid, Aspartate, Citrate, Ethanolamine, Glucose, Glutamate, Glutamine, Glutathione, Glycerol, beta-Hydroxybutyrate, Lactate, Phenylalanine, Phosphorylethanolamine, Serine, Taurine, Threonine, Tryptophan, Tyrosine, Valine), (ii) the reduction of volume of interest (VOI) decreasing the contamination from nearby areas, (iii) the acquisition of VOI in both affected and contralateral areas for each patient and (iv) increase patient recruitment.

5.6 References

1. Bottomley PA, Edelstein WA, Foster TH, et al. In vivo solvent-suppressed localized hydrogen nuclear magnetic resonance spectroscopy: a window to metabolism? Proc Natl Acad Sci U S A 1985;82(7):2148–2152.
2. Cai K, Nanga RP, Lamprou L, Schinstine C, Elliott M, Hariharan H, Reddy R, Epperson CN. The impact of gabapentin administration on brain GABA and glutamate concentrations: a 7T ^{1}H-MRS study. Neuropsychopharmacology. 2012 Dec;37(13):2764-71.
3. Carles Majos, Margarida Julia-Sape, Juli Alonso, Marta Serrallonga, Carles Aguilera, Juan J. Acebes, Carles Arus, and Jaume Gili. Brain Tumor Classification by Proton MR Spectroscopy: Comparison of Diagnostic Accuracy at Short and Long TE. AJNR Am J Neuroradiol 2004; 25:1696–1704.
4. Emir UE, Larkin SJ, de Pennington N, Voets N, Plaha P, Stacey R, Al-Qahtani K, Mccullagh J, Schofield CJ, Clare S, Jezzard P, Cadoux-Hudson T, Ansorge O. Noninvasive Quantification of 2-Hydroxyglutarate in Human Gliomas with IDH1 and IDH2 Mutations. Cancer Res. 2016 Jan 1;76(1):43-9.
5. Frahm J, Bruhn H, Gyngell ML, et al. Localized high-resolution proton NMR spectroscopy using stimulated echoes: initial applications to human brain in vivo. Magn Reson Med 1989;9(1):79–93.
6. Grams AE, Brote I, Maderwald S, Kollia K, Ladd ME, Forsting M, Gizewski ER. Cerebral Magnetic Resonance Spectroscopy at 7 Tesla: Standard Values and Regional Differences. Acad Radiol 2011; 18:584–587
7. Guerrini R, Duchowny M, Jayakar P, Krsek P, Kahane P, Tassi L, Melani F, Polster T, Andre VM, Cepeda C, Krueger DA, Cross JH, Spreafico R, Cosottini M, Gotman J, Chassoux F, Ryvlin P, Bartolomei F, Bernasconi A, Stefan H, Miller I, Devaux B, Najm I, Giordano F, Vonck K, Barba C, Blumcke I. Diagnostic methods and treatment options for focal cortical dysplasia. Epilepsia. 2015 Nov;56(11):1669-86.
8. Hanstock CC, Rothman DL, Prichard JW, et al. Spatially localized 1H NMR spectra of metabolites in the human brain. Proc Natl Acad Sci U S A 1988;85(6):1821–1825.
9. Horská A and Barker PB. Imaging of Brain Tumors: MR Spectroscopy and Metabolic Imaging. Neuroimaging Clin N Am. 2010 August ; 20(3): 293–310.
10. Kaminaga T, Kobayashi M, Abe T. Proton magnetic resonance spectroscopy in disturbances of cortical development. Neuroradiology 2001;43:575–80.
11. Kuzniecky R, Hetherington H, Pan J, Hugg J, Palmer C, Gilliam F, et al. Proton spectroscopic imaging at 4.1 Tesla in patients with malformations of cortical development and epilepsy. Neurology 1997;48:1018–24.

12. Li Y, Larson P, Chen AP, Lupo JM, Ozhinsky E, Kelley D, Chang SM, Nelson SJ. Short-Echo Three-Dimensional H-1 MR Spectroscopic Imaging of Patients With Glioma at 7 Tesla for Characterization of Differences in Metabolite Levels. J Magn Reson Imaging. 2015a;41(5):1332-41.

13. Li Y, Park I, Nelson SJ. Imaging tumor metabolism using in vivo magnetic resonance spectroscopy. Cancer J. 2015b;21(2):123-8.

14. Mekle R, Mlynarik V, Gambarota G, et al. MR spectroscopy of the human brain with enhanced signal intensity at ultrashort echo times on a clinical platform at 3T and 7T. Magn Reson Med. 2009; 61:1279–1285.

15. Mueller SG, Laxer KD, Barakos JA, Cashdollar N, Flenniken DL, Vermathen P, et al. Metabolic characteristics of cortical malformations causing epilepsy. J Neurol 2005;252:1082–92.

16. Pan JW, Duckrow RB, Gerrard J, Ong C, Hirsch LJ, Resor SR Jr, Zhang Y, Petroff O, Spencer S, Hetherington HP, Spencer DD. 7T MR spectroscopic imaging in the localization of surgical epilepsy. Epilepsia. 2013a;54(9):1668-78.

17. Pan JW, Duckrow RB, Spencer DD, Avdievich NI, Hetherington HP. Selective homonuclear polarization transfer for spectroscopic imaging of GABA at 7T. Magn Reson Med. 2013b;69(2):310-6.

18. Pan JW, Kuzniecky RI. Utility of magnetic resonance spectroscopic imaging for human epilepsy. Quant Imaging Med Surg. 2015;5(2):313-322

19. Penner J and Bartha R. Semi-LASER 1H MR Spectroscopy at 7 Tesla in Human Brain: Metabolite Quantification Incorporating Subject-Specific Macromolecule Removal. Magn Reson Med. 2014 Jul 31. doi: 10.1002/mrm.25380. [Epub ahead of print]

20. Riyadh N. Al-Okaili, Jaroslaw Krejza, Sumei Wang, John H. Woo, Elias R. Melhem. Advanced MR Imaging Techniques in the Diagnosis of Intraaxial Brain Tumors in Adults. RadioGraphics 2006; 26:S173–S189.

21. Scheenen TW, Heerschap A, Klomp DW. Towards 1H-MRSI of the human brain at 7T with slice-selective adiabatic refocusing pulses. MAGMA. 2008 Mar;21(1-2):95-101.

22. Simone IL, Federico F, Tortorella C, De BR, Bellomo R, Lucivero V, Carrara D, Bellacosa A, Livrea P, Carella A. Metabolic changes in neuronal migration disorders: evaluation by combined MRI and proton MR spectroscopy. Epilepsia 1999;40:872–79.

23. Fellah S, Callot V, Viout P, Confort-Gouny S, Scavarda D, Dory-Lautrec P, Figarella-Branger D, Cozzone PJ, Girard N. Epileptogenic brain lesions in children: the added-value of combined diffusion imaging and proton MR spectroscopy to the presurgical differential diagnosis. Childs Nerv Syst (2012) 28:273–282.

24. Tkáč I, Andersen P, Adriany G, et al. In vivo 1H NMR spectroscopy of the human brain at 7 T. Magn Reson Med 2001; 46:451–456; Tkáč and Gruetter, 2005.

25. Tkáč I, Oz G, Adriany G, Ugurbil K, Gruetter R. In vivo 1H NMR spectroscopy of the human brain at high magnetic fields: metabolite quantification at 4T vs. 7T. Magn Reson Med. 2009;62:868–879

26. Toncelli A, Noeske R, Cosottini M, Costagli M, Domenici V, Tiberi G, Tosetti M. STEAM-MiTiS: An MR spectroscopy method for the detection of scalar-coupled metabolites and its application to glutamate at 7 T. Magn Reson Med. 2015 Dec;74(6):1515-22.

27. Tschampa HJ, Urbach H, Träber F, Sprinkart AM, Greschus S, Malter MP, Surges R, Gieseke J, Block W. Proton magnetic resonance spectroscopy in focal cortical dysplasia at 3T. Seizure. 2015 Nov;32:23-9. doi: 10.1016/j.seizure.2015.08.008. Epub 2015 Aug 29.

28. van der Graaf M. In vivo magnetic resonance spectroscopy: basic methodology and clinical applications. Eur Biophys J. 2010 Mar;39(4):527-40.

29. Widdess-Walsh P, Kellinghaus C, Jeha L, Kotagal P, Prayson R, Bingaman W, Najm IM.Electro-clinical and imaging characteristics of focal cortical dysplasia: correlation with pathological subtypes. Epilepsy Res. 2005 Oct-Nov;67(1-2):25-33.

30. Zhu H, Barker PB. MR spectroscopy and spectroscopic imaging of the brain. Methods Mol Biol. 2011;711:203-26.